Dowex® H^+-mediated radioiodination of alkynes: molecular probes for tracing plant carbohydrate metabolism by multimodality imaging

Master's thesis

Iiro Rautsola
Department of Chemistry
Radiochemistry unit
University of Helsinki

1.12.2019

HELSINGIN YLIOPISTO
HELSINGFORS UNIVERSITET
UNIVERSITY OF HELSINKI
MATEMAATTIS-LUONNONTIETEELLINEN TIEDEKUNTA
MATEMATISK-NATURVETENSKAPLIGA FAKULTETEN
FACULTY OF SCIENCE

Faculty Faculty of Science	Degree program Master's program in Chemistry and Molecular Sciences	
Author Iiro Rautsola		
Level Master's thesis	Month and year December 2019	Number of pages 88 + 7 attachments

Abstract

Multimodality imaging is an efficient, non-invasive method for investigation of molecular and cellular processes *in vivo*. However, the potential of multimodality imaging in plant studies is yet to be fully realized, largely due to the lack of research into suitable molecular tracers and instrumentation. Iodine has PET- and SPECT-compatible radioisotopes that have significant advantages over other radioisotopes applied in plant radioisotope imaging, and can be incorporated into small molecules via a variety of reactions.

In this master's thesis, a radioiodination method exploiting a novel, Dowex® H^+-mediated addition of iodine for terminal alkynes was optimized and tested on two D-glucose analogues. The goal of the sugar analogue radioiodination was to develop a radioiodinated molecular tracer for plant carbohydrate metabolism studies. The parameters under optimization were activation Dowex® by HCl, reaction temperature, carrier amount, solvent, and evaporation of excess water. The most optimal results were achieved under the following conditions: Dowex® HCl-activated, reaction temperature 95 °C, amount of carrier 3.0 µmol of carrier, cyclohexanol as solvent, and excess water evaporated.

The Dowex® approach was compared to electrophilic reactions with Chloramine T and Iodogen, and it was concluded that the Dowex® approach leads to superior radiochemical yields under the optimized conditions. The Dowex® method was successfully tested on the sugar analogues, resulting in a single main product at a satisfactory 50 – 56 % radiochemical yield. The main products were successfully characterized with NMR, and in addition the method was indicated to be regioselective. It is plausible that the developed method may be improved further in terms of radiochemical yield and molar activity, and that the method could prove to be a useful tool for developing novel radiodinated molecular tracers for plant studies.

Keywords
multimodality imaging, radioiodination, alkynes, ^{125}I, PET, SPECT

Where deposited

Additional information

HELSINGIN YLIOPISTO
HELSINGFORS UNIVERSITET
UNIVERSITY OF HELSINKI
MATEMAATTIS-LUONNONTIETEELLINEN TIEDEKUNTA
MATEMATISK-NATURVETENSKAPLIGA FAKULTETEN
FACULTY OF SCIENCE

Tiedekunta Matemaattis-luonnontieteellinen tiedekunta		Koulutusohjelma Kemian ja molekyylitieteiden maisteriohjelma
Tekijä Iiro Rautsola		
Työn laji Pro gradu	Aika joulukuu 2019	Sivumäärä 88 + 7 liitettä

Tiivistelmä

Multimodaliteettikuvantaminen on tehokas, non-invasiivinen menetelmä solu- ja molekulaaristen prosessien tutkimiseen *in vivo*. Multimodaliteettikuvantamisen koko potentiaalia kasvitutkimuksessa ei kuitenkaan ole toistaiseksi voitu täysin hyödyntää, johtuen soveltuvien instrumenttien ja radiomerkkiaineita koskevan tutkimuksen puutteesta. Jodin SPECT- ja PET-yhteensopivilla radioisotoopeilla on merkittäviä etuja verrattuna aiemmin kasvien radioisotooppikuvantamisessa käytettyihin isotooppeihin verrattuna, ja jodia voidaan liittää pienmolekyyleihin useilla eri reaktioilla.

Tämän pro gradu -työn tavoitteena oli optimoida uusi, Dowex® H^+-välitteinen alkyynien radiojodiointimenetelmä ja testata menetelmää kahden D-glukoosianalogin radioleimaukseen. Sokerianalogien radiojodioinnin tarkoituksena oli kehittää radiomerkkiaine kasvien hiilihydraattimetabolian tutkimiseen. Optimoitavat parametrit olivat Dowex®-hartsin HCl-aktivointi, reaktiolämpötila, kantajan määrä, liuotin, sekä ylimääräisen veden haihduttaminen. Optimaalisimmat tulokset saavutettiin seuraavissa olosuhteissa: aktivoitu Dowex®, reaktiolämpötila 95 °C, kantajan määrä 3.0 µmol, liuottimena sykloheksanoli, ja ylimääräinen vesi haihdutettu.

Optimoitua Dowex®-menetelmää verrattiin elektrofiilisiin Chloramine T- ja Iodogen-reaktioihin, ja tulosten perusteella Dowex®-menetelmä johtaa merkittävästi korkeampaan radiokemialliseen saantoon optimoidun menetelmän olosuhteissa. Optimoidun radiojodiointimenetelmän toimivuutta sokerianalogien leimaukseen testattiin onnistuneesti, ja päätuotteiden radiokemiallinen saanto oli 50 – 56 %. Päätuotteet karakterisoitiin onnistuneesti NMR:lla, ja lisäksi havaittiin merkkejä menetelmän regioselektiivisyydestä. On mahdollista, että kehitetyn menetelmän radiokemiallista saantoa ja molaarista aktiivisuutta voidaan parantaa, ja että menetelmää voidaan hyödyntää kehitettäessä uusia radiojodioituja merkkiaineita kasvitutkimusta varten.

Avainsanat

multimodaliteettikuvantaminen, radiojodiointi, alkyynit, ^{125}I, PET, SPECT

Säilytyspaikka

Muita tietoja

Table of Contents

List of abbreviations

[^{18}F]FDG = 2-Deoxy-2-[^{18}F]fluoroglucose

µCT = micro (X-ray) computed tomography

ACN = acetonitrile

ANOVA = analysis of variance

BLT = bioluminescence tomography

CT = (X-ray) computed tomography

DMF = N,N-dimethylformamide

DMSO = dimethyl sulfoxide

DOT = diffuse optical tomography

FMT = fluorescence molecular tomography

HPLC = high-performance liquid chromatography

MRI = magnetic resonance imaging

NIR = near-infrared

NMR = nuclear magnetic resonance

PET = positron emission tomography

RCY = radiochemical yield

SPECT = single photon emission computed tomography

TLC = thin layer chromatography

1. Introduction

Multimodality imaging is the concept of combining two or more imaging modalities into one system, that is capable of scoping the target for morphological and functional information and compiling the acquired data into an image. Multimodality imaging is applied in a variety of fields, including (but not limited to) drug research, neuroimaging and oncology, and i*n vivo* multimodality imaging techniques are typically applied to humans and laboratory animals; however, similar molecular and cellular processes, that are monitored by multimodality imaging in humans and animals, are also present in plants, and the potential of multimodality imaging in plant biology research is yet to be fully actualized.

Molecular imaging covers a variety of imaging modalities that are applied to scope molecular and cellular level processes involving a molecular tracer. PET and SPECT are molecular imaging modalities utilizing molecular tracers labeled with radioactive isotopes, and they are widely used in molecular imaging due to their practically unlimited depth penetration and high sensitivity. The key factors to be taken into consideration when developing a molecular tracer for PET or SPECT studies are selecting a proper radioisotope in terms of decay mode and half-life, the chemistry required for the radiolabeling procedure, optimization of the labeling conditions, and *in vivo* behavior of the tracer.

The aim of this thesis was to assess the state and role of PET and SPECT multimodality imaging in plant studies and to optimize a radioiodination method for sugar analogues towards the end of utilizing these sugar analogues as molecular tracers for studying plant carbohydrate metabolism studies by multimodality imaging. The experimental part of the thesis utilized a radioiodination method for aliphatic alkynes that was first optimized using a commercially available precursor, and then tested on customized sugar analogues for characterization and assessment of radiochemical yield.

2. Molecular imaging

2.1 Principle of molecular imaging

Molecular imaging is a non-invasive method to provide information of molecular dynamics in a living organism by localizing, characterizing and quantifying molecular and cellular processes involving a specific molecular probe *in vivo*.[1–4] The molecular probe in question can be an

endogenous or exogenous chemical species, and in molecular imaging the spatiotemporal distribution of molecular and cellular processes involving the species are monitored directly or indirectly in two or three spatial dimensions and quantified over time, providing information of the kinetics and dynamics of the species.[3,4]

2.2 Imaging modalities

Imaging modalities can be grouped by the spatial resolution, the type of energy used in acquisition of the information, or, most importantly, the type of acquired information. The energy used may be electromagnetic or mechanical, the spatial resolution ranges from macroscopic to microscopic, and the type of information obtained can be structural or functional.[1,2] Different modalities also have differing penetration ranges that depend on the type of energy applied.

A particular imaging modality is typically good at acquiring a certain type of information, and some modalities are not exclusively limited to one type of information. However, a single modality is often insufficient to provide both structural and functional information of a specific target, often due to limitations in quantitativity, sensitivity or spatial resolution.[1,5] To overcome these limitations, different imaging modalities may be combined to provide both structural and functional information of a target: this is referred to as multimodality imaging. In order to produce a 3-dimensional image, the target may be scanned in sections and reconstructed via reconstruction algorithms: this is referred to as tomography.[3]

Molecular imaging modalities range beyond those discussed in this review. The imaging methods discussed in detail are thus limited to functional molecular imaging modalities and structural imaging modalities typically applied in tomographic multimodality imaging together with nuclear imaging. Special focus is given to molecular imaging modalities involving radiotracers: i.e. SPECT and PET. Some common imaging modalities and their properties are presented in Table 1.

Table 1. Common imaging modalities and their properties.

Modality	SPECT	PET	Optical	CT	MRI
Spatial resolution	1 – 4 mm (animal)[3] 5 – 12 mm (clinical)[3]	1 – 3 mm (animal)[3] 3 – 8 mm (clinical)[3]	≥ 5 mm (DOT)[1] 2 – 10 mm (FMT)[3] 3 – 10 mm (BLT) [3]	50 µm (CT)[5] < 1 µm (µCT)[6]	50 µm[5]
Depth penetration[1]	Not limited	Not limited	<10 mm	Not limited	Not limited
Sensitivity (mol of label detected)[5]	10^{-14}	10^{-15}	10^{-12}	10^{-6}	$10^{-9} – 10^{-6}$
Type of energy[1]	γ-rays	γ-rays	Visible light, infrared	X-rays	Magnetic fields, radio waves
Uses ionizing radiation[1]	Yes	Yes	No	Yes	No

2.2.1. Modes of radioactive decay in molecular radioisotope imaging

Molecular imaging modalities that are based on the detection gamma emissions (i.e. SPECT and PET) require that the molecular tracer applied is labelled with a radionuclide decaying via a suitable decay mode. For pure molecular imaging purposes (i.e. omitting theranostic applications) the relevant decay modes are: positron emission, which ultimately leads to two gamma photons emitted in opposite directions[3]; electron capture, which leads to a nucleus in a short-lived excited state that is relaxed through the emission of a single gamma photon[3]; and isomeric transition, in which a nucleus in a metastable state relaxes to ground state by emitting a photon[3]. α- and β^--decaying nuclides may decay into daughter nuclides in an excited state that relaxes into ground state by emitting gamma photons[7], and α- and β^--decaying nuclides with suitable gamma emissions may be utilized in theranostic applications[8], but for pure molecular

imaging purposes these decay modes are disregarded due to the undesired damage to tissues their particle emissions may cause in the target. In plant studies, where damage to tissue may not be of as high concern as in human and animal studies, β^--decaying nuclides are sometimes applied in real-time radioisotope imaging, but β^--emissions are strongly scattered and attenuated in the target medium, and are mostly used to study thin systems, such as roots and leaves.[9]

In β^+ decay, a proton in an unstable, proton-rich nucleus is converted into a neutron, and a positron and a neutrino are emitted from the nucleus. One up-quark decays into a down-quark via the weak nuclear force, leading to a virtual W^+ particle mediated emission of a positron and a neutrino.[10] In this process the atomic number of the nucleus is reduced by one while the mass number remains unchanged.[7] A Bohr model schematic of β^+ decay is illustrated in Figure 1.

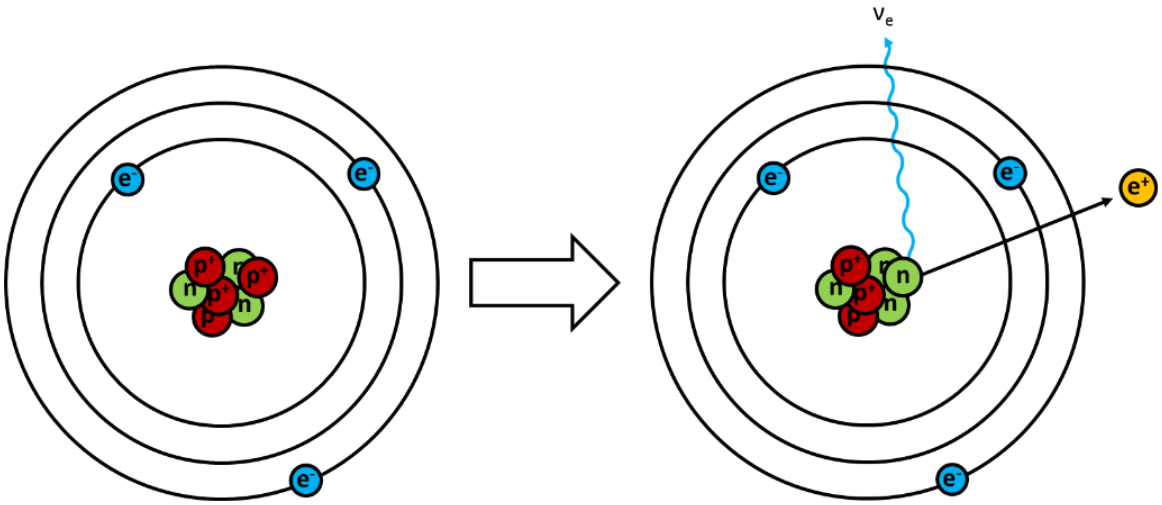

Figure 1. A Bohr model schematic diagram of β^+ decay. One of the protons is transformed into a neutron, leading to the emission of a positron and a neutrino.

The decay energy is distributed between the positron, the neutrino, and the recoiling nuclide. Due to the relatively small masses of the emitted particles compared to that of the nucleus, the recoil energy is negligibly small, and the total decay energy is thus considered to be distributed solely between the positron and the neutrino.[7] Energy values for the emitted particles are not constant and can be presented as a continuous probability distribution spectrum, the beta spectrum.[7,11] The emitted positron loses its kinetic energy gradually while travelling through a medium, until the energy is low enough to allow interactions with an electron.[7] Positron-electron interaction leads to an annihilation event, in which both particles are converted into

two photons.[11] Since the kinetic energy of both interacting particles in positron-electron annihilation is relatively low and therefore negligible when calculating the energy of the emitted photons, the total energy of the emitted photons is equal to the rest mass of an electron and a positron: this leads to two 0.511 keV gamma photons being emitted in opposite directions.[11] A schematic of electron-positron annihilation is illustrated in Figure 2.

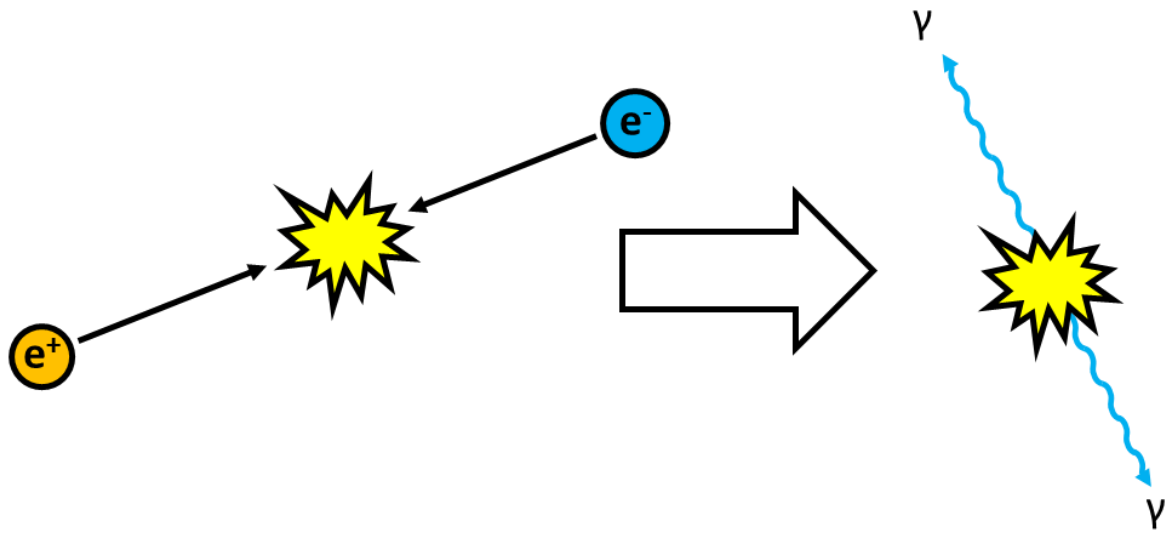

Figure 2. A schematic of electron-positron annihilation. Interaction of the particle-antiparticle pair leads to both particles being annihilated and converted into electromagnetic energy in the form of two 0.511 keV gamma photons emitted in opposite directions.

Electron capture is a competing process for β^+ decay, and in this process an unstable, proton-rich nucleus absorbs an electron from its inner electron shells, transforming the proton into a neutron and causing the emission of a neutrino that carries all of the decay energy.[7] In this process the atomic number is reduced by one while the mass number remains unchanged. A Bohr model schematic of electron capture is illustrated in Figure 3.

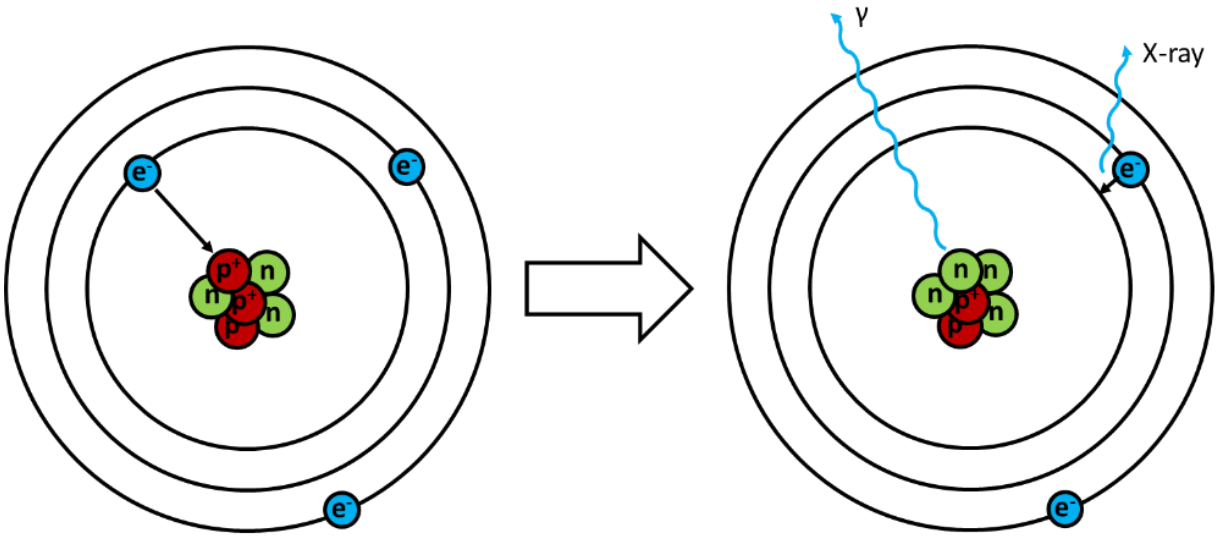

Figure 3. A Bohr model schematic of electron capture. A proton captures an electron from the inner shell, transforming into a neutron and resulting in a daughter nuclide in an excited state. The excited state relaxes into ground state, with the excitation energy emitted as a gamma photon. The inner-shell vacancy is filled by an electron from an outer shell, leading to X-ray emissions.

Electron capture may lead to a daughter nuclide in an excited state, whose transition to ground state produces gamma emissions.[3,7] The vacancy in the inner shell is filled by an electron from an outer shell, producing X-ray emissions.[3] The energy released in filling the vacancy may also be transferred to an orbital electron, which leads to the electron being ejected: this process is called Auger effect.[3]

Isomeric transition is the relaxation of a nucleus in a particularly long-lived, metastable excited state, that proceeds through gamma emissions.[3] An excited nucleus, metastable or otherwise, may also relax through a process called internal conversion, in which the excitation energy of the nucleus transfers to an orbital electron, leading to the electron being ejected with high energy.[7]

2.2.2. Functional imaging

The purpose of functional imaging is the localization, characterization and quantification of processes in the target system. In the context of this work, molecular imaging is considered a

subtype of functional imaging, and the terms overlap to some extent. The distinction between functional and molecular imaging is essentially in the scale and type of the processes under observation. In functional imaging the entity under study may be a process that is not of molecular or cellular nature, such as myocardial blood flow.[12] Molecular imaging, however, involves a molecular probe whose *in vivo* kinetics and dynamics are the processes under study, and the scale of the processes are on a fine, molecular or cellular level.[4]

2.2.2.1. Single photon emission computed tomography

Single photon emission computed tomography (SPECT) is an imaging modality that utilizes molecular tracers labeled with gamma-emitting radionuclides.[1] The radiotracer is introduced to the subject typically by an intravenous injection, and the distribution of the tracer is determined by detecting the gamma emissions with a gamma camera.[1] The gamma emission occurs when a decay event of an unstable nuclide leads to a daughter nuclide in an excited state.[7,11] The excess energy of this state is released as high energy electromagnetic radiation when the nuclide relaxes to ground state.[7] By scanning the target from multiple angles in transversal slices, a 3-dimensional image illustrating the distribution of the molecular tracer is then reconstructed.[1]

A SPECT system consist of a gamma camera that detects the incident gamma photons and converts the energy into an electric pulse, and a computer that reconstructs the image.[3,13] The gamma camera itself consists of three main components: a parallel- or a pinhole collimator, a scintillation crystal, and photomultiplier tubes.[13,14] The collimator filters the incident photons so that only those photons that are emitted perpendicular to the camera plane are recorded.[14,15] This improves image quality by filtering gammas scattered outside the target from interacting with the scintillation crystal: however, this reduces the sensitivity of a SPECT scan, since some emissions from inside the target are also filtered.[15] The photons that pass the collimator interact with the scintillation crystal (typically a NaI(Tl) crystal), producing a flash of electromagnetic radiation in the visible light spectrum that is transformed into an electric pulse and amplified in the photomultiplier tube.[13] These pulses are then counted and recorded by a computer that reconstructs a two-dimensional image of the distribution and density of detected decay events.[3,15] A schematic of a SPECT system is illustrated in Figure 4.

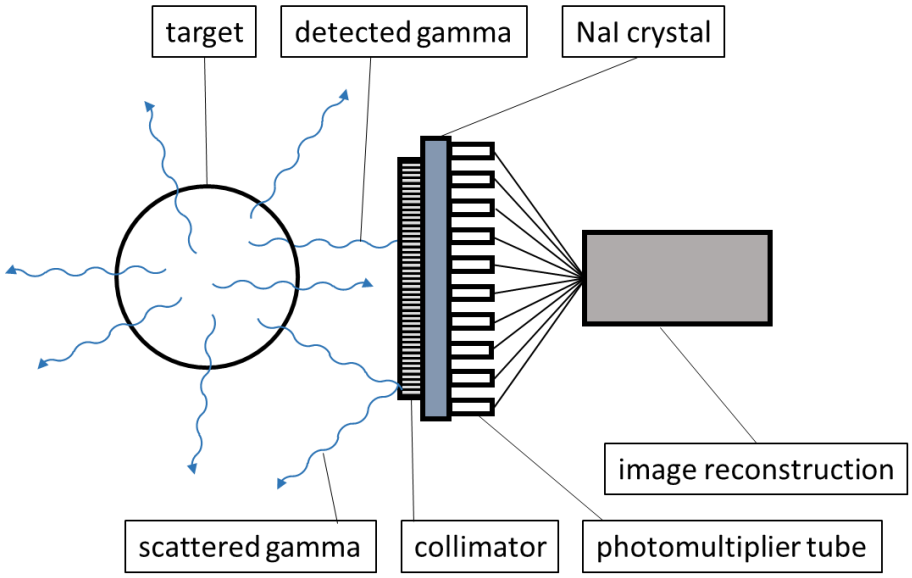

Figure 4. Schematic of a SPECT system. Emissions perpendicular to the camera plane pass the collimator and are detected, while other gammas are scattered and not detected.

A 3-dimensional image of the distribution of the radiolabeled tracer is reconstructed by rotating the camera around the target in a transversal plane, acquiring two-dimensional images of the target from multiple angles and processing the data with computer algorithms.[3,16] An illustration of SPECT image acquisition is presented in Figure 5.

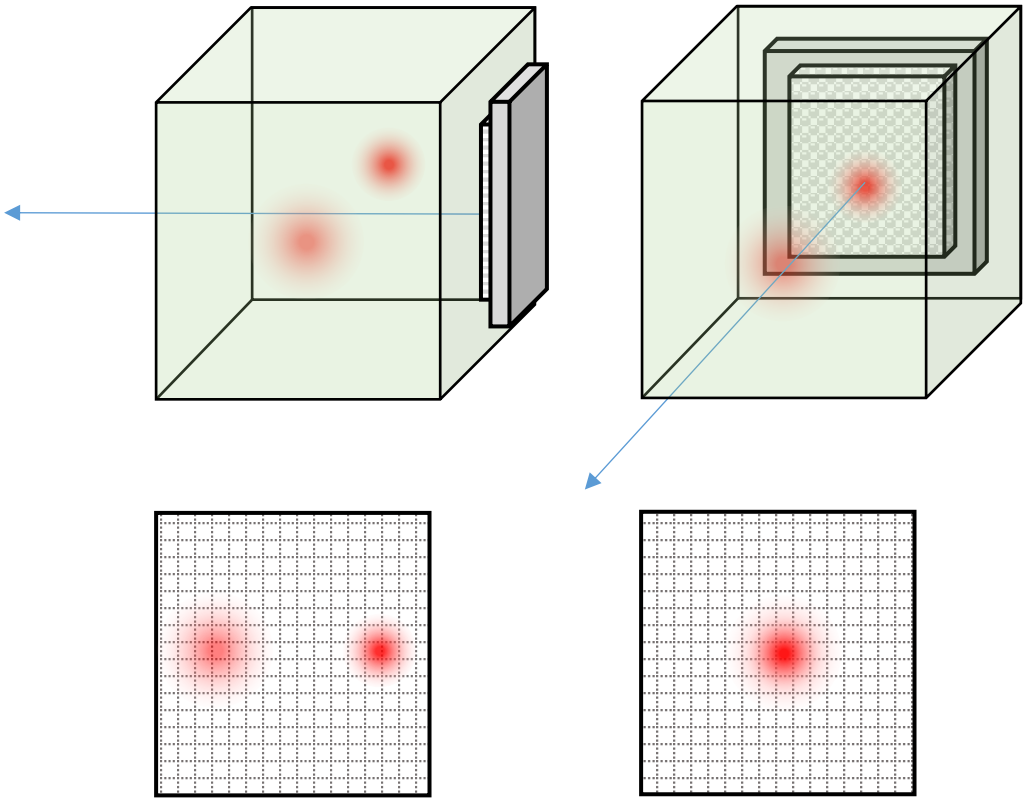

Figure 5. An illustration of SPECT image acquisition. The pictures on top row depict a SPECT camera imaging the target from two angles, and the bottom row pictures depict the planar images acquired from each angle. The red areas are concentrations of radioactivity.

The planar images are compiled into a sinogram, which is a container for the projection data for reconstructing the images.[1,3] The sinogram is then processed with a reconstruction algorithm to reconstruct an image of radioactivity distribution in the target.[3] The reconstructed, transversal tomographic slices are then stacked on top of each other to reconstruct a whole-target image. An illustration of SPECT image reconstruction is presented in Figure 6.

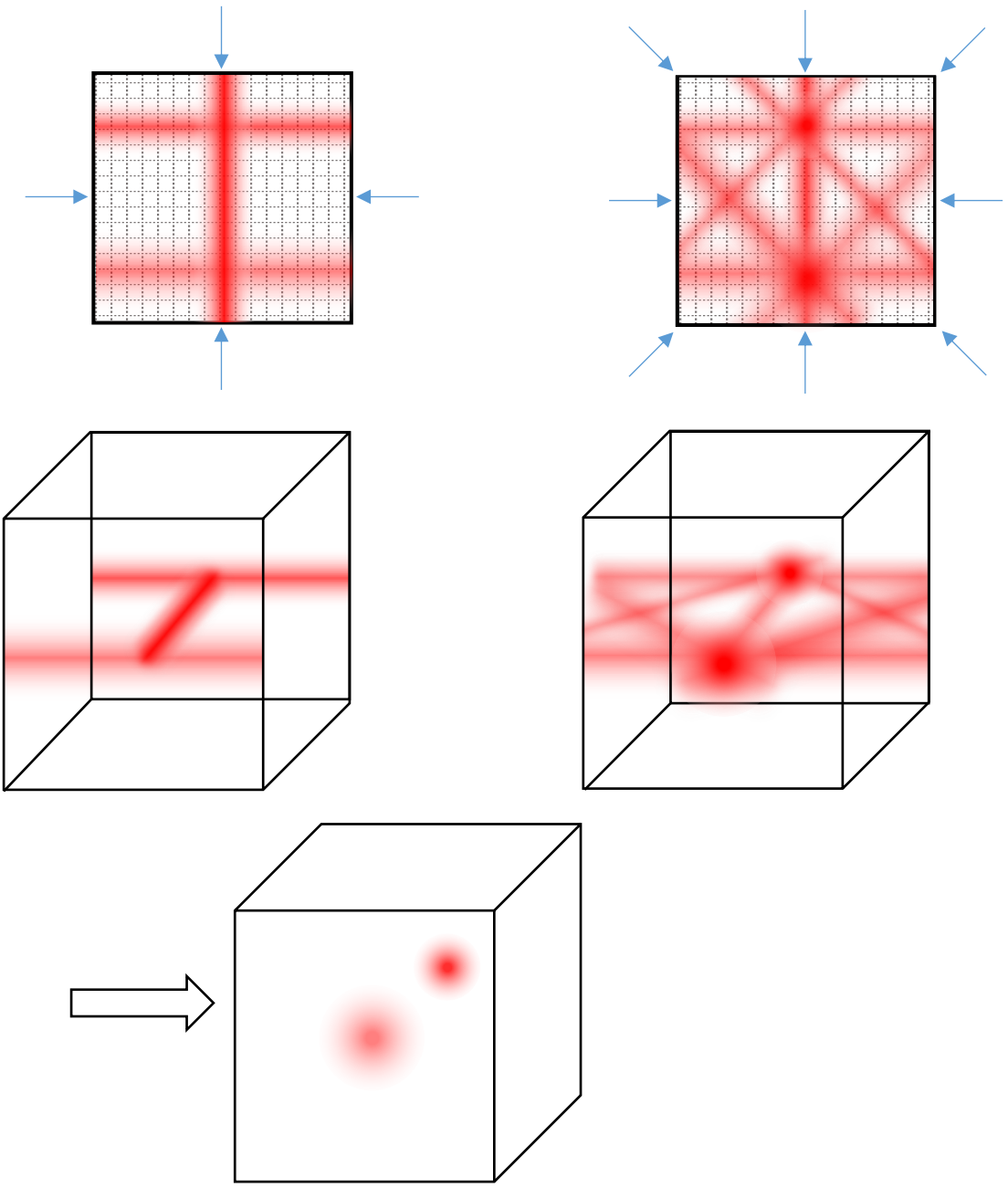

Figure 6. An illustration of SPECT image reconstruction. The top row depicts a top-down sinogram of a tomographic slice, with the directions of image acquisition visualized. The center row depicts sinograms in three dimensions, and the bottom row is a complete, processed and reconstructed image

The gamma photon is emitted directly from the position of the decay event: therefore, a SPECT scan's spatial resolution is not limited by photon energy.[1] However, the collimator used to filter out scattered gamma photons also filters emissions originating from inside the target, degrading

sensitivity.[13] Reduction of collimation or an un-collimated system may be used for studies where sensitivity is favored over spatial resolution.[13,17] A SPECT scan may be executed with two (or more) different molecular tracers labelled with different radionuclides whose gamma emission energies are suitably far apart, so that a detector with sufficient energy resolution can differentiate the gamma emissions by energy.[3]

2.2.2.2. Positron emission tomography

Positron emission tomography (PET) is an imaging modality that utilizes a radiotracer labelled with a positron-emitting radionuclide. The tracer is injected to the subject, and the location of the radioisotope is determined by detecting the two gamma photons resulting from the annihilation event following the positron emission.[15] The positron emitted travels through the medium, losing its kinetic energy until the energy is low enough to permit interactions with an electron.[7,13] The positron and electron, being a particle-antiparticle pair, annihilate upon interaction, leading to the conversion of the masses of the particles into electromagnetic radiation.[7]

The gamma photons emitted in opposite directions from the location of the annihilation event are detected by a dual-head gamma camera or a toroidal scintillation detector.[16] The target is scanned in transversal slices, which are then reconstructed to an image displaying the locations of detected annihilation events, providing information of the distribution of the molecular tracer inside the target.[3] The tomographic slices are then stacked to reconstruct a 3-dimensional whole-target image. A schematic of a PET system is illustrated in Figure 7.

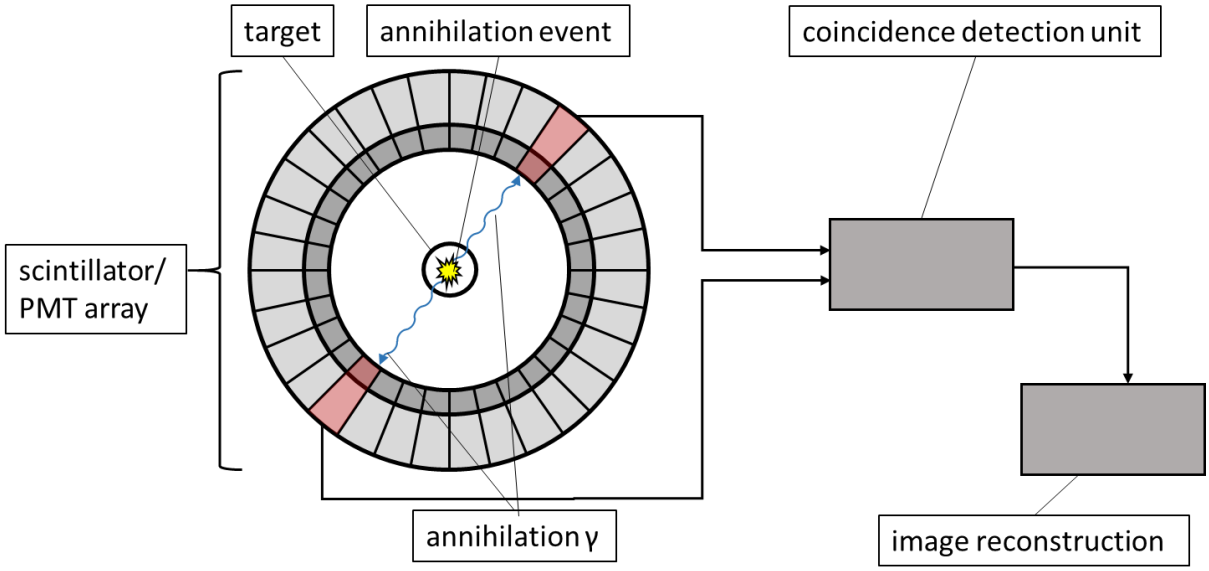

Figure 7. Schematic of a PET system with a toroidal detector. The annihilation gammas emitted in opposite directions reach the detector array simultaneously and are detected in coincidence.

The distance traveled by the positron before annihilation is determined by the initial kinetic energy of the positron.[3] This sets the limits to the spatial resolution of the PET scan: the longer the mean positron range, the lower the resolution.[13] Unlike a typical SPECT gamma camera, a PET detector does not utilize a collimator to filter scattered gamma photons; instead, the detector uses coincidence detection to distinguish the annihilation gammas from other gamma emissions interfering with the measurement, meaning only the events that are detected within a sufficiently short time interval are recorded.[13,16]

2.2.2.3. Optical tomography

Optical tomography covers a variety of techniques that exploit the properties of visible light and near-infrared radiation (NIR) to acquire information that can be of structural or functional nature, depending on the technique applied. Optical tomography is based on the variations in light-scattering and –absorbing properties of different materials, and due to the non-penetrating nature of visible light, the target material is usually light-transmitting or translucent, such as soft tissues. The acquired information is then processed to produce a three-dimensional image of the target. Optical tomography has the benefit of not relying on ionizing radiation or expensive equipment[1]. However, visible light and NIR lack the penetration of more energetic electromagnetic radiation, which sets limitations to the applications of optical imaging modalities.[1] Optical tomography, and optical imaging techniques in general, range beyond the

techniques described in this chapter, and the techniques described below were selected as points of interest due to being applied in multimodality imaging, as well as being established imaging modalities in plant studies.

Diffuse optical tomography (DOT) is a technique applying near-infrared (700 – 900 nm) spectroscopy to scope the target.[18] When NIR radiation is projected on the target, a small quantity of the incident photons will travel in the target medium nearly unscattered, along the axis of the incident light.[19] These photons can be differentiated from the scattered light and detected separately. The target is scoped to detect differences and changes in absorption and scattering properties in the target medium, and the acquired information is processed to obtain an image of the target.[18] An example of application of DOT is determining the spatial distribution of oxy- and deoxyhemoglobin in brain[19].

Fluorescence molecular tomography (FMT) is a technique using molecular probes based on a fluorescent compound, a fluorochrome, whose position in the target can be located by exciting the fluorochrome with a laser pulse and detecting the fluorescence emissions following the excitation.[20,21] Fluorochromes can absorb an incident photon of an appropriate wavelength and transition to an excited electronic energy state, which is unstable and will soon decay into a ground state. The excess energy from the transition to the ground state is emitted as a photon, and due to some of the deposited energy being spent on transitions between vibrational states, the emitted photon is of lower energy than the one absorbed.[20] The emitted photons can thus be differentiated from incident photons by a difference in wavelength, and the location of the probe is determined by detecting the emissions.[20,21] A three-dimensional image can be reconstructed by scanning the target in slices, and distribution of the fluorescent probe can be quantified over time.

Bioluminescence tomography (BLT) utilizes the properties of luciferases, enzymes capable of catalyzing an oxidative process on its substrates, small molecules referred to as luciferins, that exhibit emission maxima at 480 – 635 nm.[22,23] Luciferases are generally of biological origin (e.g. isolated from *Photinys pyralis* fireflies) and require the presence of cofactors such ad molecular oxygen, Mg^{2+} and ATP to induce bioluminescence.[23] After a luciferase has acted on its substrate, the oxidized product is in an excited state, and electromagnetic radiation in the visible light spectrum is emitted when the oxidation product relaxes to ground state: these emissions can then be localized and quantified to study the molecular and cellular processes

involved.[24] BLT does not require an external light source to induce bioluminescence, and the emissions can therefore be detected with ultra-sensitive equipment under low-light conditions.[21,23]

2.2.3. Structural imaging

Structural imaging is the imaging of a target at a certain point of time, providing a static image that can be used to study and analyze the morphology of the target. In the context of multimodality imaging, structural information is used in conjunction with functional information for localizing the concentrations of the molecular probe in the target.[25] The structural image also serves as a photon attenuation map for quantification of gamma emissions from within the target.[25–27]

2.2.3.1. Computed tomography

Computed tomography (CT) utilizes X-rays to scope differences in attenuation coefficients of the target to obtain three-dimensional structural information. The target is scanned with a monoenergetic X-ray source from multiple angles to determine the attenuation of the incident radiation in the target and to reconstruct a cross-sectional image illustrating the distribution of X-ray attenuation in two dimensions[15]. These images are then stacked to reconstruct a three-dimensional structural image of the target.

CT has practically unlimited depth penetration, a short acquisition time (minutes), and a high spatial resolution which can be further enhanced with contrast agents.[1,15] CT may be applied in some functional imaging purposes, such as perfusion and ventilation imaging[1,28], but the sensitivity of CT is often insufficient for molecular imaging purposes: hence, most applications of CT concern acquiring structural information.[1,15]

X-ray microtomography (μCT) is an imaging technique characterized by a spatial resolution better than 1 μm, and it can be used to acquire very high-resolution structural information.[1,6,29] A μCT system is designed for smaller field of view and higher resolution than a regular, clinical CT system, but is built on the same physical principles, and can be combined with other imaging modalities.[1] μCT is an imaging modality applied in a wide variety of fields: it can be used to scope mineralized and soft tissues[1,30], and materials such as wood, cement and composite

materials[6,29]. The native soft tissue contrast of μCT is relatively low, but can be enhanced with contrasting agents, such as iodine and phosphotungstic acid.[30,31]

2.2.3.2. Magnetic resonance imaging

Magnetic resonance imaging (MRI) is an imaging modality that utilizes the phenomenon of nuclear magnetic resonance (NMR). Nuclei with an odd number of nucleons have non-zero spin, and thus have an associated non-zero magnetic dipole momentum derived from a non-zero nuclear angular momentum.[15,32] When exposed to an external, constant magnetic field, magnetic nuclei can align parallel or anti-parallel to the applied magnetic field, and in thermal equilibrium more nuclei align with the field than against it, resulting in a net macroscopic magnetization vector aligned parallel to the field.[15,32] The nuclear angular momentum causes the nuclear magnets to precess around the magnetic field: the direction of precession is dependent on the orientation of the nuclear magnet about the axis of the applied magnetic field, and the frequency of precession is dependent on the magnitude of the magnetic field and the gyromagnetic radius of the nucleus.[32] The angular frequency of precession in a magnetic field of a specific strength is called the Larmor frequency. A non-equilibrium state may be generated by exciting the spin system with a oscillating radiofrequency pulse whose frequency matches that of the Larmor frequency, causing the spins to absorb the energy of the pulse and flip between energy states.[15] This changes the direction of the net magnetization vector, causing it to fall out of alignment with the applied magnetic field. Following the excitation, the nucleus relaxes by precessing at the nucleus's Larmor frequency about the applied magnetic field axis, generating an oscillating magnetic field that can be detected due to inducing a voltage in a detection coil.[32]

99,98% of hydrogen is of the isotope ^{1}H, which has a non-zero nuclear spin. Due to its ubiquitousness and presence in many molecules, e.g. water and fatty acids, ^{1}H is the most essential isotope in MRI, and typically MRI is applied to scan for distribution and concentration of water to scope the structure of a water-containing target.[1,32]

MRI can be used in a tomographic fashion, scanning the target in slices to reconstruct a three-dimensional image of the target. The Larmor frequency and the phase of precession can be manipulated by variations in the strength of the applied magnetic field: thus, a signal can be localized in the acquisition plane by creating a gradient in the applied magnetic field so that the

strength of the field varies with a linear relationship to distance.[32] The location of the signal is then determined in one direction by variations in the exciting frequency, and in an orthogonal direction by phase changes in the detected signal.[32]

2.3 Multimodality imaging

A single molecular imaging modality is often insufficient to acquire all the essential information from a target.[1,5] Multimodality imaging is the combination of two or more different molecular imaging modalities to acquire both structural and functional information of the target; either sequentially as independent systems; or simultaneously, integrating the modalities into one system.[5,33] The most established multimodality imaging combinations are SPECT/CT and PET/CT, but MRI has gained favor over CT due to having superior sensitivity and not relying on use of ionizing radiation.[33–35] Combination of optical modalities with PET to overcome the limitations in each modality (penetration depth and spatial resolution, respectively) has been reported.[5,33] Basically any arbitrary combination of imaging modalities is possible, assuming it is capable of yielding the needed information.[33]

2.3.1. Applications of multimodality imaging

Multimodality imaging is a way to non-invasively study the *in vivo* behavior of a molecular probe in real time over a structural framework, and its applications typically concern studies of molecular and cellular processes in living subjects, both humans and experimental animals.[1,33,36,37] Multimodality imaging is particularly suitable for applications in which high resolution and sensitivity are required, and in which the studied processes need to be localized in real-time and quantified over time. Multimodality imaging is widely used to facilitate drug research and monitor human health: for example, studying pharmacokinetics and -dynamics of a drug candidate using sub-threshold doses and imaging of brain structure and function are typical applications of multimodality imaging.[1,3,37,38] Perhaps the most well-known example of a multimodality imaging application are multimodal [^{18}F]- fluorodeoxyglucose studies that are conducted to quantify the distribution and accumulation of ^{18}F-labeled glucose inside the target biological system and combine this functional information with a morphological image of the target.[33,39] This image can then be used to locate sites of abnormal glucose metabolism, such cancerous tissues, infection and inflammation, and osteoarthritis.[3,33,37,40]

2.3.2. Radioisotope and multimodality imaging in plants

While multimodality imaging techniques are widely applied in studies involving humans and animals, their utilization in plant studies appears to be less common.[9,41–43] Current molecular and cellular level imaging techniques used in plant studies mostly utilize autoradiography and optical imaging modalities, out of which fluorescence imaging is the most prevalent.[9,44–49] The applications of molecular imaging in plants include, but are not limited to, phenotyping and studying of autophagy, nutrient transport and chloroplast movement.[9,46,47,49,50]

Autoradiography methods require termination of physiological activity in the target and produce only static images of radiotracer distribution, and are therefore incompatible in real-time imaging approaches.[9,51] In addition, autoradiography can be applied only in 2-dimensional imaging of planar systems, such as leaves, and is ill-suited for 3-dimensional imaging of whole plants.[51] Optical imaging modalities can be used to study molecular and cellular processes of plants in real-time and may be combined with a structural imaging modality to study the target in a multimodality fashion, but the limited penetration depth hinder the applicability of optical imaging to monitoring processes occurring on the surface or in the thinner parts, such as leaves, of the plant. Furthermore, fluorescence imaging modalities require darkness for detection while plants require light for normal physiological activity, rendering application of real-time fluorescence imaging to plants complicated.[41]

Majority of the documented real-time radioisotope imaging systems for plants are based on β^-- and β^+-emissions[9,41,43,51–55]. Gamma camera has been used to study ^{137}C uptake[56], and at least one un-collimated detector single-photon system for small animal and plant imaging has been presented[17]. The combination of PET and MRI has been used to investigate structures, transport routes and translocation dynamics using ^{11}C-labelled tracers and [^{11}C]CO_2[52], and a PET/CT system has been utilized in [^{18}F]FDG- and [^{68}Ga]gallium citrate translocation studies[57]. MRI and CT as independent imaging modalities are relatively well established structural imaging modalities in plant studies[58–62], so the basis for further development of plant multimodality imaging systems exists. µCT, in particular, has proved to be an effective imaging modality in plant studies due to its high resolution[29]: for example, it has been used to study the accumulation and distribution of selenium in *Arabidopsis thaliana* roots[63], and changes in tissue density of lyophilized *Brassica oleracea* leaves.[64]

The most significant issue in imaging systems utilizing β^--emissions is the self-absorption of β^--particles in the target, which limits the usefulness of these systems to imaging only thin targets, such as roots and leaves.[9] In addition to self-absorption in the target, attenuation of β^--emissions may occur in the airspace between the target and the detector.[65] β^+-emissions travel in the medium until their kinetic energy is low enough to allow annihilation: therefore, when imaging thin targets, positron escape may occur particularly with high-energy β^+-emissions.[9,66]

Radioisotopes used in plant radioisotope imaging include (but are not limited to) ^{11}C, ^{13}N, ^{18}F, ^{15}O, ^{32}P, ^{35}S, ^{45}Ca, ^{55}Fe, ^{137}Cs and ^{68}Ga, and among their fields of application are nutrient uptake, water movement and CO2 translocation studies, in which the radionuclides are bound to simple, neutral molecules such as H_2O or CO_2, or in mono-and polyatomic cations and anions such as Cs^+ and $(PO_4)^{3-}$.[41,56,57,67] With the exception of [^{18}F]FDG studies[51,57,68], more complex small molecules appear to be rarely used in plant radioisotope imaging: therefore, novel molecular tracers could open new possibilities in developing and utilizing multimodality imaging methods for plant studies. Carbon, nitrogen and oxygen are ubiquitous in organic compounds and may be substituted with ^{11}C, ^{13}N and ^{15}O: however, the half-life of these radionuclides ($t_{½}$ = 20.4, 9.96 and 2.03 min, respectively) limits their applicability to experiments of a short timescale.[57,67] In addition, their applicability is further limited by their decay mode of positron emission, which may result in positron escape when probing thin systems; this is also true for ^{18}F. However, applying PET in real-time, non-invasive plant imaging is becoming more common, and PET/CT and PET/MRI systems for plant imaging have been reported[52,57]; thus, further utilization of multimodality imaging systems involving PET in plant studies depends on the development novel molecular tracers, particularly small molecules labelled with long-living positron-emitting isotopes such as ^{124}I, ^{89}Zr and ^{86}Y ($t_{½}$ = 100.2, 78.4 and 14.7 h, respectively)[69], so that compounds with slower kinetics may be utilized.

PET appears to be a more commonly applied tomographic radioisotope imaging modality in plant studies than SPECT, and radionuclides with SPECT-compatible gamma emissions are rarely exploited in plant radioisotope imaging. A study in which ^{137}Cs uptake was imaged using a gamma camera is reported[56], and an un-collimated detector single-photon imaging system was used in a $^{99m}TcO_4^-$ xylem transport study[17]; however, in these studies the gamma camera was used in planar imaging, not in a tomographic fashion, and a true SPECT system for plant studies is yet to be reported. In the aforementioned studies the gamma-emitting nuclides were

applied in the form as cations or anions, and studies, in which the radionuclide was introduced in the target system in the form of a neutral molecule, are yet to be reported. The functionality of a SPECT imaging system is not hindered by positron escape, and therefore SPECT could prove to be a superior imaging modality particularly when imaging thin parts of a plant. However, to fully exploit these advantages, further research is needed in combining and applying SPECT with MRI or CT in plant studies, and in developing novel, SPECT-compatible molecular tracers.

Radioisotope imaging modalities are superior in terms of sensitivity and penetration depth to optical imaging modalities, and maintaining conditions required for natural physiological activity in the target plant are less complicated when using real-time radioisotope imaging methods, since these methods do not require darkness (as do optical imaging modalities) nor termination of physiological activity (as does autoradiography). The obvious advantage PET and SPECT imaging modalities have over planar radioisotope imaging is the capability of providing 3-dimensional, functional information of the target[57], and, when combined to a structural imaging modality in a multimodality fashion, could prove to be a powerful tool in plant studies, particularly when imaging thick systems and kinetics of organic biomolecules in plants. However, PET and SPECT have yet to become established imaging modalities in plant studies, and more research in developing suitable instrumentation and molecular tracers is required to fully realize the potential of PET or SPECT multimodality imaging of plants.

3. Iodine in multimodality imaging

3.1 Properties and chemistry of iodine

Iodine is an element of the halogen group with atomic number 53.[70] At standard conditions molecular iodine, I_2, is present as a lustrous dark-gray, non-metallic solid that sublimates into a violet gas.[3,70,71] I_2 is only slightly soluble in water, but dissolves readily in nonpolar solvents.[3] Iodine occurs in oxidation states −1, +1, +3, +4, +5, +6 and +7, oxidation states +3, +4 and +6 being relatively uncommon.[70] Physical properties of iodine are presented in Table 2.

Table 2. Physical properties of iodine.

Atomic number[3]	Atomic radius (pm)[3]	Ionic (I^-) radius (pm)[3]	Electron structure[3]	Electronegativity (Pauling scale)[3]	Oxidation state (most common in **bold**)[3]	Ionization potential (eV)[72]
53	133	216	[Kr]$4d^{10}5s^2$ $5p^5$	2.66	**−1**, **+1**, +3, +4, **+5,** +6, **+7**	10.44 (1^{st}) 19.13 (2^{nd}) 32.96 (3^{rd})

In comparison to other stable halogens (astatine is a halogen with no known stable isotopes; its properties are not well known and is thus omitted in the following comparisons), iodine is less electronegative and larger in ionic radius. These properties render iodine's electron cloud relatively polarizable, and as a consequence molecular iodine is considered formally to have the structure of $I^+–I^-$ in aqueous solutions.[3] The electronegativity and ionic radius of iodine are comparable to those of a methyl group, and when assessing molecular interactions with species containing iodine atoms, its properties can be approximated to be close to those of a methyl group.[73] Van der Waals radius and electronegativity for stable halogens and methyl group are presented in Table 3.

Table 3. Van der Waals radius and electronegativity for stable halogens and the methyl group.[73]

	H	F	Cl	Br	I	CH_3
Van der Waals radius (Å)	1.20	1.35	1.80	1.95	2.15	2.00
Electronegativity	2.28	3.95	3.03	2.80	2.47	2.30

Due to the relatively low electronegativity of iodine, bond enthalpies of diatomic halogen molecules, hydrogen halide and carbon–halogen bonds are lower for iodine than for other stable halogens.[71,72] The length of carbon–iodine bonds decreases with increasing s character of the carbon, while bond enthalpy increases, implying a correlation between bond stability and degree of s character.[73] Bond lengths of C–I bonds are presented in Table 4.

Table 4. Lengths of C-I bonds.[73]

s character of carbon	sp^3	sp^2 (ethylenic)	sp^2 (aromatic)	sp
Bond length (Å)	2.13	2.09	2.05	1.99

The electrophilic iodine species I^+ readily complexes with nucleophiles, and therefore does not exist as a free species in aqueous solutions.[3] Electrophilic iodine reacts with oxygen forming neutral oxides, most of which are unstable and thus unisolatable, and reactions with water lead to a multitude of anionic species, the most stable iodine anions being iodide, iodate and periodate. In nature iodine occurs mostly in oxidation state -1 in the form of sodium or potassium salts.[3] Anions and oxides of iodine in common oxidation states are presented in Table 5.

Table 5. Anions and oxides of iodine in common iodine oxidation states.[70]

Oxidation state	-1	+1	+5	+7
Anion name	iodide	hypoiodite	iodate	periodate
Anion formula	I^-	IO^-	IO_3^-	IO_4^- (metaperiodate), IO_6^{5-} (orthoperiodate)
Oxide name	-	diiodine monoxide	diiodine pentoxide, diiodine tetroxide, tetraiodine nonaoxide	tetraiodine noanoxide
Oxide structure	-	I_2O	$O(IO_2)_2$ (pentoxide), $(IO_2)_2$ (tetroxide), $I(OIO_2)_3$ (nonoxide)	$I(OIO_2)_3$

3.2 Stable iodine as a contrasting agent in CT

The native soft-tissue contrast of CT and μCT is relatively low, but can be improved with the use of a suitable contrasting agent. Iodine-based contrasting agents are common in CT studies,

(particularly in μCT) due to iodine's X-ray attenuating properties[74], and one of the more popular methods of enhancing CT contrast in *ex vivo* and *in* vitro studies is staining with Lugol's iodine, an aqueous solution of two parts of KI to one part of I_2.[75] However, for *in vivo* purposes such as cardiac, vascular and cancer imaging, more attractive choices for contrasting agents are iodinated small molecules and iodine-containing nanoparticles.[74,76] Iodine-containing nanoparticles are particularly attractive for *in vivo* studies, since their renal clearance rate is typically slower than that of iodinated small molecules, enabling imaging over extended time periods[74,76]. Another attractive feature of iodine as a CT contrasting agent is the possibility of simultaneously using a radioiodinated tracer and an iodinated contrast agent in PET/CT and SPECT/CT multimodality imaging, since the improved CT resolution can be exploited to improve the quality of attenuation correction of the radioisotope imaging modality, and thus improve SPECT or PET image quality.[76]

3.3 Radioisotopes of iodine in molecular imaging

Iodine has 37 known isotopes, of which only ^{127}I is stable: the rest undergo radioactive decay.[73] The longest-lived radioisotope of iodine is ^{129}I, with a half-life of 1.57×10^7 y.[7] ^{129}I is generated in the atmosphere by cosmic radiation-induced nuclear reactions, and it is the only radioisotope of iodine naturally present in the environment, although only in trace amounts.[7] The rest of the radioisotopes of iodine have half-lives of less than 60 days and are all synthetic, being either fission products or produced with charged particle reactions and neutron activation.

There are many different modes through which an unstable nucleus may decay, but in the context of SPECT and PET imaging only the decay modes which lead to sufficiently abundant emissions of gamma photons of a suitable energy are useful. The daughter nuclide is ideally stable, since additional gamma emissions from subsequent decay events may interfere with the measurement. The gamma energy must be sufficiently high to penetrate target medium; however, the higher the gamma energy, the less likely it is to interact with the detector, leading to compromised sensitivity. In addition, high energy gamma emissions cause issues concerning radiation safety due to their penetrating nature, and thick lead shielding must be used to avoid external exposure. The half-life of the nuclide is an important aspect considering *in vivo* applications. A suitable (radiological) half-life depends on the kinetics that determine the biological half-life of the compound: the nuclide must be long-lived enough to assure the radiolabeled compound reaches its destination, but a long half-life leads to less decay events

during the measurement period, compromising sensitivity, in addition to needlessly increasing patient dose in medical applications.[77,78]

In the context of this study, four radioisotopes of iodine are discussed as radiopharmaceutically relevant and suitable for molecular imaging purposes due to their decay properties. These isotopes and their most significant decay properties are presented in Table 6.

Table 6. Radiopharmaceutically relevant radioiodine isotopes and their decay properties.[73]

Isotope	t½	Decay mode(s)	E (MeV)
^{123}I	13.22 h	EC (100 %)	γ 0.159 (83.3 %)
^{124}I	4.176 d	β^+ (22.4 %)	E_{β^+}max 2.13 (10.8 %)
		EC (77.6 %)	γ 0.603 (62.9 %) 0.723 (10,4 %) 1.691 (11.2 %)
^{125}I	59.41 d	EC (100 %)	γ 0.0355 (6.68 %)
^{131}I	8.021 d	β^- (100 %)	E_{β^-}max 0.606 (89.9 %)
			γ 0.284 (6.14 %) 0.365 (81.7 %) 0.637 (7.17 %)

^{123}I is a short-lived isotope of iodine that decays to ^{123}Te (t½ = 1.3 x 10^{13} y; observationally stable) via electron capture, emitting abundant (83 %) 159 KeV gamma emissions.[73,79] ^{123}I is applied in SPECT imaging due to its ideal gamma energy, and its half-life is sufficiently long for studying pharmacokinetics over extended periods.[78–80] Using ^{124}Xe as target material, ^{123}I can be produced in a cyclotron via several nuclear reactions, e.g.:[79]

^{124}Xe (p, 2p) ^{123}I

^{124}Xe (p, pn) ^{123}Xe $_{(t½=2.08\ h)}$ → ^{123}I

^{124}Xe (p, 2n) ^{123}Cs $_{(t½=5.9\ min)}$ → ^{123}Xe $_{(t½=2.08\ h)}$ → ^{123}I

^{124}I is an isotope of iodine with a moderate half-life. ^{124}I decays to stable ^{124}Te via positron emission and electron capture, and it is applied in PET imaging.[73,80,81] Due to its half-life, ^{124}I is particularly suitable for labelling molecular tracers that have particularly slow pharmacokinetics.[73,80] It can be produced in a cyclotron via the reaction:[73,80]

^{124}Te (p, n) ^{124}I

^{125}I is a long-lived isotope of iodine that decays to stable ^{125}Te via electron capture. Its gamma emissions are relatively weak compared to other radiopharmaceutically relevant iodine isotopes, rendering ^{125}I incompatible with *in vivo* SPECT imaging. The most significant gamma emission is not particularly abundant (6.68 %), and due to their low energy, 35.5 keV, the emissions are significantly attenuated in the target and thus hard to detect outside the target.[82] However, the relatively long half-life and easily attenuated gamma emissions render ^{125}I particularly suitable for in *vitro* studies due to the relative ease of handling and protective measures.[73,82] ^{125}I also produces abundant Auger electrons, and it is used in sealed-source brachytherapy for treatment of cancer of the eye, prostate, breast, etc.[73,83,84] ^{125}I can be produced in nuclear reactors via the reaction:

^{124}Xe (n, γ) ^{125}Xe $_{(t½=17\ h)}$ →^{125}I

^{131}I has a moderate half-life, and decays to ^{131}Xe via β^- decay. Due to its decay mode it is not used for pure imaging purposes; ^{131}I is rather used in radiotherapy while its gamma emissions can be utilized simultaneously in imaging, rendering ^{131}I suitable for theranostic applications. ^{131}I is produced in nuclear reactors as a fission product of ^{235}U:

^{235}U (n, fission) ^{131}I, ^{99}Mo, ^{117}Pd, ^{137}Cs, …

3.4 Radiolabeling methods with radioiodine

There are numerous known iodination reactions, all of which can generally be used in radioiodinations. However, radiochemical synthesis has its own special conditions to be considered, and usually a known iodination method needs to be specifically adapted to

radiochemical purposes to overcome these conditions. Most radiopharmaceutically relevant isotopes of iodine have characteristically short half-lives: therefore, the radioiodination reaction has to be optimizable for relatively short (e.g. < 1 h) reaction times in order to avoid excess product loss due to radioactive decay, and ideally the labeling procedure can be executed in one step and one pot.[73] When the concentration of radioiodine in a radioiodination reaction is low, stable iodine may need to be added to the reaction mixture as isotopic carrier to ensure that the radionuclide behaves normally during the reaction.[85]

Iodine is a volatile element, and safety precautions include prevention internal exposure via inhalation of radioiodine when working with radioactive iodine isotopes. In addition, proper lead shielding is required to prevent external exposure to radiation. In practice this means that radioiodinations should be carried out in a ventilated environment, such as a glove box or a fume hood, and that, during working with radioiodine and handling radioiodinated samples, external exposure to radiation should be prevented by sufficiently thick lead shielding and avoiding positioning oneself unnecessary close to the source of radiation. When working with ^{125}I, additional care must be taken to prevent contaminating detectors etc., since ^{125}I:s long half-life renders these contaminations particularly troublesome.

Most essential radioiodination reactions are nucleophilic and electrophilic substitutions, and these reactions are discussed in detail in the scope of this study. In addition, halogenations of alkenes and alkynes are discussed separately.

3.4.1. Nucleophilic substitution

In nucleophilic substitution the attacking species acts as the nucleophile, donating an electron pair to a covalent bond formed with an electrophilic species, while the electrophile's bond with the leaving group, the nucleofuge, is disconnected, and the nucleofuge leaves with an electron pair.[73,86] In the context of nucleophilic radioiodinations, the attacking species is the iodide anion, I^-, which can exist as a free species and is thus easy to introduce into the reaction mixture in the form of, for example, NaI. Nucleophilic substitutions may occur in aliphatic and aromatic compounds, and the mechanisms vary depending on the aromaticity, or lack thereof, of the substrate.[73,86]

Nucleophilic substitution in aliphatic compounds occurs mostly via S_N1 and S_N2 mechanisms. The essential difference between S_N1 and S_N2 mechanisms is at which step the leaving group

is disconnected from the compound: in S_N1 the disconnection occurs before the nucleophile forms a bond with the electrophile, whereas in S_N2 mechanism the nucleophile first attacks the electrophile, forming a transition state with a -1 net charge and in which the negative charge is distributed between the nucleophile and the nucleofuge, after which the leaving group is disconnected.[73,86] These differences are demonstrated in Equation 1 and Equation 2:

$$S_N1: RX + Nu^- \rightleftharpoons R^+ + X^- + Nu^- \rightleftharpoons RNu + X^-$$

Equation 1

$$S_N2: RX + Nu^- \rightleftharpoons \left[X^{\delta-} - R - Nu^{\delta-}\right]^- \rightleftharpoons RNu + X^-$$

Equation 2

where R is the substrate, X (≠ H) the leaving group and Nu the nucleophile. Another distinctive feature between S_N1 and S_N2 mechanisms is the effect on stereochemistry: S_N2 results in the reversal of stereochemistry, whereas in S_N1 the nucleophile may attack from both sides, leading to a racemic mixture of products.[86] This is demonstrated in Figure 8

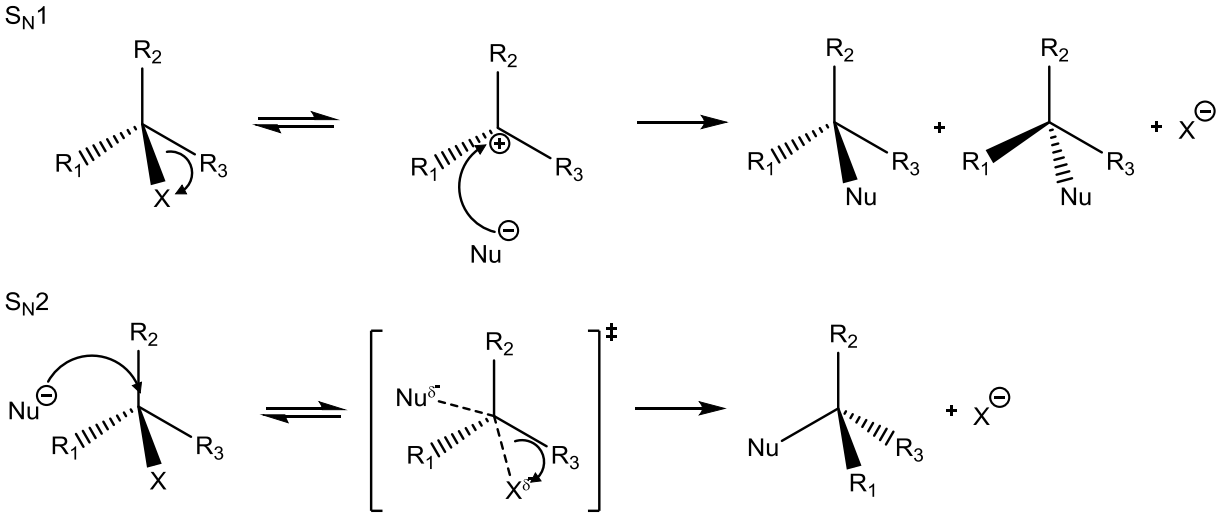

Figure 8. Schematics of S_N1 and S_N2 mechanisms. In S_N1 reaction a racemic mixture is produced, whereas in S_N2 the stereochemistry is reversed.

In S_N1 the rate-determining step is the unimolecular step in which the leaving group is disconnected: therefore, the reaction rate displays first-order dependence on electrophile concentration.[86] In S_N2 the rate-determining step is the bimolecular step in which the transition

state is formed: the formation of the transition state displays first-order dependence on the concentrations of the nucleophile and the electrophile, meaning the overall reaction rate follows second-order kinetics.[86]

The solvent has a significant effect on the reaction rate of S_N1 and S_N2 reactions. The reaction rate depends on solvation of the transition state, reagents and products, and S_N1 reactions favor protic solvents, whereas S_N2 reactions favor aprotic solvents.[86] The polarity of the solvent also affects the reaction rate, depending on the mechanism: S_N1 reaction rates increase with the polarity of the solvent, whereas for S_N2 reactions favor less polar (but polar nonetheless) solvents.[73,86]

The leaving groups in aliphatic substitutions are typically sulphonates, such as triflates, mesylates and tosylates, or halides.[73,86] In aliphatic iodinations, sulphonates are generally considered to be better leaving groups than halides; however, due to practical reasons a halide is often selected as the leaving group.[73] The order of nucleofugality of halogens with iodide anion as the attacking species follows the order I > Br > Cl.[73] Isotope exchange, i.e. substituting a stable iodide atom with a radioactive iodine isotope, is a simple and viable, although a non-efficient, radioiodination method when high specific activity is not necessary.[73]

Nucleophilic substitution via addition-elimination route can also occur in aromatic compounds in S_NAr mechanism, which requires a leaving group X ($\neq$ H) at the preferred position of substitution.[86] In addition, the aromatic system must be activated, either by an electron-withdrawing group (EWG) with –M and/or –I effect in ortho- or para-position to the leaving group.[73,86] An example electron-withdrawing group is a nitro or a carbonyl group, and the purpose of the EWG is to stabilize the negative charge to give rise to the transition state, a resonance-stabilized sigma complex. The aromatic system can also be activated by a suitable catalyst, such as a metal salt.[73] The leaving group in S_NAr reactions is typically a halide, and nucleofugality order of halides in S_NAr reactions is F > Cl ≈ Br > I, a reverse order compared to S_N2 reactions of aliphatic halides.[87] The rate-limiting step is the attack of the nucleophile, the following formation of the tetrahedral transition state and the breaking of the aromatic system. A simplified (i.e. without all the resonance forms illustrated), schematic of S_NAr mechanism with the electron-withdrawing group in ortho-position is illustrated in Figure 9.

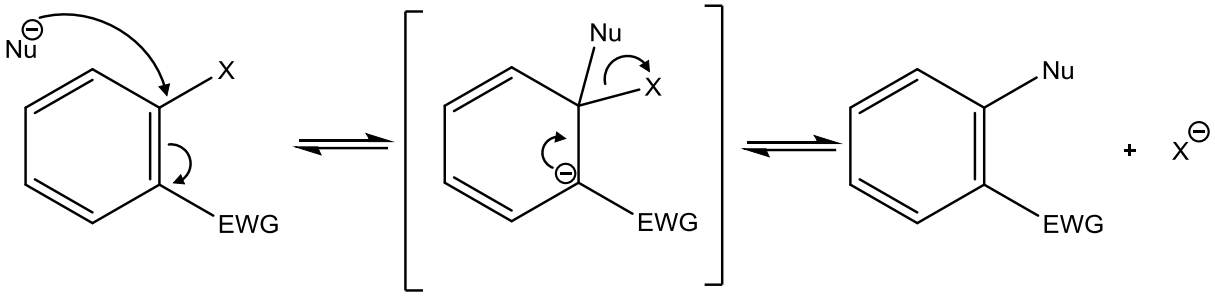

Figure 9. A schematic of S_NAr mechanism. All the possible resonance forms are not illustrated.

3.4.2. Electrophilic substitution

In electrophilic substitution a positively charged electrophile attacks an electron-rich system: as a result, a covalent bond is formed and and a positively charged leaving group is disconnected.[86] A typical leaving group in electrophilic substitution is a weak Lewis acid that is capable of existing without the pair of electrons needed to completely fill the outer electron shell: example of such a leaving group is a proton or, less commonly, a metal ion.[73] At least four major mechanisms are recognized: SE_1, SE_2 and SE_i for aliphatic compounds, and SE_{Ar} for aromatic compounds. However, most electrophilic radioiodination reactions revolve around the SE_{Ar} mechanism, and aliphatic electrophilic radioiodinations are less common, nucleophilic substitution being the vastly more commonly exploited mechanism for radioiodinating aliphatic compounds.[73]

Since positively charged iodine cannot exist in condensed form, in electrophilic radioiodinations the attacking species is a dipole, $^{\delta+}I - X^{\delta-}$, where X is an electron-withdrawing group.[73] The formation of electrophilic iodine requires an oxidizing reagent: examples of such reagents that are commonly applied are N-chloroamides, Iodogen™ and peracids.[73] A SE_{Ar} mechanism with electrophilic iodine, where Y is a leaving group and X an electron-withdrawing group, is illustrated in Figure 10.

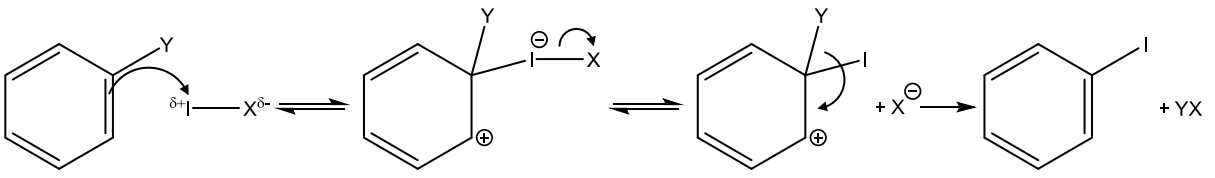

Figure 10. SE_{Ar} mechanism with electrophilic iodine.

3.4.3. Halogenations of aliphatic alkenes and alkynes

Halogens may be added to aliphatic alkenes and alkynes via addition reactions, and in the scope of this study additions of hydrogen halides or diatomic halogens are discussed. The reaction pathway resembles electrophilic substitutions, requiring a dipole as an attacking species.[86] Hydrogen halides natively exhibit dipole properties, and diatomic halogens may be polarized to induce a dipole in the molecule. The mechanism is initiated by an electrophilic attack, leading to formation of a positively charged intermediate, which then traps the nucleophile.[86] Additions of hydrogen halides and diatomic halogens are stereoselective. Hydrogen halide additions follow the Markovnikov rule; the hydrogen attacks the carbon with the least substituents. Additions of diatomic halogens lead to the formation a halonium ion, in which the positive charge is carried by the halogen atom and that are highly reactive due to the ring strain of the three-membered ring. The positively charged intermediate then captures the nucleophile, leading to the product. The mechanism with diatomic halogens proceeds via anti addition.[86] Reaction mechanisms of a hydrogen halide and diatomic halogen additions to an alkyne are demonstrated in Figure 11.

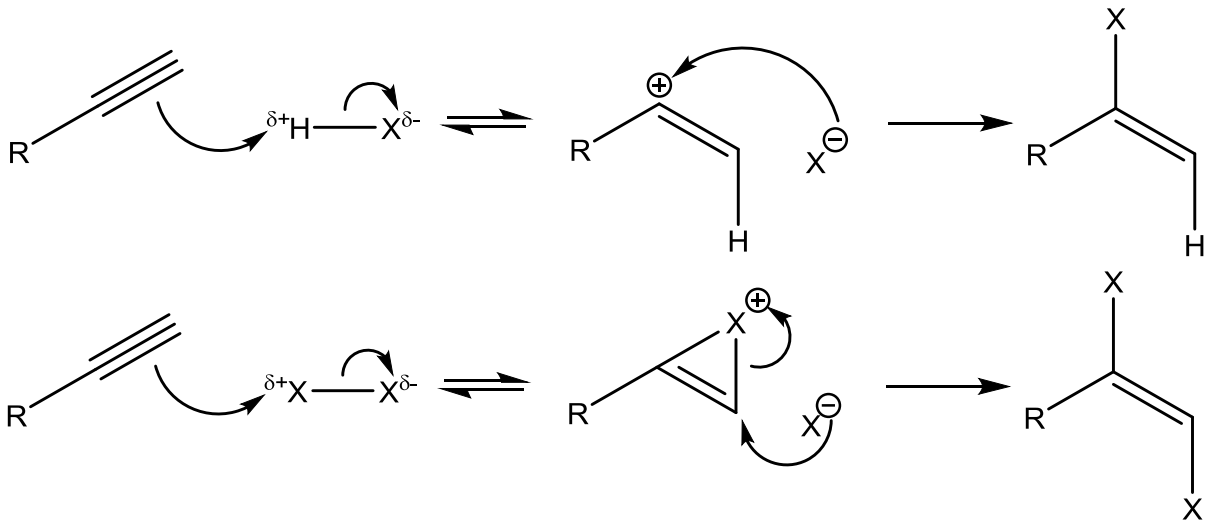

Figure 11. Addition mechanisms of a hydrogen halide and a diatomic halogen to an alkyne.

4. Experimental work

4.1 Aim of the study

Utilizing PET and SPECT in multimodality imaging of plants has notable potential which is yet to be fully realized, mostly due to limited research on suitable instrumentation and molecular tracers. The experimental part of this study describes the optimization of a radioiodination method for alkynes and testing the method on sugar analogues that are potential molecular tracers for studying plant carbohydrate metabolism with multimodality imaging. The metabolic incorporation of 6-deoxy-alkynyl glucose into plant cell walls in the root hair tips of *Arabidopsis thaliana* has been reported[88], in addition to the synthesis of a suite of similar alkynyl sugars[89]. The sugar analogues used in this study are similar alkynyl derivatives of D-glucose, and the alkynyl moiety is the targeted region of the radioiodination. Stereoselective, acid-catalyzed one-pot iodination method of alkynes with stable iodine leading to a di-iodinated product at 60 % yield has been reported[90,91], and the radioiodination method developed in this study seeks to exploit this particular reaction. Radioiodinations are typically carried out by aromatic substitution reactions, but since the carbohydrates found in plant cell walls do not generally contain aromatic structures, the aromatic ring would need to be separately incorporated into the molecule, which could affect the *in vivo* behavior of the compound due to increased steric bulk and interactions with the aromatic system. An alkynyl group has less steric bulk, and the formed iodine-aliphatic sp^2-carbon -bond is almost as stable as one with an aromatic sp^2-carbon[73]: thus, in terms of *in vivo* stability, the products are expected to be comparable to those produced by aromatic substitution, and the natural *in vivo* behavior of the compound is assumedly less affected by an additional iodoalkene moiety than an aromatic system. Iodine has radioisotopes with PET and SPECT compatible emissions, so the labelling procedure may be executed by using an iodine isotope suitable for the preferred/available imaging modality.

The experimental aim of this study was to develop a reasonably quick, selective, high-yield radioiodination method for sugar analogues with a terminal alkyne moiety and to characterize the main product(s). The experimental part consisted of optimizing the reaction conditions for iodination of a terminal alkyne by an ion exchange resin mediated reaction, comparison of this reaction to electrophilic substitution, and purification and characterization of the labelled sugar analogues. Reaction condition optimization was carried out using 4-phenyl-1-butyne, a cheap,

easily obtainable terminal alkyne that was expected to behave in a similar way as the sugar analogues, and the parameters optimized were reaction temperature, carrier amount, solvent, activation of the ion exchange resin, and minimizing the amount of water in the reaction mixture. After determining the optimal reaction conditions, the reaction was compared to electrophilic substitution using the same precursor. Finally, the radioiodination method was tested on sugar analogues for assessing radiochemical yield and characterization of the main product.

A report of the studied reaction suggest that the reaction is mediated by an *in situ* formed hydrogen iodide species[87], which, when reacting with an alkyne, would lead to an addition reaction, the main product of which being a monoiodinated Markovnikov product. However, the reported main product of the reaction is a di-iodinated species, suggesting the involvement of an *in situ* formed molecular iodine species.[90,91] Furthermore, the implication of the involvement of *in situ* formed molecular iodine suggests that electrophilic iodine I^+ may be present in the reaction mixture, and therefore one possible reaction product is a monoiodinated species resulting from an electrophilic substitution reaction between an alkyne and electrophilic iodine. A generalized reaction scheme of the studied iodination reaction is illustrated in Figure 12.

Figure 12. Generalized reaction scheme of the iodination reaction presenting possible iodinated products.

4.1.1. Reaction yield

Radionuclides used in molecular imaging characteristically have relatively short half-lives, which must be considered when working on a radiolabeling method. Ideally the method is quick, efficient and repeatable, so that high radiochemical yields may be consistently achieved in a short time as possible to minimize product loss due to decay during the labelling. The radioisotope used in this study was ^{125}I, whose half-life, 59.4 d, is long enough that no significant product loss due to radioactive decay occurs during the labeling. However, ^{125}I's

decay properties are unsuitable for *in vivo* studies, and the method needs to be suited for shorter-living radioisotopes of iodine: hence, the maximum time allocated to the reaction part of the labelling method in this study was 1 hour. This is the amount of time the sample spends in a heated shaker, and during which the majority of the product is formed. To minimize product loss due to radioactive decay when labeling with shorter-living radioisotopes of iodine, reaction time could not be extended beyond the one-hour limit, and the reaction conditions needed to be optimized in other ways in order to maximize the radiochemical yield.

Generally, reaction rates may be increased, to a certain extent, by increasing the reaction temperature. Previous studies on the Dowex®-mediated iodination of alkynes were conducted by leaving the reaction mixture to react in 65 °C overnight. [90,91] However, reaction times of radioiodinations must be significantly shorter than overnight, and it was suspected that increasing the reaction temperature to increase the reaction rate could lead to improved reaction yields during the 1 h reaction time. However, evaporation or decomposition of reactants, products or solvents may occur at high temperatures, and therefore the reaction temperature needs to be tested thoroughly to optimize the reaction conditions.

Typically, iodinations with non-radioactive iodine may be carried out by using an excess of iodine to maximize the reaction yield, but this approach is not suitable for radioiodinations, since the non-radioactive iodine will compete with radioiodine, which in turn may lead to low RCY and molar activity. Radioiodinations, however, typically utilize such a small amount of radioiodine that non-radioactive iodine needs to be added as carrier to ensure that the radioiodine behaves as expected. The optimal amount of carrier iodine was therefore set as one of the optimization parameters.

Presence of water in the reaction mixture was assumed to be disadvantageous to the reaction yield due to water's nucleophilic properties, which may interfere with the behavior of electrophilic iodine species and lead to dissociation of the HI species suspected to be involved in the addition reaction route; therefore, the evaporation of excess water in the samples was selected as an optimization parameter.

A previous report of the reaction suggests that the Dowex® resin used to facilitate the reaction could be activated with hydrochloric acid prior to drying, leading to an improved reaction yield[87]; HCl activation of Dowex® was thus set as an optimization parameter.

In summary, the parameters in reaction yield optimization were set to be reaction temperature, amount of carrier, removal of excess water, and HCl activation of Dowex® resin. In addition, the solvent of choice was expected to effect on reaction yield, although the solvent was a more essential parameter for studies involving product selectivity.

4.1.2. Product selectivity

The Dowex®-mediated reaction using 4-phenyl-1-butyne as precursor is suggested to yield three possible reaction products, which from now on will be referred to as **1**, **2** and **3**. The actual mechanism of the reaction remains ambiguous[90,91], and the following assumptions about the identity of the reacting species are based on the structure of the product. **1** is assumed to be the product of an electrophilic substitution reaction with electrophilic iodine I^+. **2** is the expected Markovnikov product formed in an addition reaction with *in situ* formed hydrogen iodide, and **3** is assumed to be an addition product of *in situ* formed molecular iodine. Structural formulas of these products are illustrated in Figure 13.

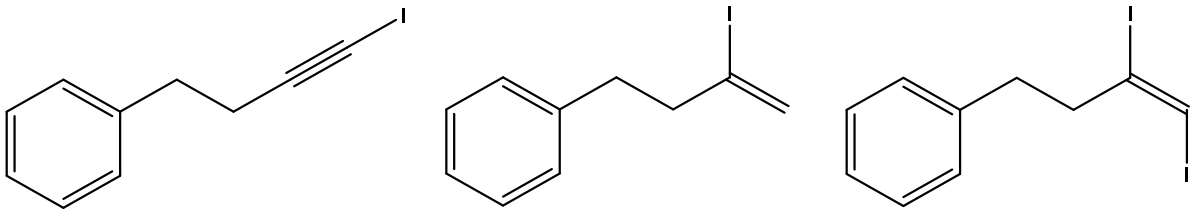

Figure 13. Structural formulas of reaction products (from left to right): **1** ((4-iodobut-3-yn-1-yl)benzene), **2** ((3-iodobut-3-en-1-yl)benzene), **3** (((E)-3,4-diiodobut-3-en-1-yl)benzene).

Due to its electronegativity and ionic radius, the iodide group is assumed to behave much like a methyl group: thus, the position and number of substitutions/additions may significantly affect the labelled compounds *in vivo* behavior. In addition, the degree of s character of the carbon in a C–I bond may significantly affect the bond strength and the compound's *in vivo* stability. Selectivity towards a single product and the possibility to modify the conditions to control the product formed are therefore desired properties of a labelling method: higher radiochemical purity may be achieved when there is only one single product formed, and the possibility to control the formed product is highly beneficial when *in vivo* behavior and stability vary significantly between different radiochemical species.

A previous study on the Dowex®-mediated reaction suggested a connection between the selected solvent's protic properties and product selectivity.[87] Polar, organic solvents with differing protic properties were selected as candidates for studies involving product selectivity.

4.1.3. Radioiodination of sugar analogues

The ultimate goal of the study was a radioiodinated sugar analogue that could be labelled with a suitable isotope of iodine to study carbohydrate metabolism in plants by SPECT or PET combined to a structural imaging modality. Two D-glucose analogues were selected as precursors for the study. Structural formulas of the precursors (from now on referred to as **4** and 2) are illustrated in Figure 14.

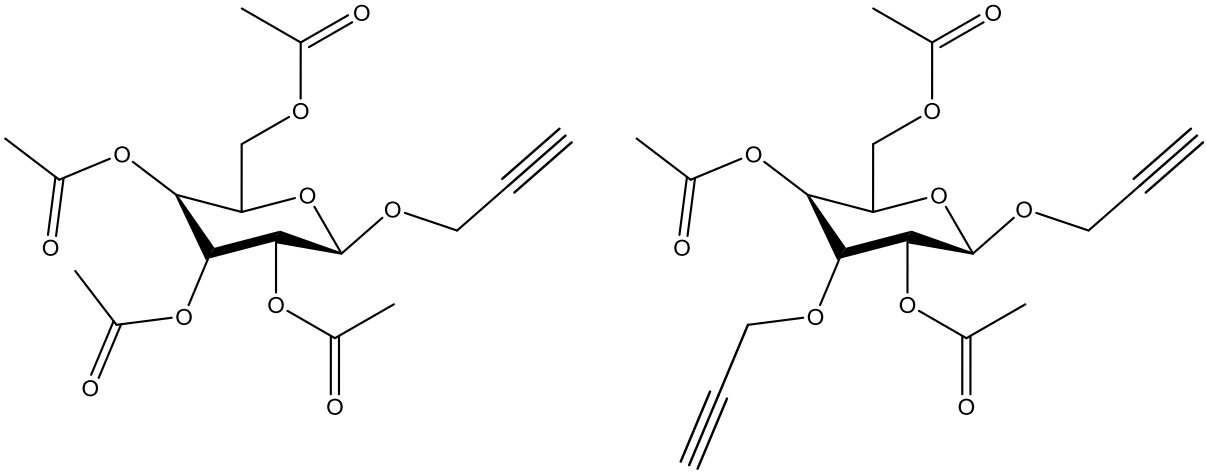

Figure 14. Structural formulas of **4** (1-(prop-2-yn-1-yloxy)-2,3,4,6-tetra-O-acetyl-D-glucose; left) and **5** (1,3-di-(prop-2-yn-1-yloxy)-2,4,6-tri-O-acetyl-D-glucose; right).

Propargyl groups are the targeted radioiodination moieties and replace some of the hydroxyl groups of the sugar analogues: at 1-position for **4**, and at 1- and 3-positions for **5**. In addition, the remaining hydroxyl groups are protected as acetyl groups to prevent unwanted side reactions during labeling.

4.2 Methods and materials

4.2.1. Materials

The list of commercially available materials used in this study is presented in Table 7. The propargyl sugars are not listed due to not being commercial products: they were synthesized by

Dr. Filip Ekholm from University of Helsinki, who kindly provided them for the purpose of developing the labeling method.

Table 7. List of commercially available materials used in this study.

Product name	CAS number	Manufacturer
4-Phenyl-1-butyne, 97 %	16520-62-0	Sigma-Aldrich
Dowex® 50WX8 hydrogen form	69011-20-7	Sigma-Aldrich
2-Propanol, anhydrous, 99.5 %	67-63-0	Sigma-Aldrich
Cyclohexanol, ReagentPlus®, 99 %	108-93-0	Sigma-Aldrich
Dimethyl sulfoxide, anhydrous, ≥99.9 %	67-68-5	Sigma-Aldrich
N,N-Dimethylformamide, anhydrous, 99.8 %	68-12-2	Sigma-Aldrich
Sodium thiosulfate, purum p.a., anhydrous, ≥98.0 %	7772-98-7	Sigma-Aldrich
Sodium iodide	7681-82-5	N/A
$Na^{125}I$, radiochem. purity 98.0 %, molar act. 80.48 GBq/mmol (carrier-free), in 0.1 M NaOH	N/A	PerkinElmer
Chloramine T trihydrate, 98 %	7080-50-4	Sigma-Aldrich
Pierce™ Iodination tubes, 12 mm x 75 mm	51592-06-4 (Iodogen®)	Thermo-Fischer Scientific

4.2.2. Radioiodination optimization

The sugar analogues were available in limited amounts: therefore, the optimization of the iodination method was carried out using 4-phenyl-1-butyne as the precursor under the assumption that adjusting the reaction parameters will lead in analogous results in terms of product yield and selectivity when using the sugar analogues as precursors. The labelling reaction parameters under optimization were: reaction temperature, carrier amount, solvent,

activation of the ion exchange resin, and minimization of water in the reaction mixture. All the experiments concerning labelling optimization were carried out according to the labelling method described above, unless stated otherwise.

4.2.2.1. Labelling method with Dowex® resin

The initial labelling method before optimization is described below. Concentration of $Na_2S_2O_3$ solution was selected as such that an excess of $Na_2S_2O_3$ compared to added carrier and ^{125}I could be added in 0.5 µL, (i.e. 3.0 µmol of NaI added -> 4µmol of $Na_2S_2O_3$ added -> concentration of $Na_2S_2O_3$ solution 8 µmol/µL). Dowex® and NaI were oven-dried for 20 hours in 120 °C before use.

50.0 ±0.5 mg of oven-dried Dowex® resin was weighed into an Eppendorf tube. 0.5 µL of aqueous NaI solution (1.2 – 5.0 µmol of NaI) and 400 µL of solvent were pipetted into the tube, the tube was closed, and the reaction mixture was vortexed. 10.8 µL of 4-phenyl-1-butyne (76.8 µmol) and 0.5 µL of ^{125}I solution (~0.5 MBq) was pipetted into the tube, and the reaction mixture was vortexed. The reaction mixture was placed into a heated shaker and was left to react in 70 – 120 °C for 1 h on 160 rpm shaking speed. The reaction mixture was cooled down to RT and the reaction was quenched with 0.5 µL of $Na_2S_2O_3$ solution. The reaction mixture was vortexed and was left to settle until the supernatant could be transferred into a clean tube by pipetting. HPLC samples and a TLC plate were prepared from the reaction mixture for analysis of results.

4.2.2.2. Resin activation

The effect of resin activation was tested by comparing the radiochemical yields of sample batches prepared using HCl-activated and non-activated resin. Activation of the resin was carried out by stirring 25 g of resin in 50 mL 2 M HCl for 0,5 hrs in room temperature, filtering the mixture and washing the residue with milli-Q –water until the pH of the filtrate was neutral. HCl-activated Dowex® was oven-dried for 20 hours in 120 °C before use.

4.2.2.3. Amount of I^- carrier

The effect of carrier amount was tested with three different amounts of carrier: 1.2, 3.0 and 5.0 µmol of NaI per sample. The carrier was introduced to the reaction mixture in the form of a

solution that was prepared from oven-dried solid NaI dissolved in milli-Q –water, and whose concentration was such that the desired amount of carrier could be added to the reaction mixture in 0.5 µL of the solution (i.e. for adding 1.2 µmol of NaI to the reaction mixture, a 2.4 µmol/µL solution was prepared). Samples for testing the effect of carrier amount were prepared with HCl-activated Dowex®.

4.2.2.4. Reaction temperature

The effect of reaction temperature on reaction yield was tested in three different temperatures: 70, 95 and 120 °C. Samples for testing the effect of carrier amount were prepared with HCl-activated Dowex® and 3.0 µmol of carrier.

4.2.2.5. Solvent

Four polar, organic solvents with differing protic properties were selected as candidates for assessing the effect solvent on reaction yield and product selectivity. The solvent effect tests were conducted by preparing the samples for resin activation, carrier amount and reaction temperature tests in these selected solvents.

4.2.2.6. Removal of excess water

The effect of minimizing water amount in the reaction mixture was carried out by comparing the radiochemical yields of samples from which excess water was evaporated prior to reaction vs. samples upon which such procedure was not executed. Water evaporation was carried out by slightly modifying the labelling method so that the carrier solution was added right after weighing the resin in the tube, and water in the solution was evaporated before adding liquid reagents to the reaction mixture. A more detailed description is described below.

4.2.3. Optimized labelling method with Dowex® resin

The labeling method after optimization is described below:

50.0 ±0.5 mg of oven-dried Dowex® resin was weighed into an Eppendorf tube. 0.5 µL (3.0 µmol) of aqueous NaI solution was pipetted on the walls of the tube, and the open tube was placed into a heating block for ~5 minutes, until the water had evaporated. 400 µL of cyclohexanol was pipetted into the tube, the tube was closed, and the reaction mixture was

vortexed. 10.8 µL of 4-phenyl-1-butyne (76.8 µmol) and 0.5 µL of ^{125}I solution (~0.5 MBq) was pipetted into the tube, and the reaction mixture was vortexed. The reaction mixture was placed into a heated shaker and was left to react in 95 °C for 1 h on 160 rpm shaking speed. The reaction mixture was cooled down to RT and the reaction was quenched with 0.5 µL (4 µmol) of $Na_2S_2O_3$ solution. The reaction mixture was vortexed and was left to settle until the supernatant could be transferred into a clean tube by pipetting. HPLC samples and a TLC plate were prepared from the reaction mixtures for analysis of results.

4.2.4. Comparison to electrophilic substitution

The Dowex®-mediated radiolabeling reaction was compared to electrophilic substitution reactions using Chloramine-T and Iodogen™ as facilitating agents. The samples were prepared using the optimized method described above, with the following exceptions: no Dowex® was used in the samples with Chloramine-T or Iodogen™; samples with Chloramine-T were prepared by pipetting 10 µL of 0.1 mg/µL Chloramine-T solution into an Eppendorf tube and evaporating the water; and samples with Iodogen™ were prepared in Pierce™ Iodination Tubes coated with Iodogen™. HPLC preparates and a TLC plate were prepared from the reaction mixtures for analysis of results.

4.2.5. Radioiodination of sugar analogues

The radioiodination of sugar analogues was executed according to the optimized labeling method, using ~10 mg of precursor. For characterization of the main product, the procedure was upscaled and executed without the addition of ^{125}I, the main product separated with HPLC, and analyzed with a 400 MHz NMR spectrometer.

4.2.6. Analysis

The samples obtained were analyzed using two different methods: a quick, qualitative method using a FLA scan of a TLC plate prepared from the samples, and a more sensitive, quantitative HPLC method. The HPLC method was used to characterize and quantify the obtained radiochemical products, and TLC was used to qualitatively confirm the results acquired by HPLC.

4.2.6.1. TLC/FLA

The TLC plate was prepared by pipetting 0.5 µL of the sample on a normal-phase, silica coated aluminum plate. The plate was then eluted with hexane, and after elution left to dry for 20 min in RT. The plate was then placed in a plastic zip-lock bag and placed in a FLA cassette. The imaging plate was placed on top of the TLC plate and left to expose from 4 hours to overnight. After sufficient exposure the imaging plate was analyzed with a FLA scanner.

4.2.6.2. HPLC

A HPLC method was developed for separating and quantifying the radioiodinated products. Samples were prepared for HPLC analysis by diluting a 40 – 50 µL aliquot of sample in 200 mL of ACN:H_2O (50:50) and filtering the preparate using a 0.2 µm PVDF syringe filter. 100 µL of preparate was the manually injected into the HPLC system with a Hamilton syringe; for some runs the injection volume was increased to provide more reliably quantifiable results. An UV-Vis detector and a NaI radiodetector were used for detection. Essential HPLC parameters are listed in Table 8, and a HPLC gradient curve representing ACN concentration over run time is illustrated in Figure 15.

Table 8. HPLC parameters of the analysis method used in the study.

Column	SymmetryPrep C18 7µm, 7.8 x 300 mm
Eluent	ACN:H_2O
Gradient	50:50->90:10
Flow rate	3 mL/min
Run time	25 min
UV-detection wavelengths	210 and 254 nm
Injection volume	100 µL

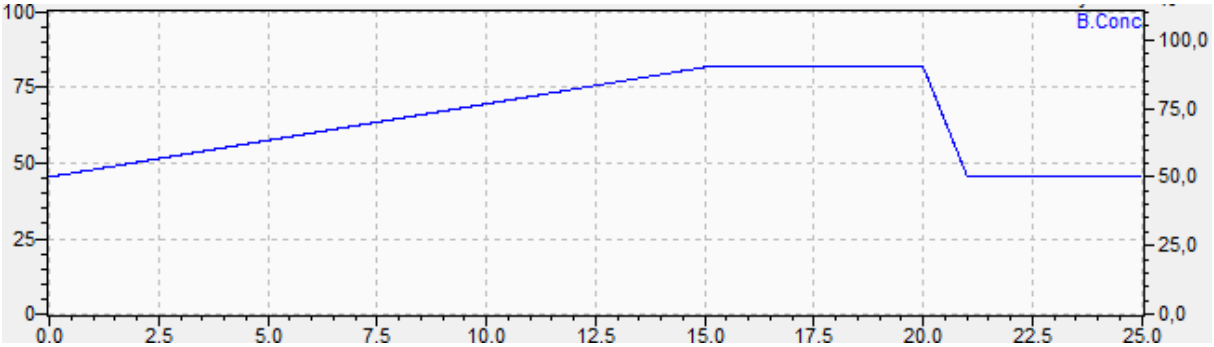

Figure 15. HPLC gradient curve representing ACN concentration (%) over run time.

Characterization of the radioiodination products of ^{125}I-iodination of 4-phenyl-1-butyne was based on HPLC analysis of samples of **1**, **2** and **3**, whose identities were confirmed with LC-MS and NMR. This analysis was conducted in reverse-phase conditions using a C18 column, a 50:50->100:0 ACN:H_2O gradient, 3 mL/min flow rate and UV detection at 210 and 254 nm. In these conditions the retention times for **1**, **2** and **3** were 9.4, 11.3 and 14.4 min, respectively, and the elution order was assumed to be the same under the conditions described in Table 8. A reference sample of **3** was analyzed in the conditions described in Table 8: in these conditions, the retention time of **3** was 19.56 min, and **1** and **2** were characterized by comparing their elution order to that of **3**.

4.2.6.3. Equations and statistical methods

The equations and statistical methods used in processing the experimental results are presented here. Radiochemical yield for a single radiochemical product was calculated according to Equation 3:

$$\mathrm{RCY} = \frac{\mathrm{A_{prod}}}{\mathrm{A_{tot}}}$$

Equation 3

where A_{prod} is the measured activity of the radiochemical product, and A_{tot} is the measured activity of all radiochemical species and free radioiodine in the sample. Total yield of all radiochemical products was calculated according to Equation 4:

$$RCY_{tot} = \sum_{i=1}^{n} \frac{A_i}{A_{tot}}$$

Equation 4

where A_i is the measured activity of a radiochemical product. Standard deviation was calculated according to Equation 5:

$$s = \sqrt{\frac{\sum_{i=1}^{n}(x_i - \bar{x})^2}{(n-1)}}$$

Equation 5

where x is the observed sample value, $\bar{x}$ is the arithmetic mean, and n is the number of samples. Standard error was calculated according to Equation 6:

$$s_{\bar{x}} = \frac{s}{\sqrt{n}}$$

Equation 6

where s is the standard deviation and n is the number of samples. Statistical analysis was conducted by using a two-tailed T-test assuming equal variances, when number of groups was two, and a two-tailed, single factor ANOVA, when number of groups was three or more; $P \leq 0.05$ was considered statistically significant.

4.3 Experiment timeline

Timeline and reaction parameters of the experiments are presented in Table 9

Table 9. Experiment timeline.

Experiment / Parameters	Dowex activation	Carrier amount	Reaction temperature	Water evaporation	Comparison to electrophilic reaction	Radioiodination of sugar analogues
Dowex activation	Y/N	Y				
Carrier amount (µmol)	1.2	1.2, 3.0, 5.0	3		3	
Reaction temperature (°C)	70		70, 95, 120		95	
Solvent	cyclohexanol, 2-propanol, DMSO, DMF				cyclohexanol	
Water evaporation	N			Y/N	Y	
time →						

5. Results and discussion

5.1 Optimization of the radioiodination method

The results for labeling optimization are presented in this chapter. The error bars in the graphs represent the standard error of mean. Quantitative results are based on radio-HPLC analysis of the samples. Retention time of **3** was determined by analysis of a reference sample of **3**, and **1** and **2** were identified by their expected elution order of **1**, **2** and **3**. A summary of the optimization results can be found in Attachment 1. Radio-HPLC results of method optimization. A radio-HPLC chromatogram demonstrating the retention times of free $^{125}I^-$, [^{125}I]**1**, [^{125}I]**2** and [^{125}I]**3** is presented in Figure 16.

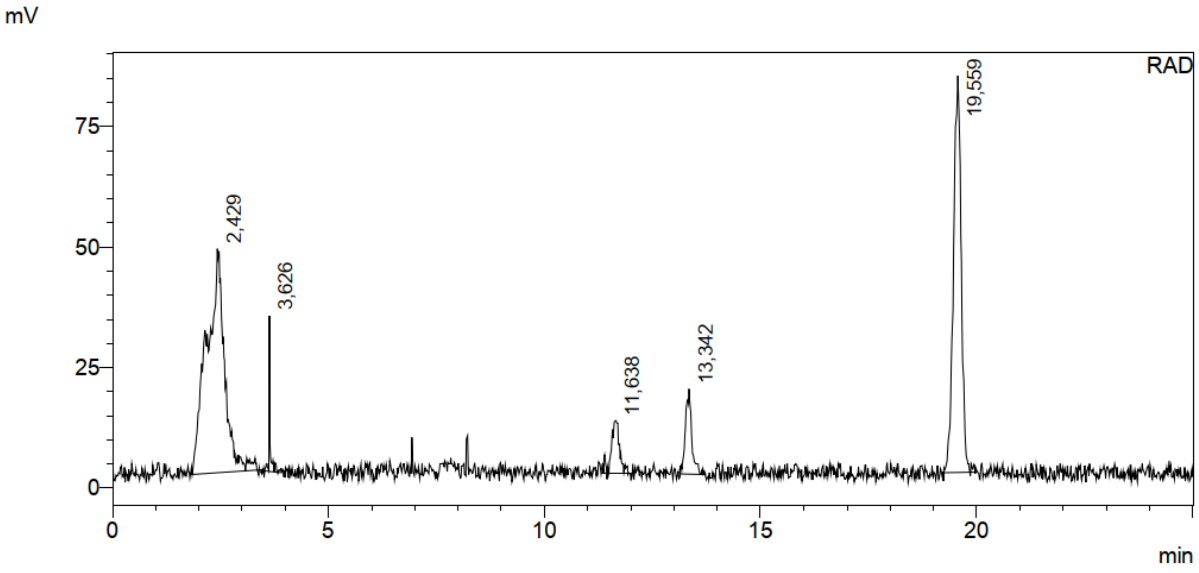

Figure 16. Radio-HPLC chromatogram demonstrating the retention times of free $^{125}I^-$ (2.429 min), [^{125}I]**1** (11.638 min), [^{125}I]**2** (13.342 min) and [^{125}I]**3** (19.559 min). The radiopeak at 3.626 min appeared inconsistently in the chromatograms and is most likely caused by interference. The sample that the chromatogram represents was prepared under the following conditions: reaction time 60 min, solvent cyclohexanol, reaction temperature 70 °C, amount of carrier 3.0 µmol, Dowex® HCl-activated, no excess water evaporated. This particular chromatogram was selected as an example, because it shows clearly all the relevant radiopeaks, i.e. those associated with free $^{125}I^-$, [^{125}I]**1**, [^{125}I]**2** and [^{125}I]**3**.

5.1.1. Resin activation

The effect of Dowex® HCl activation on the amount of formed ^{125}I-labeled products was tested in different solvents in two separate sample batches, the other prepared with non-activated resin and the other with HCl-activated resin: the assumption was that using HCl-activated Dowex® leads to higher yield of radiochemical products than when using non-activated Dowex®. The samples in were prepared in triplicate in 70 °C with 1.2 µmol of carrier. The results are presented as the average of the sum of all radioiodinated products in in Figure 17.

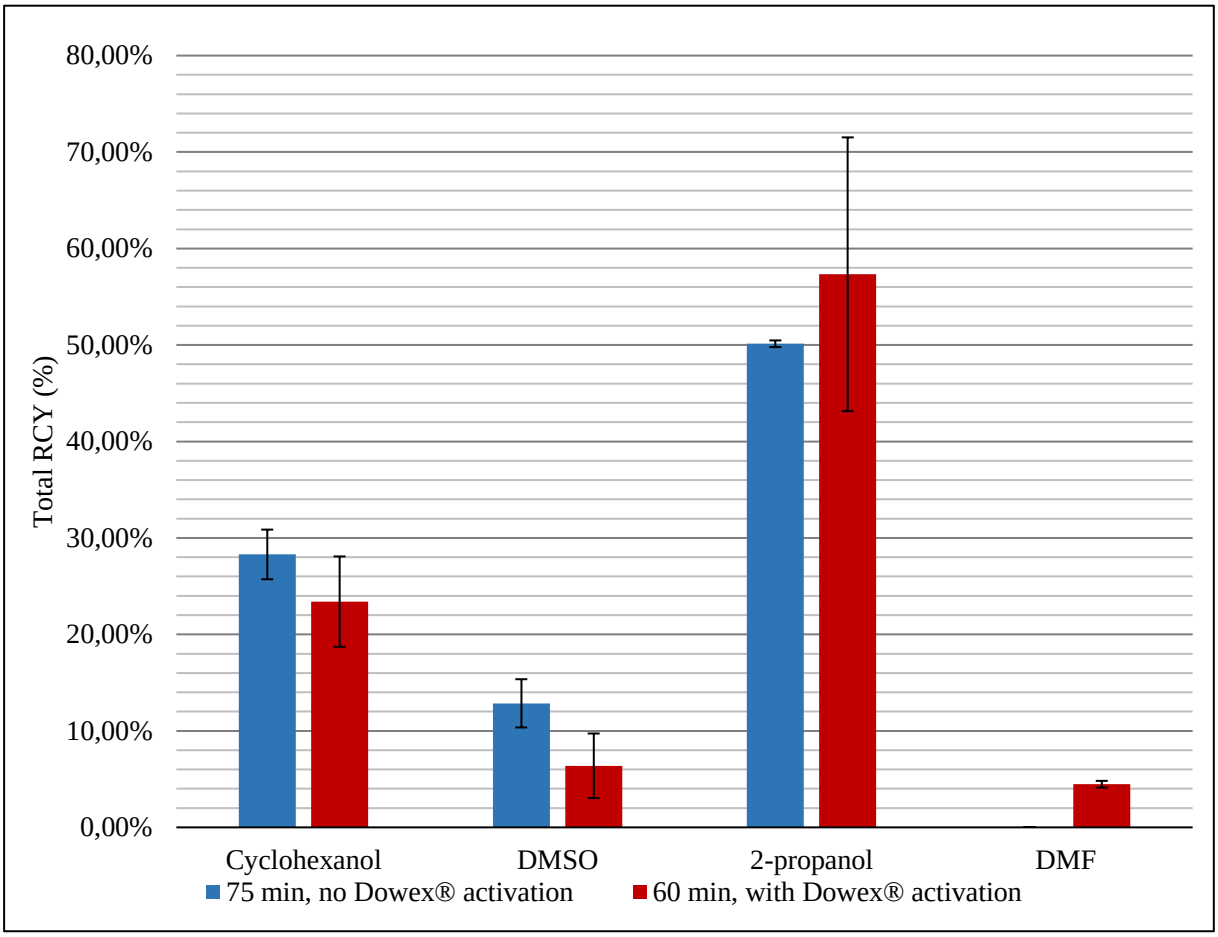

Figure 17. The effect of Dowex® HCl activation on the amount of formed ^{125}I-labeled products in ^{125}I -iodination of 4-phenyl-1-butyne in different solvents. In cyclohexanol and DMSO a slight decrease in formation of radioiodinated products is observed due to the activation, from 28.3 ±3.6 to 23.4 ±4.7 % and from 12.9 ±4.3 to 6.4 ±3.4 %, respectively, whereas in 2-propanol and DMF the effect is opposite, and the amount of radioiodinated products is increased from 50.1 ±0.5 % to 57.3 ±14.2 % and from 0 % to 4.47 ±0.4 %, respectively.

In cyclohexanol and DMSO, the amount of formed radioiodination products decreased with Dowex® HCl activation; however, it should be noted that the final reaction time for the batch without HCl-activated Dowex® was 15 min longer, which may have led to the higher yield. For 2-propanol the effect of Dowex® HCl activation was opposite, and in DMF the test batch without HCl-activated Dowex® yielded no quantifiable amounts of radioiodinated products. Dowex® HCl activation did not lead to a statistically significant increase in amount of formed radioiodination products in any of the solvents used. However, there are reports that comparable or even higher yields have been obtained with HCl-activated Dowex®[90], so activation was carried out in further experiments.

5.1.2. Amount of I^- carrier

The effect of the amount of I^- carrier on the amount of formed ^{125}I-labeled products in ^{125}I-iodination of 4-phenyl-1-butyne was tested with three separate sample batches and in four different solvents. The samples were prepared in triplicate in 70 °C with 60 min reaction time and with HCl-activated Dowex®. The results are presented as the average of the sum of radioiodinated products in each sample in Figure 18.

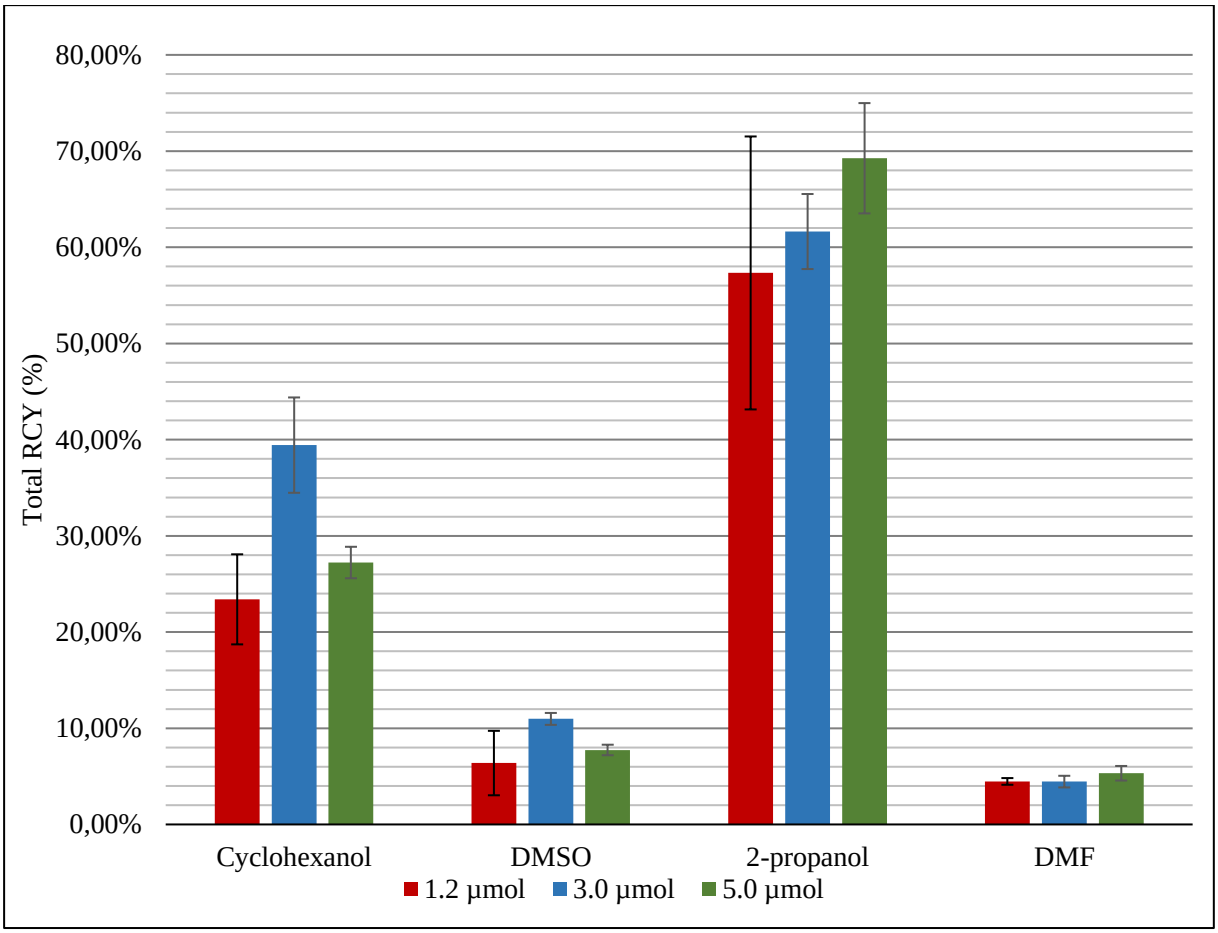

Figure 18. The effect of I^- carrier amount on the amount of formed ^{125}I-labeled products in ^{125}I-iodination of 4-phenyl-1-butyne in different solvents. In cyclohexanol and DMSO the highest yield of radioiodinated products was obtained with 3.0 µmol of NaI carrier (39.4 ±8.6 % and 11.0 ±1.1 %, respectively), while in 2-propanol and DMF the highest yield of radioiodinated products was achieved with 5.0 µmol of NaI (69.3 ±9.9 % and 5.3 ±1.1 %, respectively).

In cyclohexanol and DMSO, using 3.0 µmol of I^- carrier resulted in the highest average yield of radioiodinated products. In 2-propanol and DMF the highest average yield of radioiodinated products was achieved with 5.0 µmol of I^- carrier. In cyclohexanol the amount of I^- carrier had a statistically significant effect on the amount of radioiodinated products formed, while in the other tested solvents the effect was not statistically significant. Further experiments were carried out using 3.0 µmol of I^- carrier.

5.1.3. Reaction temperature

The effect of reaction temperature on the amount of formed ^{125}I-labeled products in ^{125}I-iodination of 4-phenyl-1-butyne was tested with three separate sample batches and in four different solvents. The samples were prepared in triplicate with 60 min reaction time, 3.0 µmol of I^- carrier and HCl-activated Dowex®. The results are presented as the average of the sum of radioiodinated products in Figure 19.

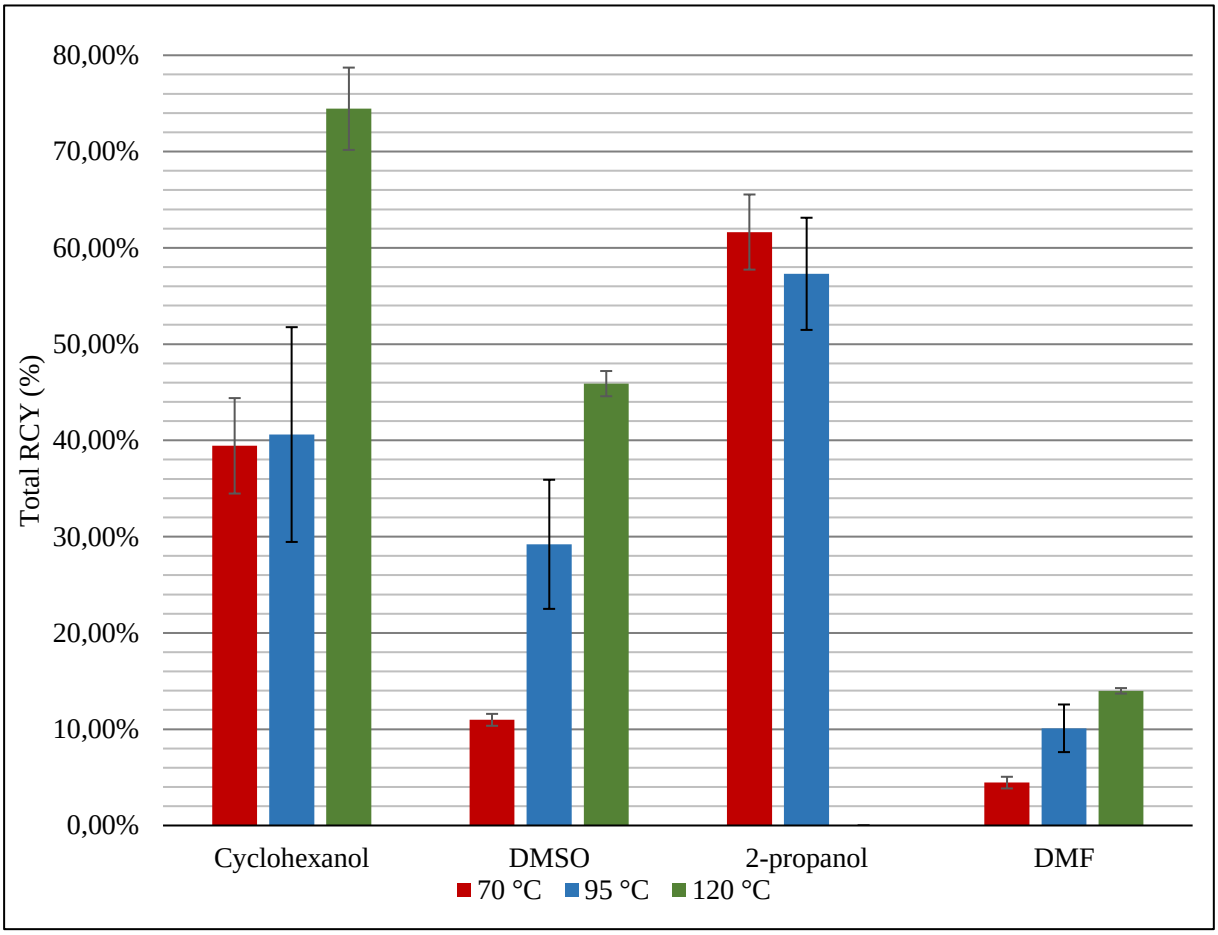

Figure 19. The effect of reaction temperature on the amount of formed ^{125}I-labeled products in ^{125}I-iodination of 4-phenyl-1-butyne in different solvents. In cyclohexanol, DMSO and DMF the highest yields of radioiodinated products were achieved in 120 °C (74.4 ±7.4 %, 45.9 ±2.3 % and 14.0 ±0.5 %, respectively); in 2-propanol the highest yield of radioiodinated products, 61.6 ±6.8 %, was achieved in 70 °C.

The highest amount of radioiodinated products was formed in 120 °C, except in 2-propanol, in which the highest amount of radioiodinated products was achieved in 75 °C . Results for 2-

propanol in 120 °C could not be obtained due to 2-propanol's boiling point of 82.5 °C, which led to almost complete solvent evaporation in 120 °C: thus, the amount of formed radioiodinated products could not be measured in these conditions. Variance analysis suggested the reaction temperature has a statistically significant effect on formation of radioiodinated products, except in 2-propanol, where such an effect could not be observed. Due to working safety concerns (the Eppendorf tubes used in the study have a nominal heat tolerance up to 100 °C[92]) further experiments were carried out in 95 °C.

5.1.4. Solvent

^{125}I-iodination of 4-phenyl-1-butyne was tested in four different solvents to study the solvent's effect on regioselectivity of the radioiodination and the radiochemical yield of individual products. Effect of reaction parameters on yield of radioiodinated products has been discussed earlier, and this section is more focused on product selectivity. The study on solvent effects used the same data set obtained in reaction temperature and carrier tests, and the results are presented as an average of the radiochemical yields of individual products, summed into a single column.

5.1.4.1. Cyclohexanol

The effect of amount of I^- carrier on formation of ^{125}I-labeled products in ^{125}I-iodination of 4-phenyl-1-butyne in cyclohexanol is illustrated in Figure 20. The samples were prepared in triplicate, using HCl-activated Dowex® in 70 °C reaction temperature and 60 min reaction time.

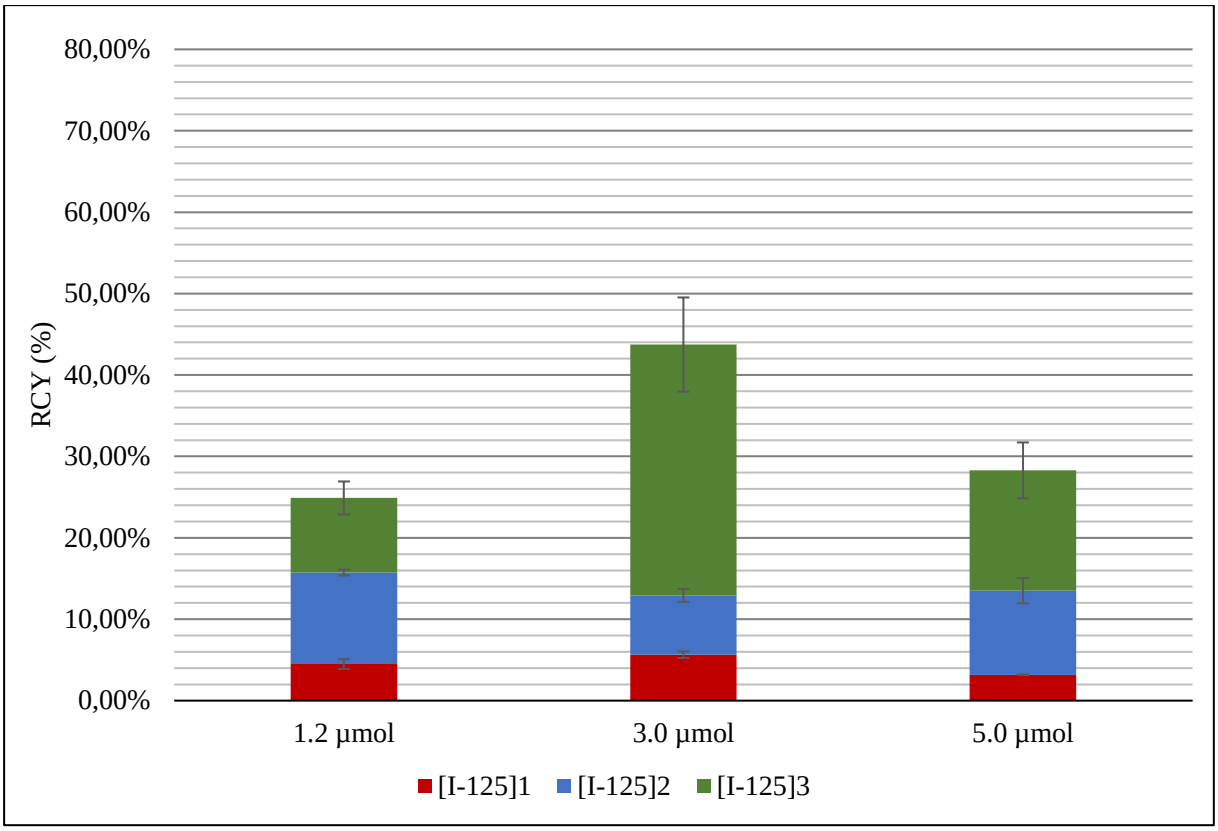

Figure 20. The effect of amount of I^- carrier on formation of ^{125}I-labeled products in ^{125}I-iodination of 4-phenyl-1-butyne in cyclohexanol. Highest RCY and regioselectivity were achieved with 3.0 µmol of I^- carrier, and yielded in main product [^{125}I]**3** at 30.8 ±5.8 % yield and a total yield of radiochemical products of 39.4 ± 5.0%.

The results display a tendency to favor the di-iodinated [^{125}I]**3** when 3.0 µmol of carrier was used, and the sum of average radiochemical yields was also highest under these conditions. With 1.2 and 5.0 µmol of carrier the results were highly similar in terms of product distribution and yield.

The effect of reaction temperature on formation of ^{125}I-labeled products in ^{125}I-iodination of 4-phenyl-1-butyne in cyclohexanol is illustrated in Figure 21. The samples were prepared in triplicate, using HCl-activated Dowex®, 3.0 µmol of I^- carrier and 60 min reaction time.

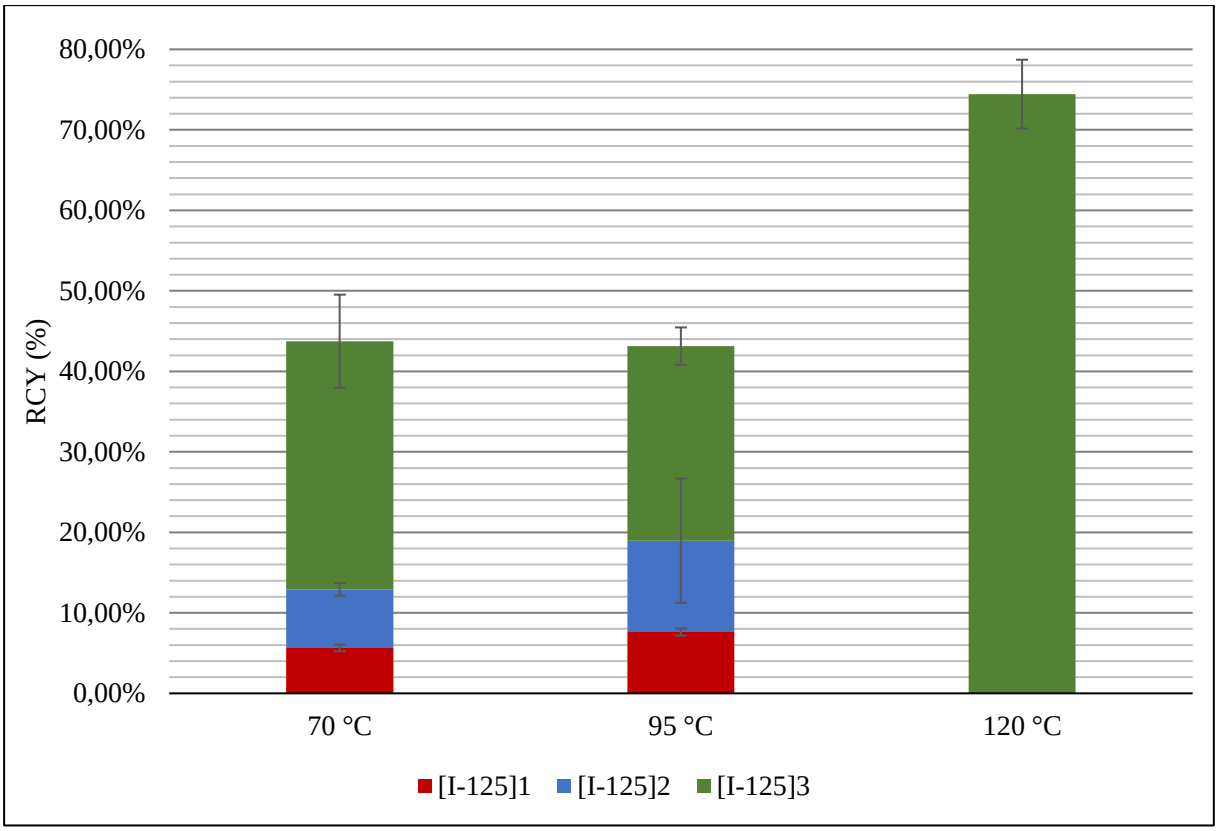

Figure 21. The effect of reaction temperature on formation of ^{125}I-labeled products in ^{125}I-iodination of 4-phenyl-1-butyne in cyclohexanol. Highest RCY and product selectivity were achieved in 120 °C: main product yield [^{125}I]**3** was 74.4 ±7.4 %, with no other radioiodinated chemical species present in measurable amounts.

In 70 and 95 °C the results are highly similar in terms of product distribution and amount of formed radioiodinated products, the favored product being [^{125}I]**3**. In 120 °C the results display a significantly increased yield, as well as a complete selectivity towards [^{125}I]**3**. A radio-HPLC chromatogram and associated peak data demonstrating the high yield and selectivity achieved in cyclohexanol in 120 °C is presented in Figure 22.

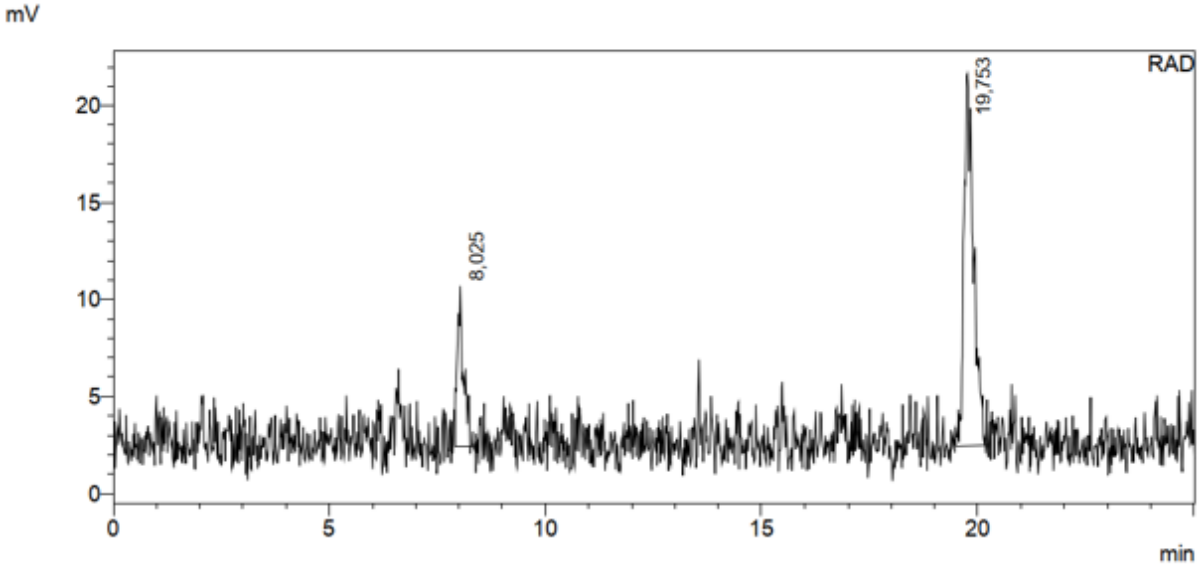

RAD

Peak#	Ret. Time	Area	Height	Conc.
1	8,025	82342	8254	21,846
2	19,753	294585	19164	78,154
Total		376926	27418	

Figure 22. Radio-HPLC chromatogram and associated peak data of a sample prepared in cyclohexanol, in 120°C, using HCl-activated Dowex®, 3.0 µmol of I^- carrier and 60 min reaction time. [^{125}I]**3** peak with an area corresponding to 78.154 % RCY is found at 19.753 min. A noticeable feature in the chromatogram is the absence of the radiopeak associated to free radioiodine. In addition, a peak associated with an unidentified radioiodination side product can be found at 8.023 min; this side product appeared inconsistently in the samples, typically in low yields, and was thus left unidentified.

5.1.4.2. DMSO

The effect of amount of I^- carrier on formation of ^{125}I-labeled products in ^{125}I-iodination of 4-phenyl-1-butyne in DMSO is illustrated in Figure 23. The samples were prepared in triplicate, using HCl-activated Dowex® in 70 °C reaction temperature and 60 min reaction time.

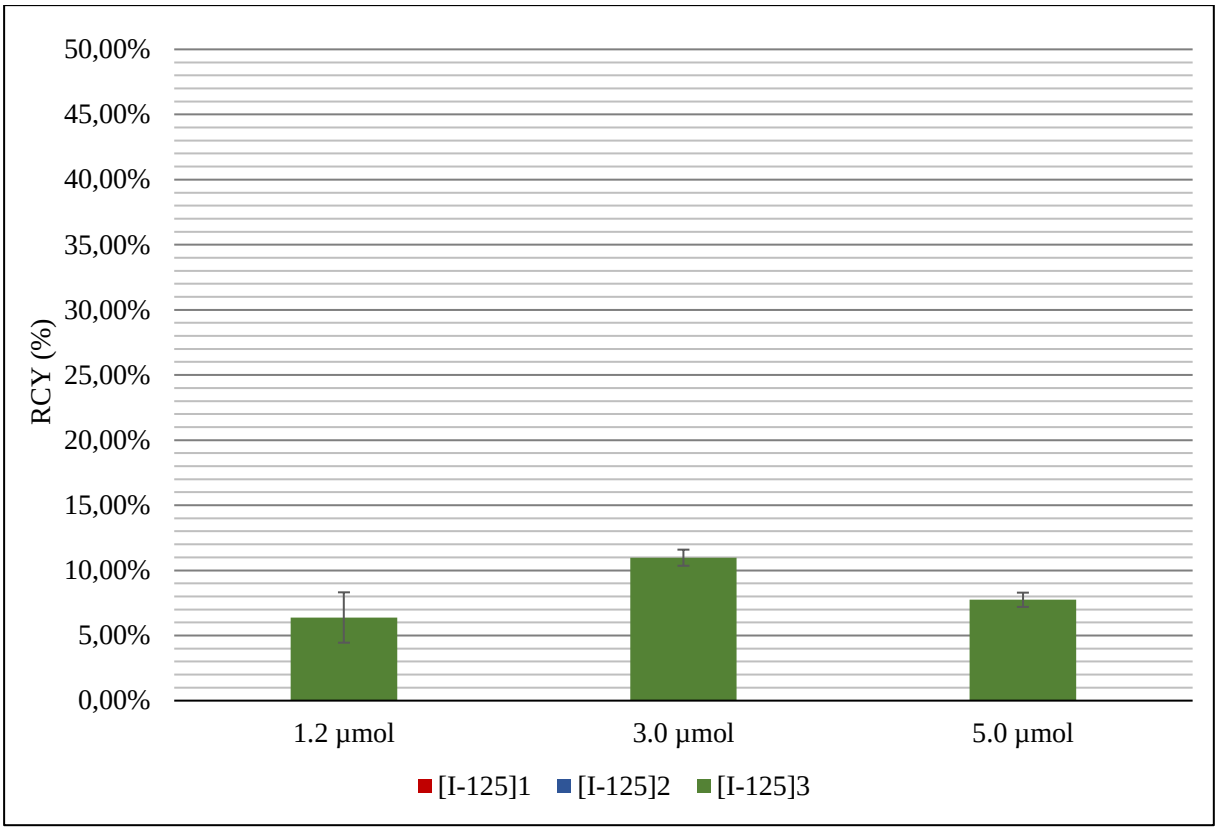

Figure 23. The effect of amount of I^- carrier on formation of ^{125}I-labeled products in ^{125}I-iodination of 4-phenyl-1-butyne in DMSO. With all tested carrier amounts the reaction favored the di-iodinated product [^{125}I]**3**, with no other radioiodinated products formed in measurable amounts. Highest RCY of [^{125}I]**3**, 11.0 ±1.1 %, was achieved with 3.0 µmol of carrier.

In DMSO the reaction appears to have complete selectivity towards [^{125}I]**3**. However, it should be noted that the overall yield was low with all tested amounts of carrier, and other radiochemical species may have formed in undetectable and -quantifiable amounts.

The effect of reaction temperature on formation of ^{125}I-labeled products in ^{125}I-iodination of 4-phenyl-1-butyne in DMSO is illustrated in Figure 24. The samples were prepared in triplicate, using HCl-activated Dowex®, 3.0 µmol of I^- carrier and 60 min reaction time.

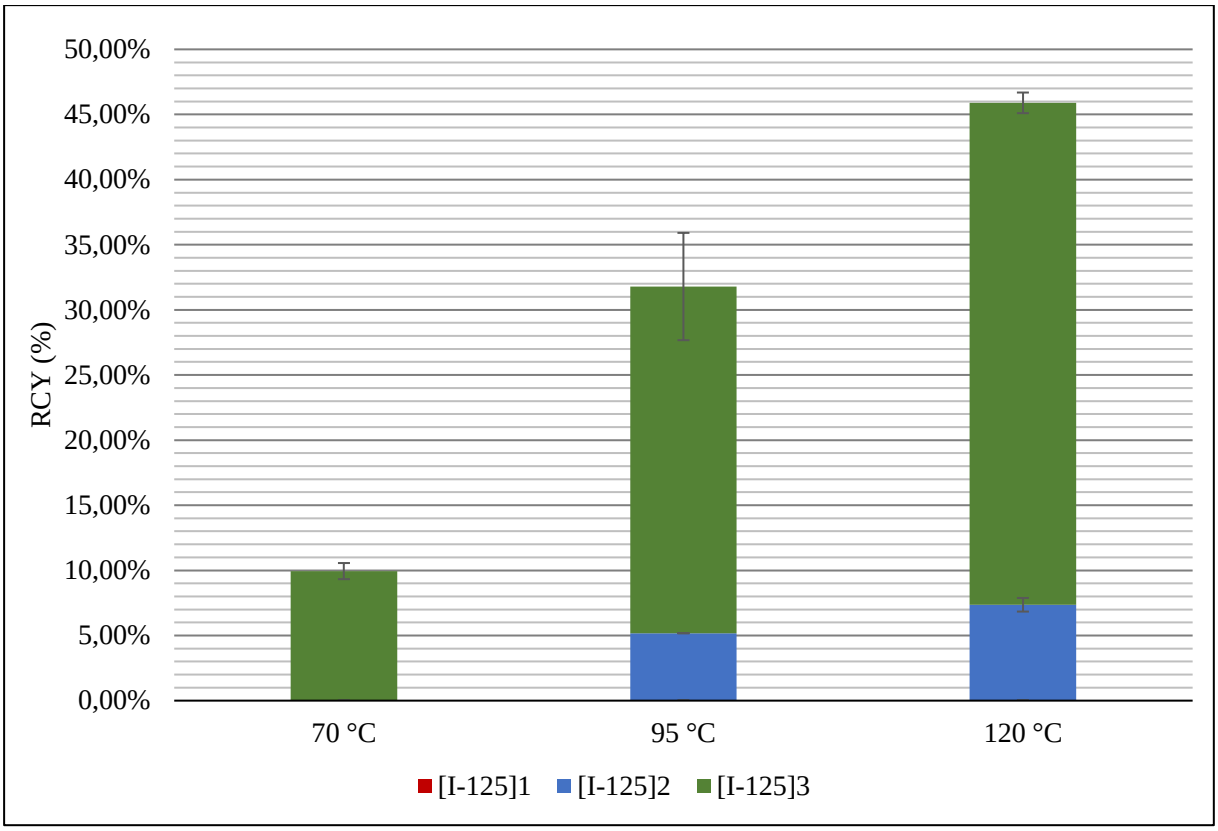

Figure 24. The effect of reaction temperature on formation of ^{125}I-labeled products in ^{125}I-iodination of 4-phenyl-1-butyne in DMSO. Highest RCY and product selectivity were achieved in 120 °C: RCY of the main product [^{125}I]**3** was 38.5 ±0.8 %, and the total amount of formed radioiodination products was 45.9 ±1.3 %.

In DMSO the reaction appears to retain its selectivity towards [^{125}I]**3**, with some [^{125}I]**2** forming in quantifiable amounts in 95 and 120 °C. Increasing the temperature resulted in a statistically significant increase in the yield of radioiodinated products.

5.1.4.3. 2-propanol

The effect of amount of I^- carrier on formation of ^{125}I-labeled products in ^{125}I-iodination of 4-phenyl-1-butyne in 2-propanol is illustrated in Figure 25. The samples were prepared in triplicate, using HCl-activated Dowex® in 70 °C reaction temperature and 60 min reaction time.

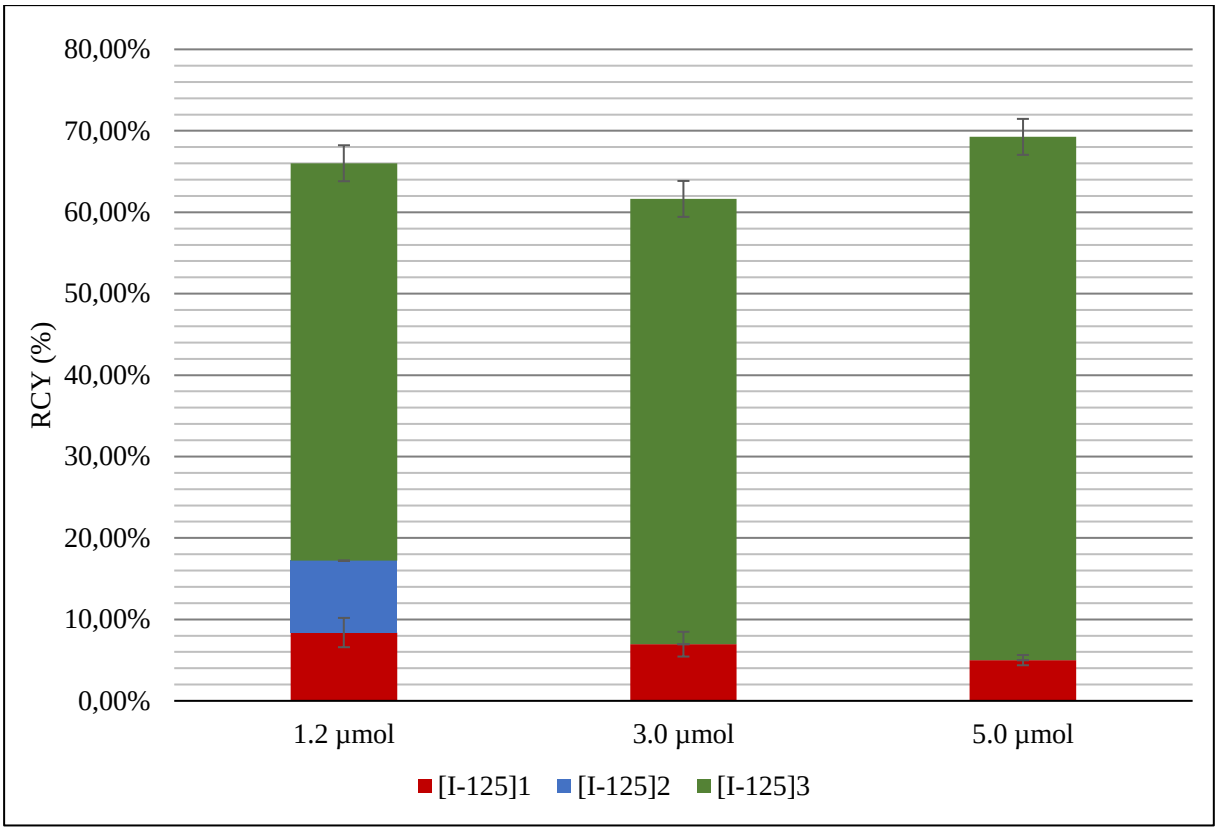

Figure 25. The effect of amount of I^- carrier on formation of ^{125}I-labeled products in ^{125}I-iodination of 4-phenyl-1-butyne in 2-propanol. Highest RCY and product selectivity were achieved with 5.0 µmol of carrier: RCY of the main product[^{125}I]**3** was 64.3 ±6.4 %, and the total amount of formed radioiodination products was 69.3 ±5.7 %.

In 2-propanol the reaction displays a rather uniform yield and product distribution with all tested amounts of carrier, with notable selectivity towards [^{125}I]**3**. [^{125}I]**2** was detectable only in the samples with 1.2 µmol of carrier: however, the detected amount was relatively low, and it can be assumed that [^{125}I]**2** was formed in unquantifiably small amounts with all tested amounts of carrier.

The effect of reaction temperature on formation of ^{125}I-labeled products in ^{125}I-iodination of 4-phenyl-1-butyne in 2-propanol is illustrated in Figure 26. The samples were prepared in triplicate, using HCl-activated Dowex®, 3.0 µmol of I^- carrier and 60 min reaction time.

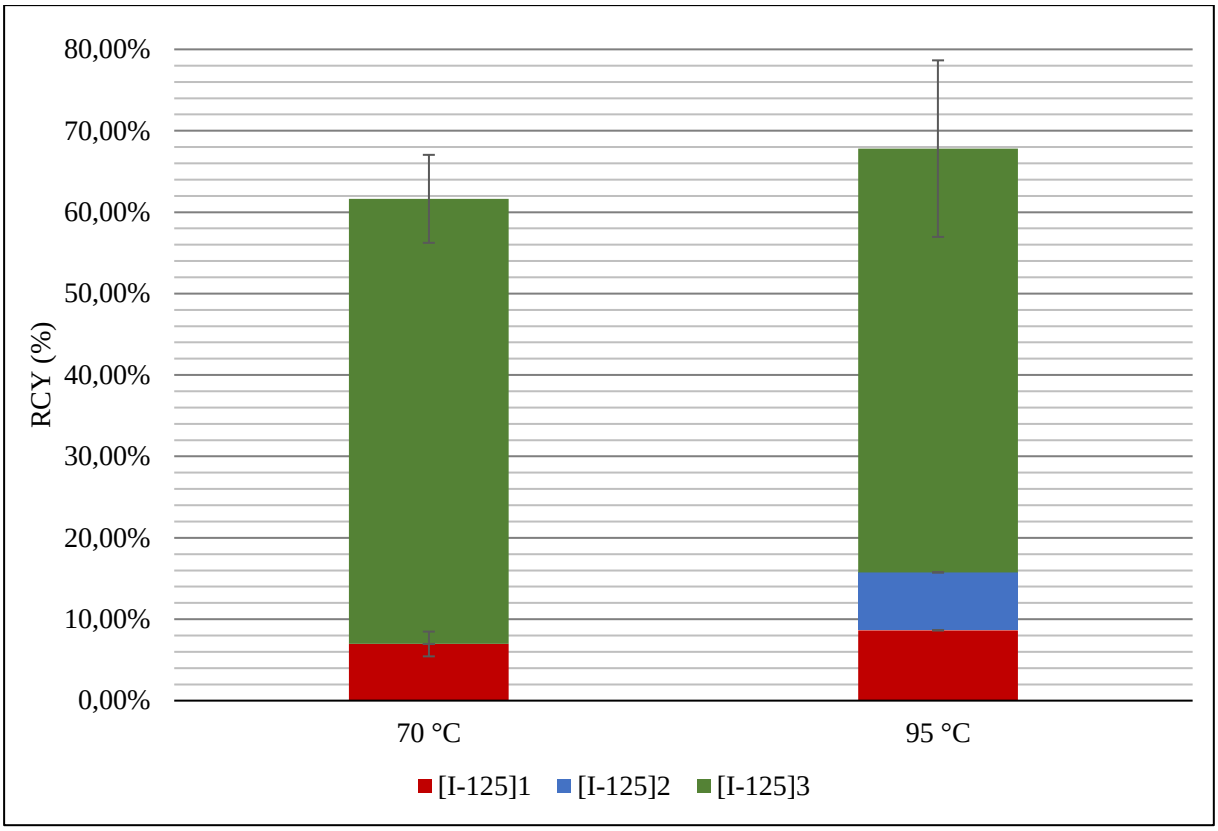

Figure 26. The effect of reaction temperature on formation of ^{125}I-labeled products in ^{125}I-iodination of 4-phenyl-1-butyne in 2-propanol. Highest amount of formed radioiodination products, 57.3 ±5.9 %, was achieved in 95°C; however, RCY of the main product [^{125}I]**3** does not differ significantly between 70 °C and 95 °C (54.7 ±5.4 and 52.1 ±10.8 %, respectively).

The reaction temperature does not appear to have a significant effect on product distribution or radiochemical yield in 2-propanol. The favored reaction product is [^{125}I]**3**, with small amounts of [^{125}I]**1**. [^{125}I]**2** was detected in 95 °C, but as before, the amount was relatively small, and an unquantifiably small amount of [^{125}I]**2** may be present in samples made in 70 °C. As before noted, reaction in 2-propanol could not be tested in 120 °C due to solvent evaporation.

5.1.4.4. DMF

The effect of amount of I^- carrier on formation of ^{125}I-labeled products in ^{125}I-iodination of 4-phenyl-1-butyne in DMF is illustrated in Figure 27. The samples were prepared in triplicate, using HCl-activated Dowex® in 70 °C reaction temperature and 60 min reaction time.

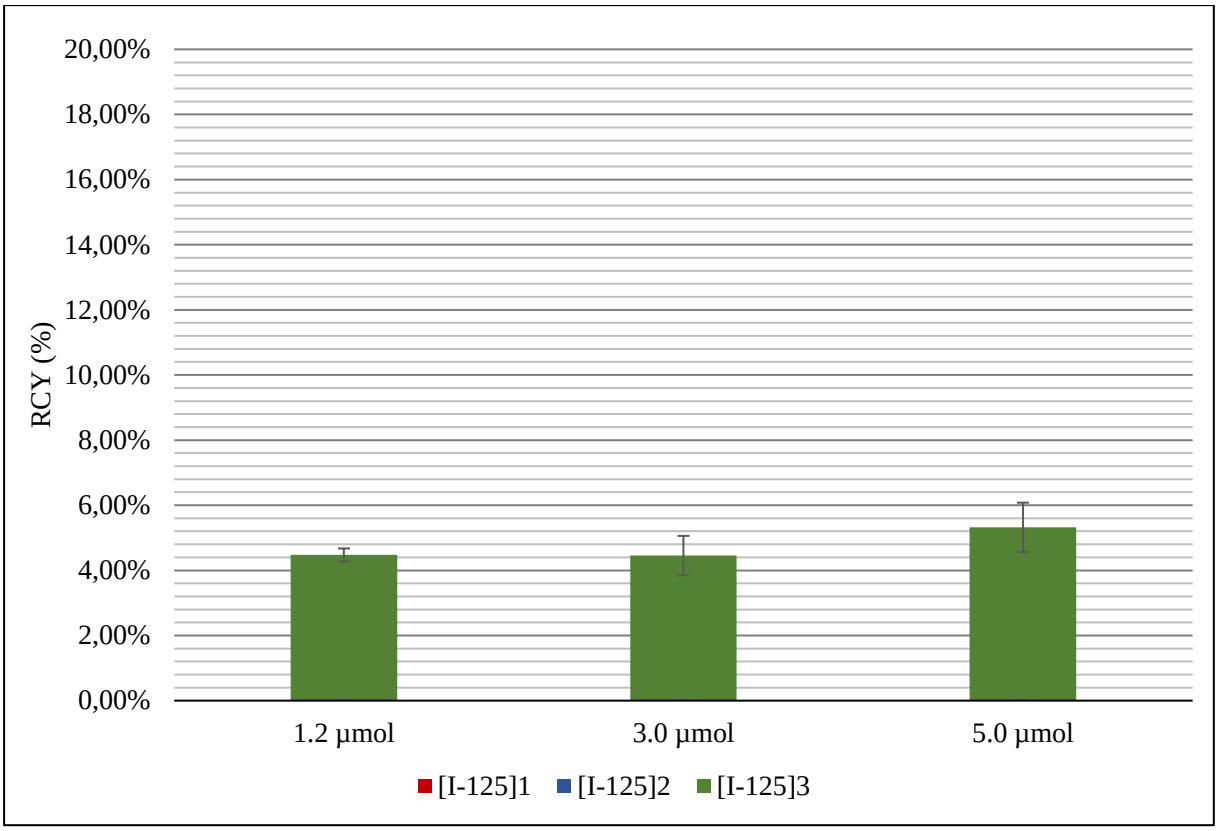

Figure 27. The effect of amount of I^- carrier on formation of ^{125}I-labeled products in ^{125}I-iodination of 4-phenyl-1-butyne in DMF. Only the di-iodinated product [^{125}I]**3** was formed in measurable amounts with all carrier amounts, and the highest RCY of [^{125}I]**3**, 5.32 ±0.8 % was achieved with 5.0 µmol of carrier.

The amount of carrier appears to have an insignificant effect on product distribution and radiochemical yield in DMF. The reaction displays a complete selectivity towards [^{125}I]**3**, although it is to be noted that the overall radiochemical yield is low, and other radiochemical species may have formed in undetectable and -quantifiable amounts.

The effect of reaction temperature on formation of ^{125}I-labeled products in ^{125}I-iodination of 4-phenyl-1-butyne in DMF is illustrated in Figure 28. The samples were prepared in triplicate, using HCl-activated Dowex®, 3.0 µmol of I^- carrier and 60 min reaction time.

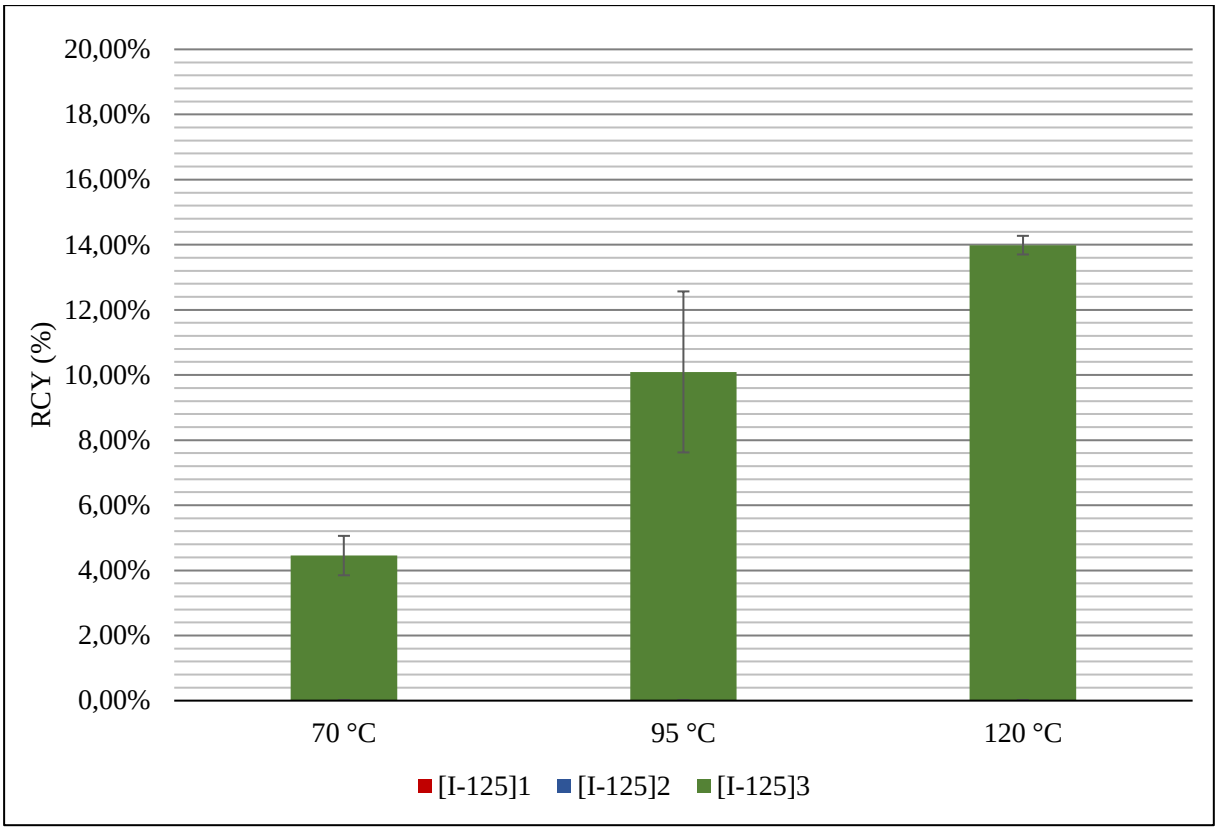

Figure 28. The effect of reaction temperature on formation of ^{125}I-labeled products in ^{125}I-iodination of 4-phenyl-1-butyne in DMF. Only the di-iodinated product [^{125}I]**3** was formed in measurable amounts in all temperatures, and the highest RCY of [^{125}I]**3**, 14.0 ±0.3 %, was achieved in 120 °C.

The reaction retains its observable selectivity towards [^{125}I]**3** with increasing temperature. Significant increase in radiochemical yield is also displayed with increasing temperature.

5.1.5. Evaporation of excess water

The effect of evaporating excess water from the samples on amount of formed radioiodinated products was studied with two sample batches, the other prepared with excess water evaporation and the other without. The samples were prepared in triplicate in cyclohexanol, using HCl-activated Dowex®, 3.0 µmol of carrier and 95 °C reaction temperature. The results are presented in Figure 29.

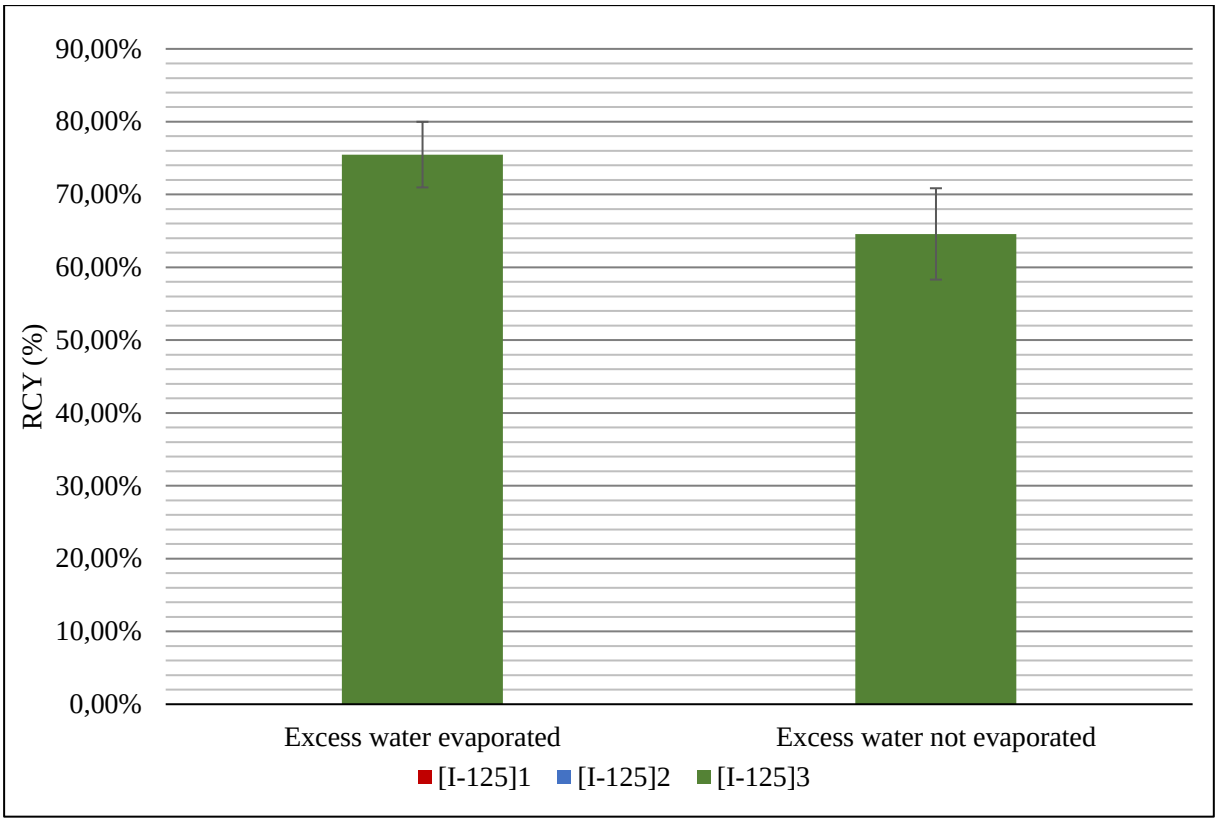

Figure 29. The effect of evaporation of excess water on the amount of formed radioiodination products in ^{125}I-iodination of 4-phenyl-1-butyne in cyclohexanol. The only radioiodination product formed in these conditions was [^{125}I]**3**, and an increase in RCY of [^{125}I]**3**was observed when excess water was evaporated from the sample: RCY of [^{125}I]**3** increased from 64.6 ±6.3 % to 75.5 ±4.5 when excess water was evaporated.

The results display an observable increase in the amount of formed radioiodination products when excess water is removed. However, the difference is not statistically significant.

5.1.6. Summary of radioiodination method optimization

Different carrier amounts were tested to study the carrier's effect on the amount of formed radioiodination products. In cyclohexanol and DMSO, 3.0 µmol of carrier resulted in the highest amount of ^{125}I-iodinated products, and in 2-propanol and DMF the highest amount of ^{125}I-iodinated products was reached with 5.0 µmol of carrier. The carrier effect was more pronounced in cyclohexanol and DMSO. The amount of carrier did not have a statistically significant effect on yield of ^{125}I-iodinated products, except in cyclohexanol, where 3.0 µmol of carrier resulted in the highest yield of ^{125}I-iodinated products. The results suggest that carrier

amounts higher than 3.0 µmol lead to the carrier competing with ^{125}I in the radioiodination reaction, leading to decreased yield of radioiodination products. Amount of carrier was not expected to affect regioselectivity of the radioiodination, and neither is this effect observed in the data.

Different reaction temperatures were tested to assess the temperature effect on formation of radioiodinated products. In the tested reaction temperatures, the amount of formed radioiodination products displayed a statistically significant increase with increasing temperature in all solvents (except 2-propanol), and the highest amounts of formed radioiodination products were obtained in 120 °C. Reactions in 2-propanol were an exception to the aforementioned, and in 2-propanol radiolabelings in 70 °C and 95 °C produced comparable and similar yields of radiochemical products. Due to 2-propanol's relatively low boiling point the reaction could not be tested in 120 °C in 2-propanol. Reaction temperature did not appear to have an observable effect on regioselectivity of the radioiodination products in DMSO, 2-propanol and DMF: in cyclohexanol selectivity towards [^{125}I]**3** increased with increasing temperature.

Reactions in protic solvents generally displayed higher radiochemical yields and wider reaction product diversity than those in aprotic solvents; however, as noted before, the observed higher selectivity in aprotic solvents may simply be a result of an overall low radiochemical yield, and other radioiodinated reaction products may have formed, although in undetectable and unquantifiable amounts. The reaction displayed regioselectivity towards the same di-iodinated product **3** under all conditions, with aprotic solvents being more selective than protic. In summary, protic solvents displayed more favorable results than aprotic.

HCl activation of Dowex® and removal of excess water displayed a slight increase in the amount of formed radioiodination products, although the difference was not statistically significant in either case. It was, however, decided to integrate these procedures into the sample preparation protocol.

Overall, the repeatability of the radioiodination method seems sufficient, and in the last two sample sets prepared under the optimal conditions the standard deviation of RCY of [^{125}I]**3** was ≤ 10 %. A total of 5 (out of 84) individual samples were rejected due to inconsistent results

(e.g. the amount of radioiodinated products was ± 2.5s from the average yield of the sample set).

Highest radiochemical yields were obtained in 120 °C. However, it was decided to set 95 °C as the reaction temperature for the rest of the method development, since the sample preparation protocol relied on the use of Eppendorf tubes, which have a heat tolerance up to 100 °C. Due to 2-propanol's relatively low boiling point and the reaction yield's dependence on reaction temperature, cyclohexanol was assessed to be the most suitable solvent from the solvents tested. However, it must be noted that cyclohexanol's high viscosity poses a practical issue in sample preparation, and additional care must be taken to assure all reagents are mixed and dissolved in the reaction mixture. Following the decision to use cyclohexanol as the solvent of choice, 3.0 µmol of carrier was selected as the carrier amount, since the highest radiochemical yields in cyclohexanol were obtained with 3.0 µmol.

Due to iodine's volatility, the suspected evaporation of radioiodine during reaction was tested twice during the optimization phase, first under the initial conditions and finally under the optimized conditions, by taking a 200 µL aliquot of the reaction mixture before and after the reaction and measuring the difference in activity between the samples by gamma counting. No significant change in radioactivity was observed under either conditions, and it was concluded that no significant loss of radioactivity occurred

5.2 Comparison to electrophilic substitution

Comparison of the Dowex®-mediated iodination reaction was carried out in the optimized reaction conditions using 4-phenyl-1-butyne as the precursor: that is, 3.0 µmol of I^- carrier; 95 °C reaction temperature; cyclohexanol as solvent; and with Dowex® HCl activation and excess water evaporated. The test was conducted by preparing the samples in triplicate and with differing reaction facilitating agents: Dowex®, Chloramine-T, and Iodogen™. Quantitative results are based on HPLC analysis of the samples, and a summary of the comparison results can be found in Attachment 1. Radio-HPLC results of method optimization. The results are illustrated in Figure 30.

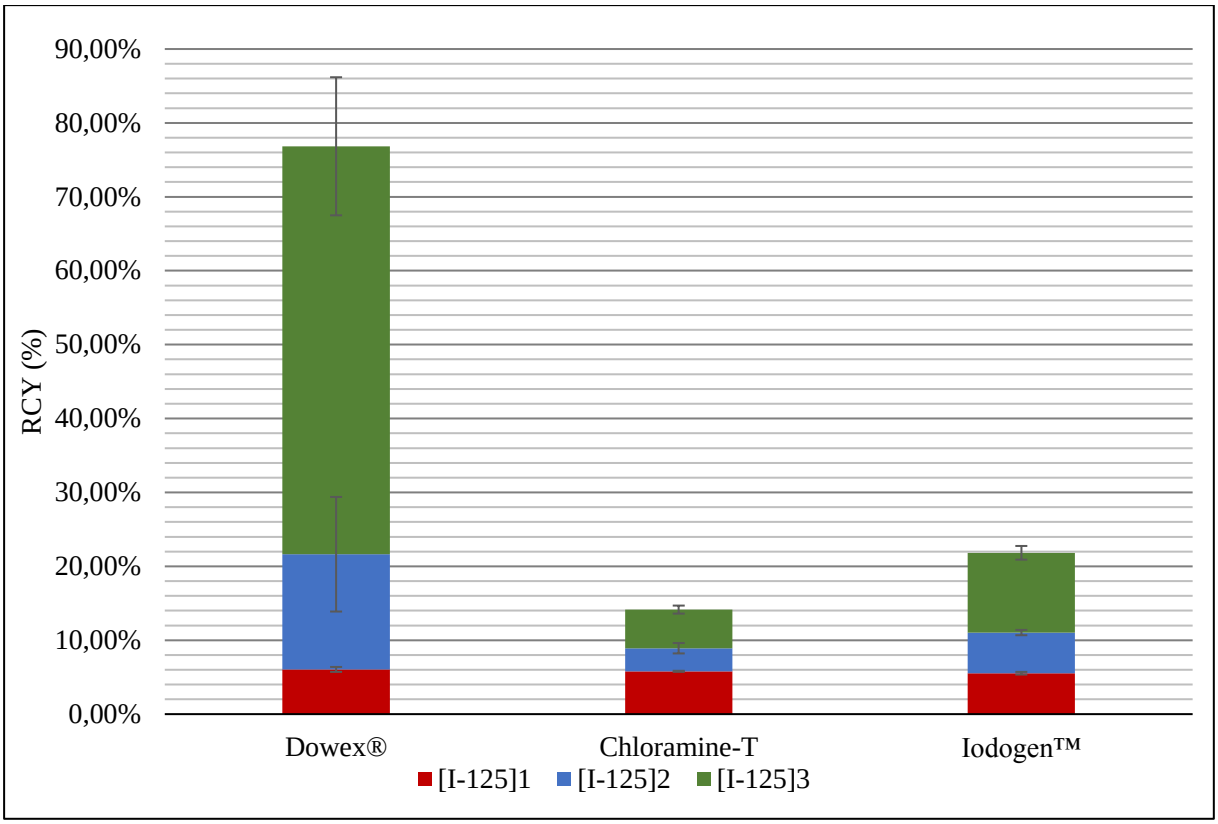

Figure 30. Comparison of optimized Dowex®-mediated radioiodination of 4-phenyl-1-butyne to electrophilic radioiodinations of 4-phenyl-1-butyne. The highest yields of radioiodinated products were achieved by using Dowex® to facilitate the reaction: RCY of the main product, [^{125}I]**3**, was 55.2 ±9.3 % and total RCY 76.8 ±1.6 %.

Under the test conditions, reactions with Dowex® yielded in a significantly higher radiochemical yield of [^{125}I]**3** than reactions with electrophilic reagents. [^{125}I]**3** dominated in the Dowex®-mediated reaction product distribution, whereas samples prepared with electrophilic reagents displayed a more even distribution of reaction products. RCYs of [^{125}I]**1** and [^{125}I]**2** were quite similar regardless of reaction facilitating used, from 1.9 to 6.2 %, implying that the choice of the reaction facilitating agent mostly affects the formation of [^{125}I]**3**. Selected radio-HPLC chromatograms and the associated peak data of samples prepared with Dowex®, Chloramine-T, and Iodogen™ are presented in Figure 31, Figure 32, Figure 33, respectively

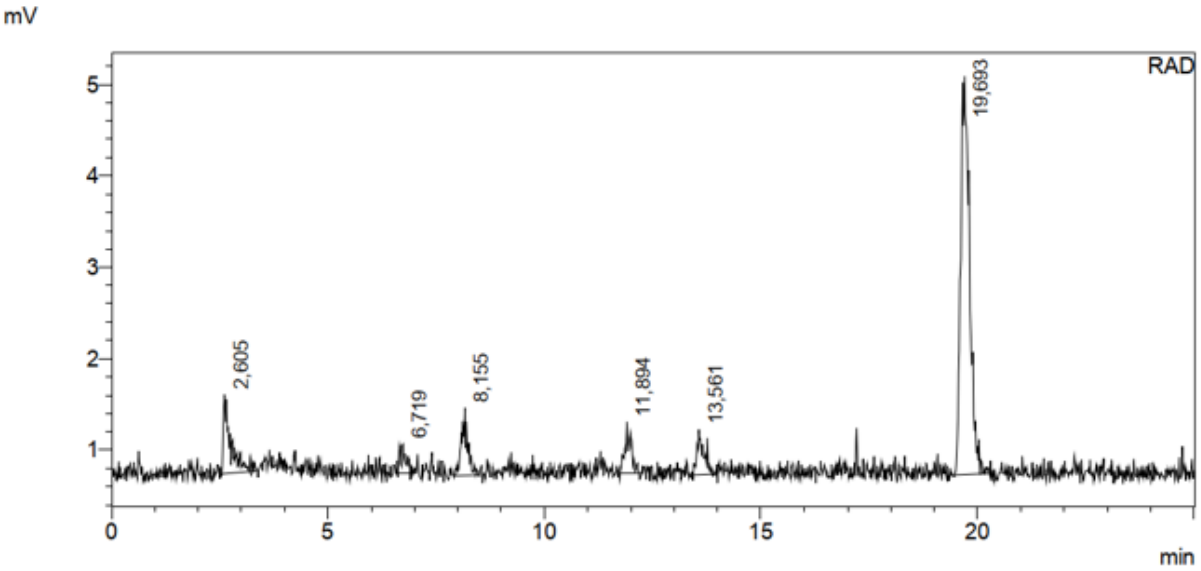

RAD

Peak#	Ret. Time	Area	Height	Conc.
1	2,605	10506	863	11,207
2	6,719	3069	319	3,274
3	8,155	7157	741	7,634
4	11,894	5124	561	5,466
5	13,561	5154	498	5,498
6	19,693	62737	4357	66,921
Total		93748	7338	

Figure 31. A radio-HPLC chromatogram and associated peak data of a sample prepared with HCl-activated Dowex® in cyclohexanol, in 95 °C, with 3.0 µmol of I^- carrier and 60 min reaction time. [^{125}I]**1**, [^{125}I]**2** and [^{125}I]**3** peaks are found at 11.894 min, 13.561 min and 19.693 min, respectively, [^{125}I]**3** being the main product formed at RCY of 66.921 %. Free $^{125}I^-$ peak is found at 2.605 min. Small peaks associated with unidentified radioiodination side products can be found at 6.719 min and 8.023 min; these side products appeared inconsistently in the samples, typically in low yields, and were thus left unidentified.

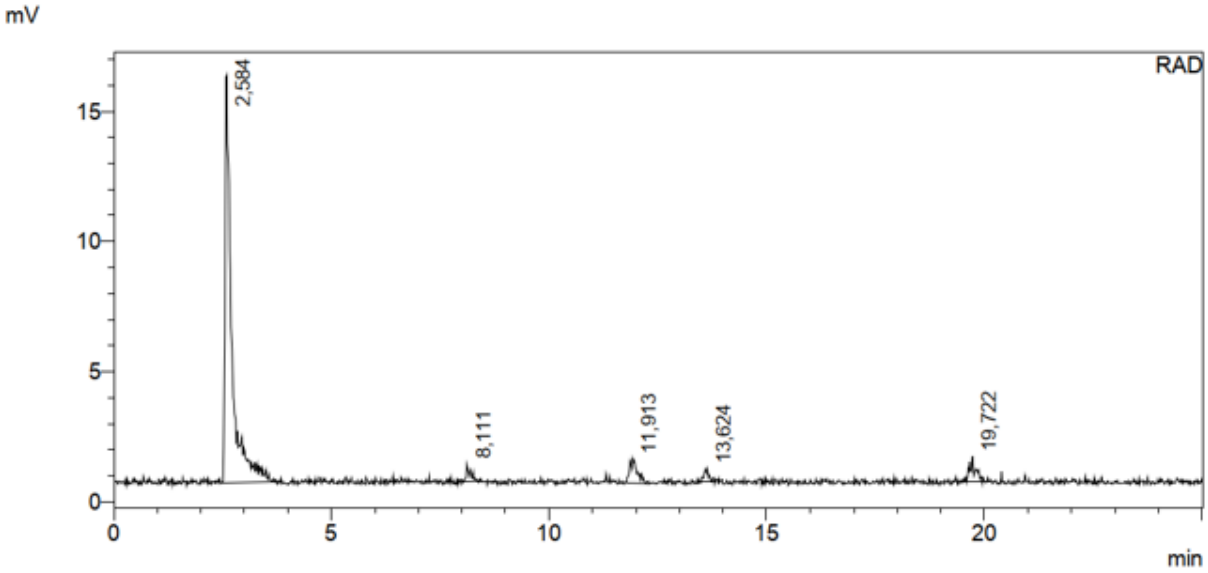

RAD

Peak#	Ret. Time	Area	Height	Conc.
1	2,584	168010	15646	85,755
2	8,111	4088	677	2,086
3	11,913	11370	931	5,803
4	13,624	3902	489	1,991
5	19,722	8548	931	4,363
Total		195917	18674	

Figure 32. A radio-HPLC chromatogram and associated peak data of a sample prepared with Chloramine-T in cyclohexanol, in 95 °C, with 3.0 µmol of I^- carrier and 60 min reaction time. [^{125}I]**1**, [^{125}I]**2** and [^{125}I]**3** peaks are found at 11.913 min, 13.624 min and 19.722 min, respectively. [^{125}I]**3** was formed in relatively small amounts in this sample (4.363 %), compared to those prepared with HCl-activated Dowex®, [^{125}I]**1** being the main product at RCY of 5.803 %. Free $^{125}I^-$ peak is found at 2.584 min. A peak associated with an unidentified radioiodination side product can be found at 8.111 min; this side product appeared inconsistently in the samples, typically in low yields, and was thus left unidentified.

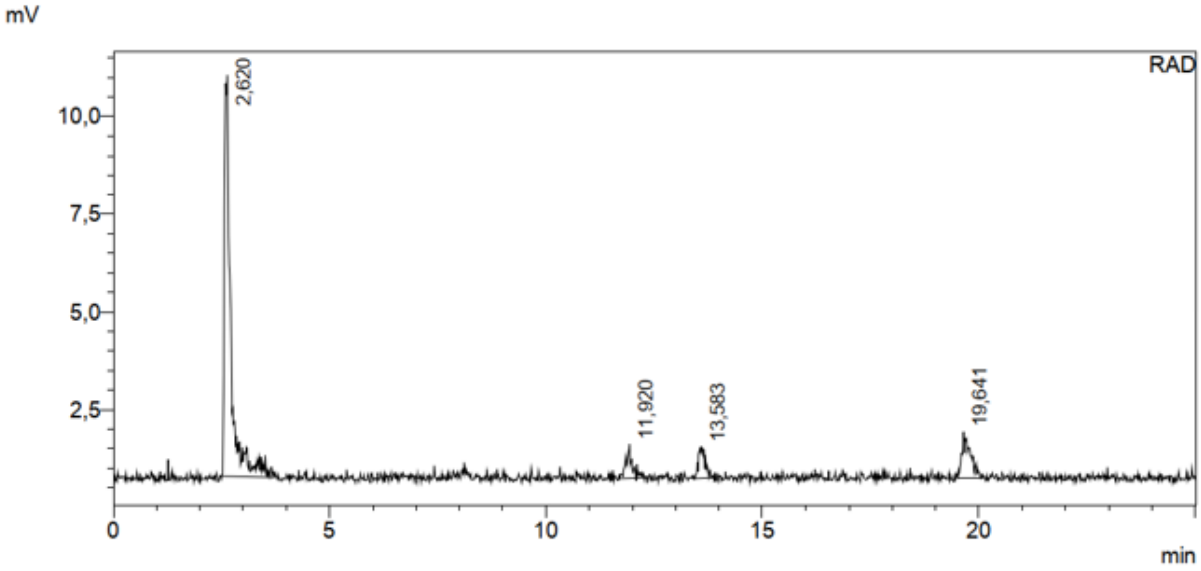

RAD

Peak#	Ret. Time	Area	Height	Conc.
1	2,620	107986	10274	77,284
2	11,920	8050	859	5,761
3	13,583	8659	791	6,197
4	19,641	15033	1169	10,759
Total		139727	13093	

Figure 33. A radio-HPLC chromatogram and associated peak data of a sample prepared with Iodogen™ in cyclohexanol, in 95 °C, with 3.0 µmol of I^- carrier and 60 min reaction time. [^{125}I]**1**, [^{125}I]**2** and [^{125}I]**3** peaks are found at 11.920 min, 13.583 min and 19.641 min, respectively. Amount of [^{125}I]**3** formed in this sample (10.759 %) was slightly higher than in those prepared with Chloramine-T, but significantly lower than in the samples prepared with HCl-activated Dowex®. Free $^{125}I^-$ peak is found at 2.620 min.

5.3 Radioiodination of sugar analogues

The optimized radioiodination protocol was tested on sugar analogues. The test was carried out by preparing triplicate samples from two different acetylated sugar analogues **4** and **5** as precursors, utilizing the optimized conditions described before. The samples were analyzed with the same HPLC method developed for the optimization phase. Radiochemical yields and retention times of the main products of Dowex®-mediated sugar analogue radioiodination are presented in Figure 34.

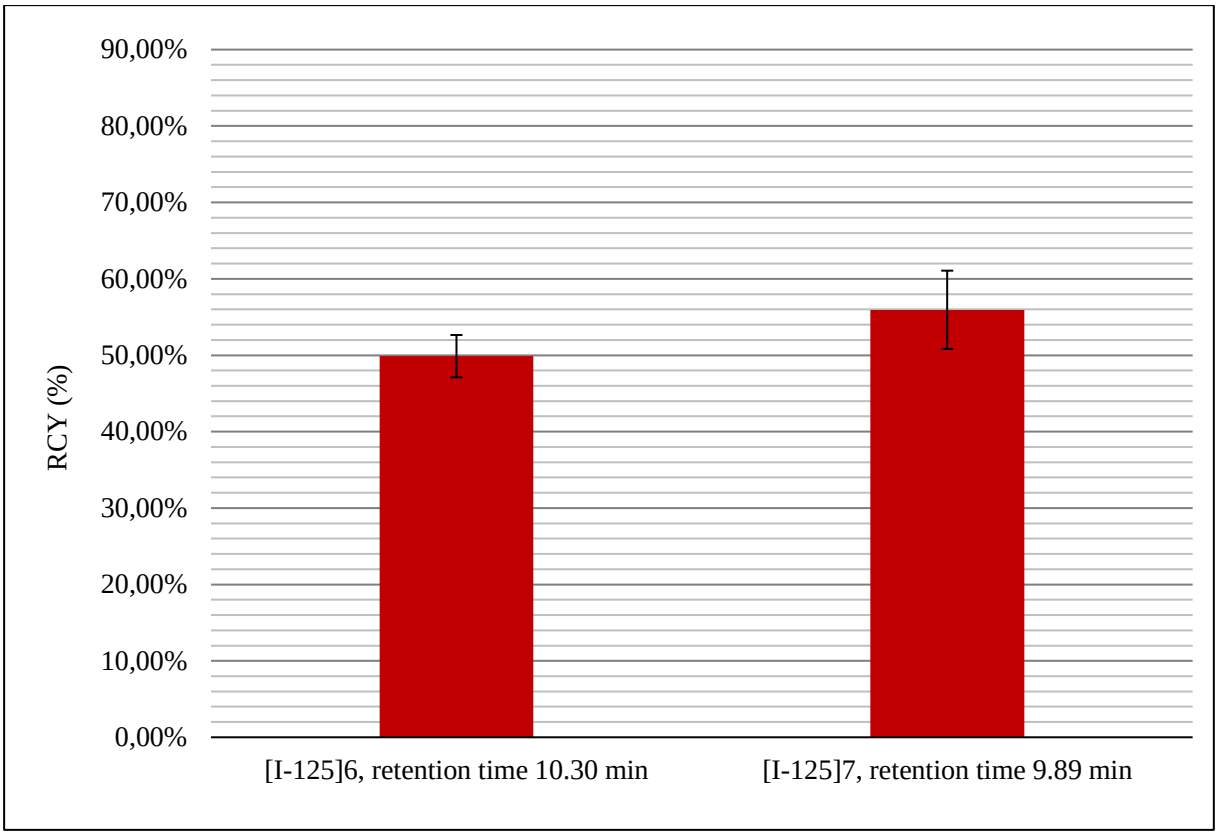

Figure 34. Radiochemical yields and retention times of the main products of Dowex®-mediated sugar analogue radioiodination. RCY of the main product was slightly higher in samples prepared from **5**: using **4** as the precursor resulted in [^{125}I]**6** with RCY of 49.9 ±2.8 %, whereas using **5** as the precursor resulted in [^{125}I]**7** with RCY of 56.0 ±5.1 %.

Tests with each precursor yielded one main product with a yield of 45 – 62 % and a consistent retention time, and 2 – 5 side products with low and inconsistent yields. Tests with **5** resulted in a slightly higher average yield: however, the difference is not statistically significant. Yields with both precursors were consistent, and the radioiodination methods appears to retain its repeatability when applied to the sugar analogues in question.

5.4 Characterization

To characterize the main product obtained in radioiodination of sugar analogues, samples without radioactive iodine were prepared from both aforementioned precursors, using the optimized radioiodination protocol upscaled in order to obtain a sufficient amount of main product for characterization. The product was separated from the reaction mixture by HPLC fractioning, and the eluent was evaporated by first removing the bulk of the eluent by rotary

evaporation and then lyophilizing the sample to remove as much of the residual eluent as possible, resulting in purified product obtained in a yield of ~1 mg. The samples were dissolved in deuterated acetonitrile, CD_3CN, and their ^{1}H-NMR spectra measured with a 400 MHz NMR spectrometer, along with reference samples prepared from the non-iodinated precursors. Since the results from the optimization phase strongly suggested a di-iodinated product, the reaction with sugar analogues was hypothesized to behave similarly and lead to a di-iodinated product. In **5** there are two propargyl moieties in which the iodination reaction may occur: the possibility of regioselectivity between the moieties was acknowledged, but no hypothesis was made concerning the preferred reaction position.

The characteristic differences in the NMR spectra of **4** and its main reaction product **6** are most apparent in the chemical shifts and splitting patterns of protons 6a, 6b and 7. In **4**'s spectrum protons 6a and 6b display the 16.0 Hz chemical shift of originating from the geminal ^{2}J-coupling between the protons, and the 2.4 Hz shift from the propargylic long-range ^{4}J-coupling with proton 7. The doublet of doublets splitting pattern further confirms this coupling scheme. In **4**'s spectrum, proton 7's chemical shift is assigned as 2.71 ppm, and it's observed splitting pattern is a triplet. The coupling constant 2.4 Hz indicates propargylic ^{4}J-coupling with protons 6a and 6b. In **6**'s spectrum, proton 7's chemical shift has moved to 7.32 ppm and it's observed splitting pattern has changed into a singlet. However, protons 6a and 6b display, in addition to the ^{2}J-coupling constant 13.2 Hz, a coupling constant of 0.6 Hz, most likely indicating an allylic ^{4}J-coupling with proton 7: thus, proton 7's splitting pattern would be actually a triplet, although, likely due to limited resolution, the small coupling constant leads to the observed splitting pattern to be a singlet. From precursor to product spectrum, the chemical shift of 6b displays an increase of 0.17 Hz, and the chemical shift of proton 1 has decreased by 0.20 Hz, but these changes were not considered relevant for characterization. Four singlets with an integral corresponding to that of 3 protons can be observed in the 1.87 – 2.00 ppm range in both spectrums, indicating that the protecting acetyl groups remained intact during and after reaction. In summary, the NMR interpretation supports the hypothesis of a di-iodinated product **6** with no other observable structural changes. NMR interpretations of **4** and its main reaction product are illustrated in Figure 35. Details of NMR spectra of **4** and **6**, demonstrating the characteristic structural changes resulting from the iodination reaction, are illustrated in Figure 36 and Figure 37.

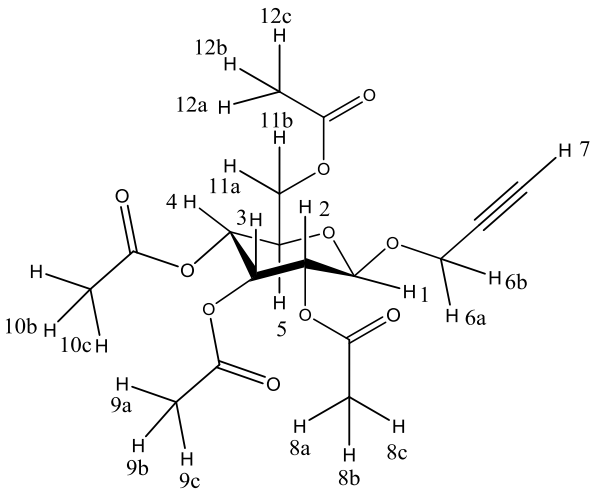

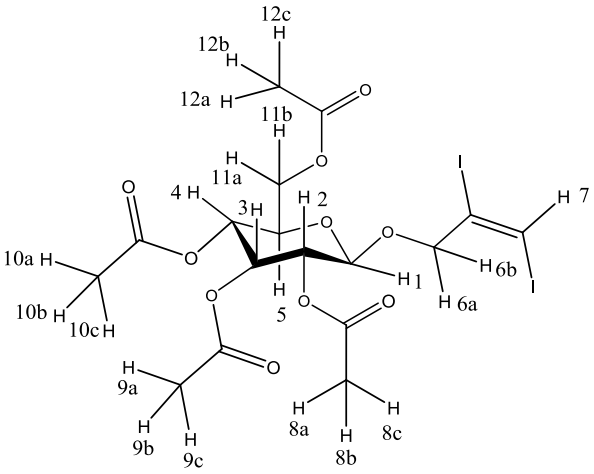

^{1}H NMR (400 MHz, Acetonitrile-d3)	1H NMR (400 MHz, Acetonitrile-d3)
5.18 (t, $^{3}J_{HH}$ = 9.6 Hz, 1H, H3),	7.32 (d, $^{4}J_{HH}$ = 0.6 Hz, 1H, H7),
4.95 (t, $^{3}J_{HH}$ = 9.8 Hz, 1H, H4),	5.19 (t, $^{3}J_{HH}$ = 9.6 Hz, 1H, H3),
4.82 (dd, $^{3}J_{HH}$ = 9.7, 8.0 Hz, 1H, H2),	4.97 (t, $^{3}J_{HH}$ = 9.7 Hz, 1H, H4),
4.72 (d, $^{3}J_{HH}$ = 8.0 Hz, 1H, H1),	4.87 (dd, $^{3}J_{HH}$ = 9.8, 8.1 Hz, 1H, H2),
4.29 (dd, $^{1}J_{HH}$ = 16.0, $^{4}J_{HH}$ = 2.4 Hz, 1H, H6b),	4.52 (d, $^{3}J_{HH}$ = 8.1 Hz, 1H, H1),
4.23 (dd, $^{1}J_{HH}$ = 16.0, $^{4}J_{HH}$ = 2.4 Hz, 1H, H6a),	4.46 (dd, $^{1}J_{HH}$ = 13.2, $^{4}J_{HH}$ = 0.6 Hz, 1H, H6b),
4.16 (dd, $^{1}J_{HH}$ = 12.3, $^{3}J_{HH}$ = 5.0 Hz, 1H, H11b),	4.23 (dd, $^{1}J_{HH}$ = 13.1, $^{4}J_{HH}$ = 0.6 Hz, 1H, H6a),
3.99 (dd, $^{1}J_{HH}$ = 12.4, $^{3}J_{HH}$ = 2.5 Hz, 1H, H11a),	4.18 (dd, $^{1}J_{HH}$ = 12.3, $^{3}J_{HH}$ = 5.1 Hz, 1H, H11b),
3.76 (ddd, $^{3}J_{HH}$ = 10.0, 4.9, 2.5 Hz, 1H, H5),	4.02 (dd, $^{1}J_{HH}$ = 12.1, $^{3}J_{HH}$ = 2.4 Hz, 1H, H11a),
2.71 (t, $^{4}J_{HH}$ = 2.4 Hz, 1H, H7),	3.76 (ddd, $^{3}J_{HH}$ = 10.0, 5.1, 2.5 Hz, 1H, H5),
1.94 (s, 3H, H12a,b,c),	1.97 (s, 3H, H12a,b,c),
1.93 (s, 3H, H8a,b,c),	1.94 (s, 3H, H8a,b,c),
1.90 (s, 3H, H10a,b,c),	1.89 (s, 3H, H10a,b,c),
1.87 (s, 3H, H9a,b,c).	1.88 (s, 3H, H9a,b,c).

Figure 35. NMR interpretations of 4 and its main reaction product, 1-((E)-2,3-diiodo-prop-2-en-1-yloxy)-2,3,4,6-tetra-O-acetyl-D-glucose (6). The structural differences between the precursor and the product can be observed in the chemical shifts of hydrogens 6b and 7, indicating the addition of iodine to the triple bond.

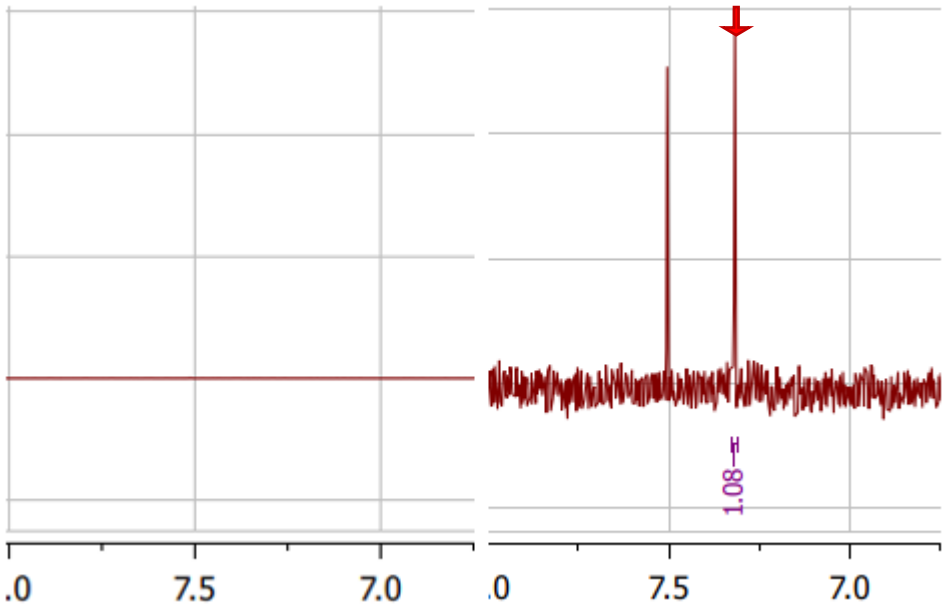

Figure 36. Details of NMR spectra of **4** (left) and **6** (right). The peak at 7.32 ppm (H7), marked with the red arrow in the right-side spectrum and notably absent in the left-side spectrum, indicates the di-iodination of the triple bond that results in the shifting of the terminal hydrogen peak from 2.70 to 7.31 ppm. The unmarked peak in the right-side spectrum results from solvent impurities.

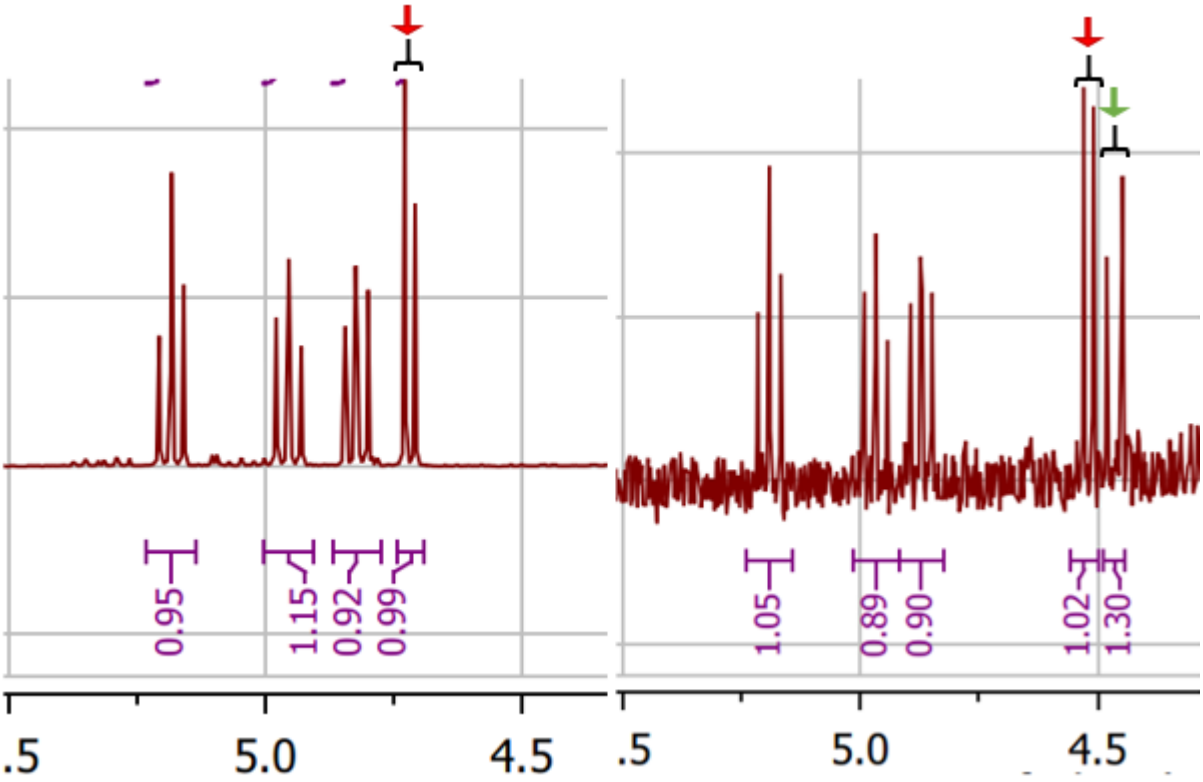

Figure 37. Details of NMR spectra of **4** (left) and 6 (right). The doublet at 4.72 (H1) ppm, marked with the red arrow in the left-side spectrum, has shifted to 4.52 in the right-side spectrum following the structural changes caused by the di-iodination of the triple bond. The doublet of doublets (H6b; appearing as a doublet in the figure due to scale) at 4.46 ppm and marked with a green arrow in the right side spectrum, has shifted from 4.29 ppm due to the structural changes caused by the di-iodination of the triple bond. The three unmarked multiplets appearing in both spectrums with unchanged chemical shifts are associated with, from left to right, H3, H4 and H2.

In the NMR spectrum of **5**, the propargylic terminal protons 7 and 10 can be observed as triplets with a coupling constant of 2.4 Hz and chemical shifts of 2.70 and 2.67 ppm, respectively. Protons 6a and 6b display a propargylic ^{4}J-coupling constant of 2.4 Hz in addition to the geminal ^{2}J-coupling constant of 16.0 Hz, and protons 9a and 9b display a propargylic ^{4}J-coupling constant of 2.4 Hz. In **7**'s NMR spectrum, the triplet at 2.70 ppm has disappeared and replaced by a singlet at 7.31 ppm, while the coupling constants of protons 6a and 6b have changed from 16.0 and 2.4 Hz to 13.3 and 0.7 Hz, indicating a similar structural change as with **4** and its product. However, the triplet at 2.70 ppm is still present in product **7**'s spectrum, and the chemical shifts of protons 9a, 9b and 3 remain virtually unchanged from precursor to

product spectrum, indicating regioselectivity towards one propargyl moiety over the other. A similar -0.20 Hz change in the chemical shift of proton 1 is observed as with **4** and its product: a comparable change would assumedly be observed in the chemical shift of proton 3 if the radioiodination occurred in both propargyl moieties. However, no such change is observed, and since proton 3:s coupling constants matches closely to those of protons 4 and 2, it can be deduced that no significant structural changes occur in this part of the molecule, and the hypothesis of regioselectivity is substantiated further. It should be noted that the expected splitting pattern of proton 3 in both spectrums is a doublet of doublets with ^{3}J-coupling constants of 10.1 and 9.5 Hz: however, the observed splitting pattern is a triplet, likely due to limited resolution. As with **4** and its product, **6**, the protecting acetyl groups remain intact, according to the three singlets with 3-hydrogen integrals at 1.94 – 2.00 ppm range in the precursor spectrum and the singlet with a 9-hydrogen integral at 1.93 – 1.99 ppm range in the product spectrum. In summary, the NMR interpretation supports the hypothesis of a di-iodinated product with no other observable structural changes. In addition, the NMR data suggests regioselectivity towards the propargyl moiety in 1-position. NMR interpretations of **5** and its main reaction product **7** are illustrated in Figure 38. Details of NMR spectra of **5** and **7**, demonstrating the characteristic structural changes resulting from the iodination reaction, are illustrated in Figure 39 and Figure 40.

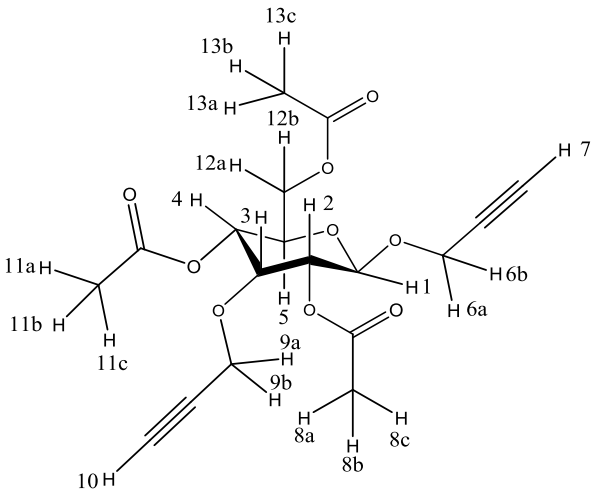

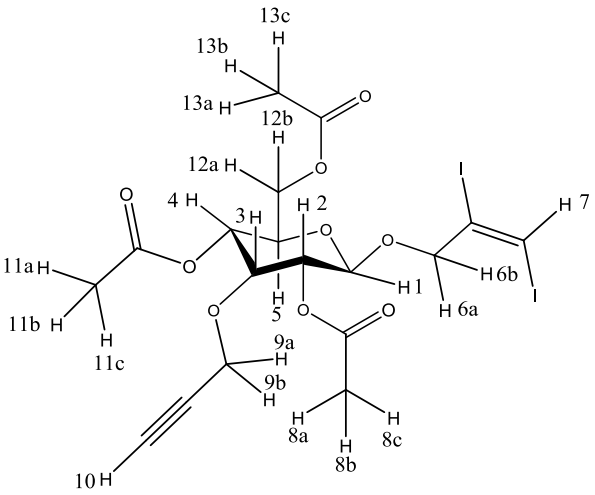

^{1}H NMR (400 MHz, Acetonitrile-d3) 4.85 (dd, $^{3}J_{HH}$ = 10.1, 9.3 Hz, 1H, H-4), 4.72 (dd, $^{3}J_{HH}$ = 9.5, 8.0 Hz, 1H, H-2), 4.60 (d, $^{3}J_{HH}$ = 8.1 Hz, 1H, H-1), 4.27 (dd, $^{1}J_{HH}$ = 16.0, $^{4}J_{HH}$ = 2.4 Hz, 1H, H-6b), 4.21 (dd, $^{1}J_{HH}$ = 16.0, $^{4}J_{HH}$ = 2.4 Hz, 1H, H-6a), 4.16 (d, $^{4}J_{HH}$ = 2.4 Hz, 2H, H-9a,b), 4.10 (dd, $^{1}J_{HH}$ = 12.3, $^{3}J_{HH}$ = 5.2 Hz, 1H, H-12b), 3.96 (dd, $^{1}J_{HH}$ = 12.3, $^{3}J_{HH}$ = 2.6 Hz, 1H, H-12a), 3.72 (t, $^{3}J_{HH}$ = 9.4 Hz, 1H, H-3), 3.64 (ddd, $^{3}J_{HH}$ = 10.1, 5.2, 2.5 Hz, 1H, H-5), 2.70 (t, $^{4}J_{HH}$ = 2.4 Hz, 1H, H-7), 2.67 (t, $^{4}J_{HH}$ = 2.4 Hz, 1H, H-10), 2.00 (s, 3H, H-13a,b,c), 1.99 (s, 3H-8a,b,c), 1.94 (s, 3H, H-11a,b,c)	^{1}H NMR (400 MHz, Acetonitrile-d3) 7.31 (s, 1H, H-7), 4.87 (dd, $^{3}J_{HH}$ = 10.1, 9.3 Hz, 1H, H-4), 4.77 (dd, $^{3}J_{HH}$ = 9.5, 8.1 Hz, 1H, H-2), 4.44 (dd, $^{1}J_{HH}$ = 13.2, $^{4}J_{HH}$ = 0.7 Hz, 1H, H-6b), 4.40 (d, $^{1}J_{HH}$ = = 8.1 Hz, 1H, H-1), 4.21 (dd, $^{1}J_{HH}$ = 13.2, $^{4}J_{HH}$ = 0.7 Hz, 1H, H-6a), 4.16 (d, $^{4}J_{HH}$ = 2.4 Hz, 2H, H-9a,b), 4.13 (dd, $^{1}J_{HH}$ = 12.3, $^{1}J_{HH}$ = 5.3 Hz, 1H, H-12b), 3.98 (dd, $^{1}J_{HH}$ = 12.2, $^{1}J_{HH}$ = 2.5 Hz, 1H, H-12a), 3.73 (t, $^{1}J_{HH}$ = 9.4 Hz, 1H-3), 3.64 (ddd, $^{1}J_{HH}$ = 10.0, 5.3, 2.5 Hz, 1H, H-5), 2.67 (t, $^{4}J_{HH}$ = 2.4 Hz, 1H, H-10), 1.99 – 1.93 (m, 9H, H-8a,b,c-11a,b,c-13a,b,c)

Figure 38. NMR interpretations of **5** and its main reaction product, (1-((E)-2,3-diiodo-prop-2-en-1-yloxy)-3-(prop-2-yn-1-yloxy)-2,4,6-tri-O-acetyl-D-glucose (**7**). The structural differences between the precursor and the product can be observed in the chemical shifts of hydrogens 6b and 7, indicating the di-iodination of the triple bonf. The chemical shifts of hydrogens 9a, 9b and 10 remain unchanged from precursor to product spectra, indicating that no iodination takes place in the 3-(prop-2-yn-1-yloxy) moiety.

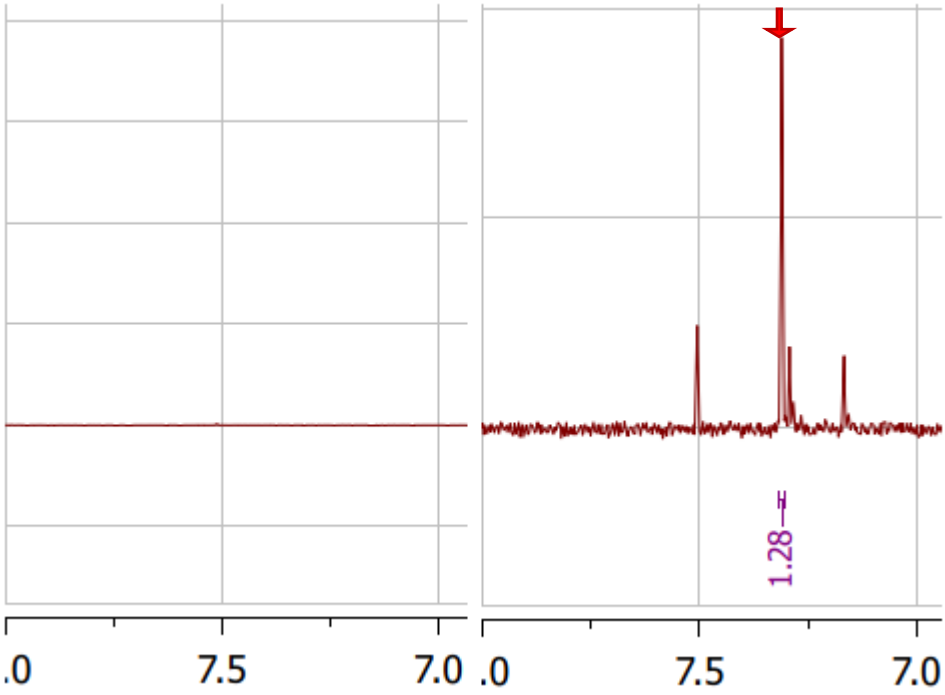

Figure 39. Details of NMR spectra of **5** (left) and **7** (right). The peak at 7.31 (H7) ppm, marked with the red arrow in the right-side spectrum and notably absent in the left-side spectrum, indicates the di-iodination of the triple bond that results in the shifting of the terminal hydrogen peak from 2.70 to 7.31 ppm. The unmarked peaks in the right-side spectrum result from solvent impurities and other contaminants.

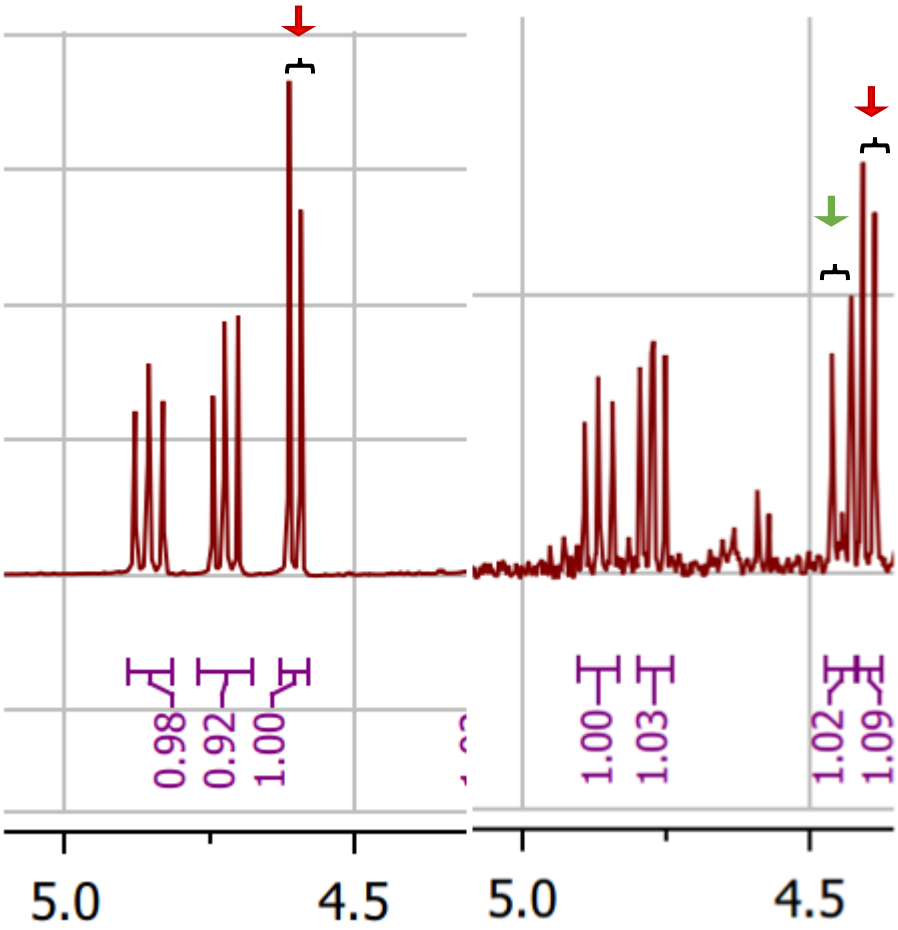

Figure 40. Details of NMR spectra of **5** (left) and **7** (right). The doublet at 4.62 (H1) ppm, marked with the red arrow in the left-side spectrum, has shifted to 4.40 in the right-side spectrum following the structural changes caused by the di-iodination of the triple bond. The doublet of doublets (H6b; appearing as a doublet in the figure due to scale) at 4.44 ppm and marked with a green arrow in the right side spectrum, has shifted from 4.27 ppm due to the structural changes caused by the di-iodination of the triple bond. The two unmarked multiplets appearing in both spectrums with virtually unchanged chemical shifts are associated with, from left to right, H4 and H2.

6. Conclusions

The experimental goal of this study was to optimize a radioiodination method that could be used to radiolabel sugar analogues for the purpose of studying plant carbohydrate metabolism by multimodality imaging. The radioiodination method described in this study is reasonably quick, one-pot reaction that leads to a selectively radioiodinated main product in a reasonably high yield, and it is likely that the method can be applied without significant modifications to radioiodinations of other, similar sugar analogues to the ones used in this study. Iodine has a variety of radioisotopes that suit many different imaging purposes and modalities, and, if the *in vivo* stability and behavior of compounds labeled with the method described in this study proves to be viable, radioiodination of sugar alkynyl derivatives could prove to be an effective and versatile method to produce suitable molecular tracers for plant carbohydrate metabolism studies.

Optimization of the radioiodination method was concluded with satisfactory results, and the optimal carrier amount and reaction temperature for each tested solvent was fairly unambiguous. Selecting the optimal solvent, however, was not as straightforward. In 70 and 95 °C, the highest RCY of main product [^{125}I]**3** and total yield of radioiodinated products were achieved with 2-propanol, but in 120 °C 2-propanol evaporated completely. In 95 °C slight evaporation of 2-propanol could be observed, but the use of Safe-Lock Eppendorf tubes prevented further evaporation. In 120 °C, RCY of [^{125}I]**3** surpassing those of 2-propanol in 95 °C was achieved in cyclohexanol: however, no further tests were conducted in this temperature due to the safety risk the Eppendorf tubes' heat tolerance (up to 100 °C) posed. The option to increase reaction temperature further was evaluated to be more crucial than the radiochemical yield under prevailing conditions: thus, cyclohexanol was selected as the solvent due to its significantly higher boiling point compared to 2-propanol. Initially, in 95 °C and with 3.0 µmol of carrier, total yields of radiochemical products differed notably between samples prepared in cyclohexanol and 2-propanol (40.60 % and 57.30 %, respectively; not statistically significant, however). Further experiments with cyclohexanol in 95 °C and with 3.0 µmol of carrier resulted in a statistically significant increase in total yield of radiochemical products, up to 77 %. The reason for the increase was not studied, but since the increase manifested consistently throughout the sample sets, it was concluded that cyclohexanol is the most optimal solvent of the ones tested.

Assuming a (plausible) 65 % RCY of [^{125}I]**3** has been achieved with 0.5 MBq of ^{125}I by utilizing the Dowex®-mediated reaction studied in this work, and that 3 µmol of carrier I^- reacts producing non-radioactive **3** in the same proportion, the molar activity of [^{125}I]**3** produced in this study is 0.1667 MBq/µmol. This molar activity is very low, and not suitable for *in vivo* purposes. However, since two iodine atoms are incorporated into the molecule when **3** is produced, the theoretical, carrier-free maximum molar activity of [^{125}I]**3** is 162,7 GBq/µmol, which is far more viable for *in vivo* purposes, since high molar activity radiotracers are typically to be in the order of 10^{11} Bq/µmol.[93] ^{125}I is, though, unsuitable for *in vivo* studies due to its decay properties (and achieving the theoretical maximum molar activity is unlikely anyway), ^{123}I and ^{124}I being more suitable radioisotopes of iodine for *in vivo* radiotracer. Theoretical, carrier-free maximum molar activities of [^{123}I]**3** and [^{124}I]**3** are 17.57 TBq/µmol and 2.312 TBq/µmol, respectively. It is unlikely that these theoretical maxima can be actually achieved, but it is, however, plausible, that radiotracers of sufficient molar activity may be produced with the radioiodination method described in this study.

The comparison to electrophilic substitution reactions indicated that, under the optimized conditions, the Dowex®-mediated reaction leads to superior yields compared to chloramine- and Iodogen-mediated reactions. However, the substrate and optimized reaction conditions differ significantly from those in which chloramine or Iodogen are typically applied. Chloramine T is typically used in radioiodinations of aromatic compounds[94]; peptides and proteins have been labelled with Chloramine, but the risk of oxidative damage to the substrate renders this an unfavourable method[95,96]. Chloramines have been applied in iodinations of terminal alkynes, and reaction yields up to 93 % were obtained with 4-phenyl-1-butyne as the substrate and Chloramine B as the oxidant, with significantly differing reaction conditions compared to those in this study: reaction was executed in room temperature, reaction time was two hours, the solvent used was ACN, and an excess of KI, compared to the substrate, was used as the source of I^-.[97] It seems unlikely, though, that this approach would work in radioiodinations without other adaptations than the addition of radioactive I^-, since an excess of non-radioactive I^- carrier will likely compete with radioactive I^- during the reaction, leading to low radiochemical yield and molar activity. Iodogen is a mild oxidizing agent that is used in iodinations of proteins, peptides and other biomolecules that are sensitive to stronger oxidants[94,98,99]. It is typically used in aqueous buffer solutions, and the reactions are carried out in room temperature during relatively short (2 – 30 min) reaction times.[94,98] As with Chloramine

T, the typical conditions for Iodogen reactions differ significantly from those used in this study, but the exact reason for the low yield remains elusive. However, in the optimized reaction conditions of this study it was remarkably obvious that the Dowex®-mediated reaction leads to the highest yields.

The optimized radioiodination method was tested successfully on the sugar analogues. Radiochemical yields of the main products **6** and **7** were satisfactory (45 – 62 %), and it is likely that the yield may be further improved. The characterization confirmed that the reaction is regioselective towards the di-iodinated main product, as predicted by the results of the optimization phase; in addition, when using the glucose derivative **5** with two propargyl groups as possible reaction sites, the characterization indicated regioselectivity towards the propargyl moiety in 1-position over the moiety in 3-position, which could not be hypothesized from the optimization results. In addition to the main product peak, multiple radio peaks with shorter retention time were observed: these are suspected to be radioiodinated side products. However, these peaks manifested inconsistently throughout the sample batches and in such low yields (<10 %), that characterization of the side products was not considered relevant, or even feasible in the tested sample volumes. The shorter retention time compared to the main product indicates that the side products are structurally similar to the main product, except that one or more of their protective groups has disconnected during labeling. Disconnection of the protective groups was expected to occur during labeling: however, NMR characterization of the main products indicates that in the main product the protective groups remain intact.

The exact reaction mechanism of the iodination method is not yet known, and the means to improve radiochemical yield likely depend on the mechanism. By increasing the reaction temperature, a higher radiochemical yield could possibly be achieved. Increasing the reaction temperature requires more heat-resistant sample vessels than used in this study, and in elevated temperatures iodine may escape the solution; however, the latter effect was not be observed in the temperatures used this study. Using a catalyst could possibly lead to improved radiochemical yield, in addition to providing more control over product selectivity[100–102]; however, using a catalyst may not be directly adaptable to the one-pot method used in this study, complicating the procedure, and the use of a heavy metal catalyst violates the green chemistry principle upon which the iodination method presented in this study is originally built[90,91]. In the tested scale the required amount of carrier NaI for one sample was of such a small mass that it

could not be accurately weighed: therefore, NaI was added as an aqueous solution, in addition to the ^{125}I that was necessary to add in a solution. Removal of excess water had an observable (but statistically insignificant) effect on radiochemical yield, and by scaling up the synthesis the amount of water in a sample may be further reduced to improve yield.

References

1 J. Tian, *Molecular Imaging*, Springer Berlin Heidelberg, Berlin, Heidelberg, 2013.

2 R. Weissleder and M. J. Pittet, Imaging in the era of molecular oncology, *Nature*, 2008, **452**, 580–589.

3 S. Vallabhajosula, *Molecular Imaging*, Springer Berlin Heidelberg, Berlin, Heidelberg, 2009.

4 D. A. Mankoff, A definition of molecular imaging., *J. Nucl. Med.*, 2007, **48**, 20–22.

5 S. Y. Lee, S. I. Jeon, S. Jung, I. J. Chung and C. H. Ahn, Targeted multimodal imaging modalities, *Adv. Drug Deliv. Rev.*, 2014, **76**, 60–78.

6 E. N. Landis and D. T. Keane, X-ray microtomography, *Mater. Charact.*, 2010, **61**, 1305–1316.

7 J. Lehto and X. Hou, *Chemistry and Analysis of Radionuclides*, Wiley-VCH Verlag GmbH & Co. KGaA, Weinheim, Germany, 2010.

8 B. M. Bavelaar, B. Q. Lee, M. R. Gill, N. Falzone and K. A. Vallis, Subcellular targeting of theranostic radionuclides, *Front. Pharmacol.*, 2018, **9**, 1–17.

9 N. Suzui, K. Tanoi, J. Furukawa and N. Kawachi, Recent Advances in Radioisotope Imaging Technology for Plant Science Research in Japan, *Quantum Beam Sci.*, 2019, **3**, 18.

10 A. Vértes, S. Nagy, Z. Klencsár, R. G. Lovas and F. Rösch, *Handbook of Nuclear Chemistry*, Springer US, Boston, MA, 2011.

11 G. F. Knoll, *Radiation Detection and Measurement*, Wiley, New York, 4th edn., 2010.

12 P. G. Camici and O. E. Rimoldi, The clinical value of myocardial blood flow measurement, *J. Nucl. Med.*, 2009, **50**, 1076–1087.

13 T. L. Roß and S. M. Ametamey, *Basic Sciences of Nuclear Medicine*, Springer Berlin Heidelberg, Berlin, Heidelberg, 2011.

14 M. M. Khalil, J. L. Tremoleda, T. B. Bayomy and W. Gsell, Molecular SPECT Imaging: An Overview, *Int. J. Mol. Imaging*, 2011, **2011**, 1–15.

15 M. Rudin, *Molecular Imaging*, Imperial College Press, 2013.

16 A. Giussani and C. Hoeschen, *Imaging in Nuclear Medicine*, Springer Berlin Heidelberg, Berlin, Heidelberg, 2013.

17 K. L. Walker, M. S. Judenhofer, S. R. Cherry and G. S. Mitchell, Un-collimated single-photon imaging system for high-sensitivity small animal and plant imaging, *Phys. Med. Biol.*, 2015, **60**, 403–420.

18 A. H. Hielscher, A. Y. Bluestone, G. S. Abdoulaev, A. D. Klose, J. Lasker, M. Stewart, U. Netz and J. Beuthan, Near-infrared diffuse optical tomography, *Dis. Markers*, 2002, **18**, 313–337.

19 Y. Hoshi, Functional near-infrared optical imaging: Utility and limitations in human brain mapping, *Psychophysiology*, 2003, **40**, 511–520.

20 F. Stuker, J. Ripoll and M. Rudin, Fluorescence molecular tomography: Principles and potential for pharmaceutical research, *Pharmaceutics*, 2011, **3**, 229–274.

21 J. Culver, W. Akers and S. Achilefu, Multimodality Molecular Imaging with Combined Optical and SPECT/PET Modalities, *J. Nucl. Med.*, 2008, **49**, 169–172.

22 W. Han and G. Wang, Bioluminescence Tomography: Biomedical Background, Mathematical Theory, and Numerical Approximation., *J. Comput. Math.*, 2008, **26**, 324–335.

23 L. Mezzanotte, M. van ‘t Root, H. Karatas, E. A. Goun and C. W. G. M. Löwik, In Vivo Molecular Bioluminescence Imaging: New Tools and Applications, *Trends Biotechnol.*, 2017, **35**, 640–652.

24 A. J. Fisher, T. B. Thompson, J. B. Thoden, T. O. Baldwin and I. Rayment, The 1.5-Å resolution crystal structure of bacterial luciferase in low salt conditions, *J. Biol. Chem.*, 1996, **271**, 21956–21968.

25 S. N. Histed, M. L. Lindenberg, E. Mena, B. Turkbey, P. L. Choyke and K. a Kurdziel, Review of Functional / Anatomic Imaging in Oncology, *Nucl. Med. Commun.*, 2013, **33**, 349–361.

26 H. Zaidi and B. Hasegawa, Determination of the attenuation map in emission tomography., *J. Nucl. Med.*, 2003, **44**, 291–315.

27 Y. Chen and H. An, Attenuation Correction of PET/MR Imaging, *Magn. Reson. Imaging Clin. N. Am.*, 2017, **25**, 245–255.

28 E. J. R. van Beek and E. A. Hoffman, Functional Imaging: CT and MRI, *Clin. Chest Med.*, 2008, **29**, 195–216.

29 S. C. Mayo, F. Chen and R. Evans, Micron-scale 3D imaging of wood and plant microstructure using high-resolution X-ray phase-contrast microtomography, *J. Struct. Biol.*, 2010, **171**, 182–188.

30 P. Heimel, N. V. Swiadek, P. Slezak, M. Kerbl, C. Schneider, S. Nürnberger, H. Redl, A. H. Teuschl and D. Hercher, Iodine-Enhanced Micro-CT Imaging of Soft Tissue on the Example of Peripheral Nerve Regeneration, *Contrast Media Mol. Imaging*, , DOI:10.1155/2019/7483745.

31 P. Swart, M. Wicklein, D. Sykes, F. Ahmed and H. G. Krapp, A quantitative comparison of micro-CT preparations in Dipteran flies, *Sci. Rep.*, 2016, **6**, 1–12.

32 B. Crosson, A. Ford, K. M. McGregor, M. Meinzer, S. Cheshkov, L. Xiufeng, D. Walker-Batson and R. W. Briggs, Functional imaging and related techniques: An introduction for rehabilitation researchers, *J. Rehabil. Res. Dev.*, 2010, **47**, 7–33.

33 L. Martí-Bonmatí, R. Sopena, P. Bartumeus and P. Sopena, Multimodality imaging techniques, *Contrast Media Mol. Imaging*, 2010, **5**, 180–189.

34 F. Gazeau, in *Molecular Imaging Techniques: New Frontiers*, Future Science Ltd, Unitec House, 2 Albert Place, London N3 1QB, UK, 2013, pp. 2–5.

35 D. Brasse and F. Boisson, Instrumentation challenges in multi-modality imaging, *Nucl. Instruments Methods Phys. Res. Sect. A Accel. Spectrometers, Detect. Assoc. Equip.*,

2016, **809**, 67–75.

36 M. Moseley and G. Donnan, Multimodality imaging: Introduction, *Stroke*, 2004, **35**, 2632–2634.

37 M. Wu and J. Shu, Multimodal Molecular Imaging: Current Status and Future Directions, *Contrast Media Mol. Imaging*, 2018, **2018**, 1–12.

38 G. V Hirsch, C. M. Bauer and L. B. Merabet, Using structural and functional brain imaging to uncover how the brain adapts to blindness., *Ann. Neurosci. Psychol.*, 2015, **2**, 395–404.

39 H. Feng, X. Wang, J. Chen, J. Cui, T. Gao, Y. Gao and W. Zeng, Nuclear Imaging of Glucose Metabolism: Beyond 18 F-FDG, *Contrast Media Mol. Imaging*, 2019, **2019**, 1–12.

40 M. I. Menendez, B. Hettlich, L. Wei and M. V. Knopp, Preclinical multimodal molecular imaging using 18F-FDG PET/CT and MRI in a phase I study of a knee osteoarthritis in in vivo canine model, *Mol. Imaging*, 2017, **16**, 1–9.

41 S. Kanno, M. Yamawaki, H. Ishibashi, N. I. Kobayashi, A. Hirose, K. Tanoi, L. Nussaume and T. M. Nakanishi, Development of real-time radioisotope imaging systems for plant nutrient uptake studies, *Philos. Trans. R. Soc. B Biol. Sci.*, 2012, **367**, 1501–1508.

42 T. M. Nakanishi, Research with radiation and radioisotopes to better understand plant physiology and agricultural consequences of radioactive contamination from the Fukushima Daiichi nuclear accident, *J. Radioanal. Nucl. Chem.*, 2017, **311**, 947–971.

43 T. M. Nakanishi, What you can see by developing real-time radioisotope imaging system for plants: from water to element and CO2 gas imaging, *J. Radioanal. Nucl. Chem.*, 2018, **318**, 1689–1695.

44 E. A. Rennie and R. Turgeon, A comprehensive picture of phloem loading strategies, *Proc. Natl. Acad. Sci. U. S. A.*, 2009, **106**, 14162–14167.

45 M. Hubeau, J. Mincke, C. Vanhove, A. P. Gorel, A. Fayolle, J. Epila, O. Leroux, S.

Vandenberghe and K. Steppe, 11C-Autoradiographs to Image Phloem Loading, *Front. For. Glob. Chang.*, 2019, **2**, 1–11.

46 L. Li, Q. Zhang and D. Huang, A Review of Imaging Techniques for Plant Phenotyping, *Sensors*, 2014, **14**, 20078–20111.

47 R. Dong, Y. Li, W. Li, H. Zhang, Y. Liu, L. Ma, X. Wang and B. Lei, Recent developments in luminescent nanoparticles for plant imaging and photosynthesis, *J. Rare Earths*, 2019, 1–13.

48 D. Rousseau, Y. Chéné, E. Belin, G. Semaan, G. Trigui, K. Boudehri, F. Franconi and F. Chapeau-Blondeau, Multiscale imaging of plants: Current approaches and challenges, *Plant Methods*, 2015, **11**, 1–9.

49 J. Marion, R. Le Bars, L. Besse, H. Batoko and B. Satiat-Jeunemaitre, Multiscale and Multimodal Approaches to Study Autophagy in Model Plants, *Cells*, 2018, **7**, 5.

50 S. Dutta, J. A. Cruz, Y. Jiao, J. Chen, D. M. Kramer and K. W. Osteryoung, Non-invasive, whole-plant imaging of chloroplast movement and chlorophyll fluorescence reveals photosynthetic phenotypes independent of chloroplast photorelocation defects in chloroplast division mutants, *Plant J.*, 2015, **84**, 428–442.

51 A. Fatangare and A. Svatoš, Applications of 2-deoxy-2-fluoro-D-glucose (FDG) in Plant Imaging: Past, Present, and Future, *Front. Plant Sci.*, 2016, **7**, 1–11.

52 S. Jahnke, M. I. Menzel, D. Van Dusschoten, G. W. Roeb, J. Bühler, S. Minwuyelet, P. Blümler, V. M. Temperton, T. Hombach, M. Streun, S. Beer, M. Khodaverdi, K. Ziemons, H. H. Coenen and U. Schurr, Combined MRI-PET dissects dynamic changes in plant structures and functions, *Plant J.*, 2009, **59**, 634–644.

53 N. Kawachi, N. Suzui, S. Ishii, S. Ito, N. S. Ishioka, H. Yamazaki, A. Hatano-Iwasaki, K. Ogawa and S. Fujimaki, Real-time whole-plant imaging of 11C translocation using positron-emitting tracer imaging system, *Nucl. Instruments Methods Phys. Res. Sect. A Accel. Spectrometers, Detect. Assoc. Equip.*, 2011, **648**, S317–S320.

54 S. Kanno, H. Rai, T. Ohya, Y. Hayashi, K. Tanoi and T. M. Nakanishi, Real-time

imaging of radioisotope labeled compounds in a living plant, *J. Radioanal. Nucl. Chem.*, 2007, **272**, 565–570.

55 Q. Wang, A. J. Mathews, K. Li, J. Wen, S. Komarov, J. A. O'Sullivan and Y. C. Tai, A dedicated high-resolution PET imager for plant sciences, *Phys. Med. Biol.*, 2014, **59**, 5613–5629.

56 N. Kawachi, Y. G. Yin, N. Suzui, S. Ishii, T. Yoshihara, H. Watabe, S. Yamamoto and S. Fujimaki, Imaging of radiocesium uptake dynamics in a plant body by using a newly developed high-resolution gamma camera, *J. Environ. Radioact.*, 2016, **151**, 461–467.

57 A. Fatangare, P. Gebhardt, H. Saluz and A. Svatoš, Comparing 2-[18F]fluoro-2-deoxy-D-glucose and [68Ga]gallium-citrate translocation in Arabidopsis thaliana, *Nucl. Med. Biol.*, 2014, **41**, 737–743.

58 R. Metzner, A. Eggert, D. van Dusschoten, D. Pflugfelder, S. Gerth, U. Schurr, N. Uhlmann and S. Jahnke, Direct comparison of MRI and X-ray CT technologies for 3D imaging of root systems in soil: Potential and challenges for root trait quantification, *Plant Methods*, 2015, **11**, 1–11.

59 D. Pflugfelder, R. Metzner, D. Dusschoten, R. Reichel, S. Jahnke and R. Koller, Non-invasive imaging of plant roots in different soils using magnetic resonance imaging (MRI), *Plant Methods*, 2017, **13**, 1–9.

60 H. van As, T. Scheenen and F. J. Vergeldt, MRI of intact plants, *Photosynth. Res.*, 2009, **102**, 213–222.

61 W. H. Stuppy, J. A. Maisano, M. W. Colbert, P. J. Rudall and T. B. Rowe, Three-dimensional analysis of plant structure using high-resolution X-ray computed tomography, *Trends Plant Sci.*, 2003, **8**, 2–6.

62 S. Dhondt, H. Vanhaeren, D. Van Loo, V. Cnudde and D. Inzé, Plant structure visualization by high-resolution X-ray computed tomography, *Trends Plant Sci.*, 2010, **15**, 419–422.

63 H. Help, M. Lusa, A.-P. Honkanen, A. Diaz, M. Holler, M. Salomé, P. Cloetens, H.

Mäkinen, S. Huotari and H. Suhonen, High-resolution synchrotron imaging studies of intact fresh roots reveal soil bacteria promoted bioremediation and bio-fortification, 2019, 1–43.

64 M. Lusa, H. Help, A.-P. Honkanen, J. Knuutinen, J. Parkkonen, D. Kalasová and M. Bomberg, The reduction of selenium(IV) by boreal Pseudomonas sp. strain T5-6-I – Effects on selenium(IV) uptake in Brassica oleracea, *Environ. Res.*, 2019, **177**, 108642.

65 R. Sugita, N. I. Kobayashi, A. Hirose, K. Tanoi and T. M. Nakanishi, Evaluation of in vivo detection properties of 22Na, 65Zn, 86Rb, 109Cd and 137Cs in plant tissues using real-time radioisotope imaging system, *Phys. Med. Biol.*, 2014, **59**, 837–851.

66 D. L. Alexoff, S. L. Dewey, P. Vaska, S. Krishnamoorthy, R. Ferrieri, M. Schueller, D. J. Schlyer and J. S. Fowler, PET imaging of thin objects: Measuring the effects of positron range and partial-volume averaging in the leaf of Nicotiana tabacum, *Nucl. Med. Biol.*, 2011, **38**, 191–200.

67 M. R. Kiser, C. D. Reid, A. S. Crowell, R. P. Phillips and C. R. Howell, Exploring the transport of plant metabolites using positron emitting radiotracers, *HFSP J.*, 2008, **2**, 189–204.

68 A. Fatangare, C. Paetz, H. Saluz and A. Svatoš, 2-Deoxy-2-fluoro-D-glucose metabolism in Arabidopsis thaliana, *Front. Plant Sci.*, 2015, **6**, 1–12.

69 T. K. Nayak and M. W. Brechbiel, Radioimmunoimaging with Longer-Lived Positron-Emitting Radionuclides: Potentials and Challenges, *Bioconjug. Chem.*, 2009, **20**, 825–841.

70 J. R. Rumble, Ed., *CRC Handbook of Chemistry and Physics (Internet Version 2019)*, CRC Press/Taylor & Francis, Boca Raton, FL, 100th edn., 2019.

71 N. N. Greenwood and A. Earnshaw, *Chemistry of the Elements*, Elsevier, 1997.

72 J. E. House, *Inorganic Chemistry*, Elsevier, 2013.

73 H. H. Coenen, J. Mertens and B. Maziére, *Radioiodination Reactions for Pharmaceuticals*, Springer Netherlands, Dordrecht, 2006.

74 H. Lusic and M. W. Grinstaff, X-ray-computed tomography contrast agents, *Chem. Rev.*, 2013, **113**, 1641–1666.

75 P. M. Gignac, N. J. Kley, J. A. Clarke, M. W. Colbert, A. C. Morhardt, D. Cerio, I. N. Cost, P. G. Cox, J. D. Daza, C. M. Early, M. S. Echols, R. M. Henkelman, A. N. Herdina, C. M. Holliday, Z. Li, K. Mahlow, S. Merchant, J. Müller, C. P. Orsbon, D. J. Paluh, M. L. Thies, H. P. Tsai and L. M. Witmer, Diffusible iodine-based contrast-enhanced computed tomography (diceCT): An emerging tool for rapid, high-resolution, 3-D imaging of metazoan soft tissues, *J. Anat.*, 2016, **228**, 889–909.

76 J. R. Ashton, J. L. West and C. T. Badea, In vivo small animal micro-CT using nanoparticle contrast agents, *Front. Pharmacol.*, 2015, **6**, 1–22.

77 D. L. Smith, W. A. P. Breeman and J. Sims-Mourtada, The untapped potential of Gallium 68-PET: The next wave of 68Ga-agents, *Appl. Radiat. Isot.*, 2013, **76**, 14–23.

78 N. A. Lassen, A reappraisal of the relative merits of SPET and PET in the quantitation of neuroreceptors: The advantage of a longer half-life!, *Eur. J. Nucl. Med.*, 1996, **23**, 1–4.

79 J. L. H. Eersels, M. J. Travis and J. D. M. Herscheid, Manufacturing I-123-labelled radiopharmaceuticals. Pitfalls and solutions, *J. Label. Compd. Radiopharm.*, 2005, **48**, 241–257.

80 R. Kuker, M. Sztejnberg and S. Gulec, I-124 Imaging and Dosimetry, *Mol. Imaging Radionucl. Ther.*, 2017, **26**, 66–73.

81 M. Lubberink and H. Herzog, Quantitative imaging of 124I and 86Y with PET, *Eur. J. Nucl. Med. Mol. Imaging*, 2011, **38**, 10–18.

82 R. H. Seevers and R. E. Counsell, Radioiodination Techniques for Small Organic Molecules, *Chem. Rev.*, 1982, **82**, 575–590.

83 C. Binder, R. J. Crilly, S. Brown, A. Skalet and A. Y. Hung, Plaque Size and Dose in I-125 Eye Plaque Brachytherapy, *Int. J. Radiat. Oncol.*, 2016, **96**, E596.

84 D. M. Routman, R. K. Funk, B. J. Stish, L. A. Mynderse, T. M. Wilson, R. McLaren, W.

S. Harmsen, K. Mara, C. L. Deufel, K. M. Furutani, M. G. Haddock, T. M. Pisansky, C. R. Choo and B. J. Davis, Permanent prostate brachytherapy monotherapy with I-125 for low- and intermediate-risk prostate cancer: Outcomes in 974 patients, *Brachytherapy*, 2019, **18**, 1–7.

85 J. J. M. De Goeij and M. L. Bonardi, How do we define the concepts specific activity, radioactive concentration, carrier, carrier-free and no-carrier-added?, *J. Radioanal. Nucl. Chem.*, 2005, **263**, 13–18.

86 J. Clayden, N. Greeves and S. G. Warren, *Organic Chemistry*, Oxford University Press, Oxford, 2nd edn., 2012.

87 N. A. Senger, B. Bo, Q. Cheng, J. R. Keeffe, S. Gronert and W. Wu, The Element Effect Revisited: Factors Determining Leaving Group Ability in Activated Nucleophilic Aromatic Substitution Reactions, *J. Org. Chem.*, 2012, **77**, 9535–9540.

88 D. D. McClosky, B. Wang, G. Chen and C. T. Anderson, The click-compatible sugar 6-deoxy-alkynyl glucose metabolically incorporates into Arabidopsis root hair tips and arrests their growth, *Phytochemistry*, 2016, **123**, 16–24.

89 B. Wang, D. D. McClosky, C. T. Anderson and G. Chen, Synthesis of a suite of click-compatible sugar analogs for probing carbohydrate metabolism, *Carbohydr. Res.*, 2016, **433**, 54–62.

90 P. A. Turhanen and J. J. Vepsäläinen, A powerful tool for acid catalyzed organic addition and substitution reactions, *RSC Adv.*, 2015, **5**, 26218–26222.

91 J. M. Timonen and P. A. Turhanen, (E)-Di-iodination of Alkynes Using Dried Dowex H + /NaI Approach , *ACS Omega*, 2019, **4**, 14663–14668.

92 Eppendorf AG, Eppendorf Tubes, Instructions for use, https://www.eppendorf.com/product-media/doc/en/234161/Consumables_Instructions-use_Tubes-Tubes-50-mL.pdf, (accessed 14 October 2019).

93 T. Keller, F. R. López-Picón, A. Krzyczmonik, S. Forsback, J. S. Takkinen, J. Rajander, S. Teperi, F. Dollé, J. O. Rinne, M. Haaparanta-Solin and O. Solin, Comparison of high

and low molar activity TSPO tracer [18F]F-DPA in a mouse model of Alzheimer's disease, *J. Cereb. Blood Flow Metab.*, , DOI:10.1177/0271678X19853117.

94 S. Mushtaq, J. Jeon, A. Shaheen, B. S. Jang and S. H. Park, Critical analysis of radioiodination techniques for micro and macro organic molecules, *J. Radioanal. Nucl. Chem.*, 2016, **309**, 859–889.

95 P. L. Chen, A. Hussain and H. H. Tai, An Improved Method of Radioiodination with Chloramine T, *Anal. Biochem.*, 1994, **219**, 159–161.

96 A. A. Hussain, J. A. Jona, A. Yamada and L. W. Dittert, Chloramine-T in radiolabeling techniques. II. A nondestructive method for radiolabeling biomolecules by halogenation, *Anal. Biochem.*, 1995, **224**, 221–226.

97 X. Liu, G. Chen, C. Li and P. Liu, Chloramine Salt Mediated Oxidative Halogenation of Terminal Alkynes with KI or NaBr: Practical Synthesis of 1-Bromoalkynes and 1-Iodoalkynes, *Synlett*, 2018, **29**, 2051–2055.

98 G. B. Saha, J. Whitten and R. T. Go, Conditions of radioiodination with iodogen as oxidizing agent, *Int. J. Radiat. Appl. Instrumentation.*, 1989, **16**, 431–433.

99 T. Ünak, Z. Akgün, Y. Yildirim, Y. Duman and G. Erenel, Self-radioiodination of iodogen, *Appl. Radiat. Isot.*, 2001, **54**, 749–752.

100 R. Chinchilla and C. Nájera, Chemicals from Alkynes with Palladium Catalysts, *Chem. Rev.*, 2014, **114**, 1783–1826.

101 W. Shi, Z. Guan, P. Cai and H. Chen, Highly efficient and recyclable catalyst for the direct chlorination, bromination and iodination of terminal alkynes, *J. Catal.*, 2017, **353**, 199–204.

102 Y. Liu, D. Huang, J. Huang and K. Maruoka, Hypervalent Iodine Mediated Chemoselective Iodination of Alkynes, *J. Org. Chem.*, 2017, **82**, 11865–11871.

Attachment 1. Radio-HPLC results of method optimization and comparison to electrophilic substitution

Radio-HPLC results of method optimization and comparison to electrophilic substitution are presented in this attachment, combined to the sample batch parameters.

Table 10. Radio-HPLC results of method optimization and comparison to electrophilic substitution. RCY (total and for individual products) is presented as a sample batch average. Standard deviation and error are calculated for total RCY, and are presented as absolute, not relative.

Batch code	Reaction t (min)	Reaction T (°C)	Amount of carrier (µmol)	Solvent	Dowex activation	Excess water evaporated	Facilitating agent	Average radiochemical yield				n	Standard deviation	Standard error
								Product 1	Product 2	Product 3	Total			
IRa190122	75	70	1.2	cyclohexanol	N	N	Dowex	2.3 %	19.1 %	6.9 %	28.3 %	2	3.6 %	2.6 %
IRa190122	75	70	1.2	DMSO	N	N	Dowex	0.0 %	1.7 %	11.7 %	12.9 %	3	4.3 %	2.5 %
IRa190124	75	70	1.2	2-propanol	N	N	Dowex	15.0 %	0.0 %	42.6 %	50.1 %	2	0.5 %	0.3 %
IRa190124	75	70	1.2	DMF	N	N	Dowex	0.0 %	0.0 %	0.0 %	0.0 %	0	0.0 %	0.0 %
IRa190220	60	70	1.2	cyclohexanol	Y	N	Dowex	4.5 %	11.2 %	9.2 %	23.4 %	3	4.7 %	2.7 %
IRa190220	60	70	1.2	DMSO	Y	N	Dowex	0.0 %	0.0 %	6.4 %	6.4 %	3	3.3 %	1.9 %
IRa190221	60	70	1.2	2-propanol	Y	N	Dowex	8.4 %	8.8 %	48.8 %	57.3 %	3	14.2 %	8.2 %
IRa190221	60	70	1.2	DMF	Y	N	Dowex	0.0 %	0.0 %	4.5 %	4.5 %	3	0.3 %	0.2 %
IRa190304	60	70	3.0	cyclohexanol	Y	N	Dowex	5.6 %	7.3 %	30.8 %	39.4 %	3	8.6 %	5.0 %
IRa190304	60	70	3.0	DMSO	Y	N	Dowex	0.0 %	0.0 %	11.0 %	11.0 %	3	1.1 %	0.6 %
IRa190305	60	70	3.0	2-propanol	Y	N	Dowex	7.0 %	0.0 %	54.7 %	61.6 %	3	6.8 %	3.9 %
IRa190305	60	70	3.0	DMF	Y	N	Dowex	0.0 %	0.0 %	4.5 %	4.5 %	3	1.0 %	0.6 %
IRa190313	60	70	5.0	cyclohexanol	Y	N	Dowex	3.2 %	10.3 %	14.8 %	27.2 %	3	2.8 %	1.6 %
IRa190313	60	70	5.0	DMSO	Y	N	Dowex	0.0 %	0.0 %	7.7 %	7.7 %	3	1.0 %	0.5 %
IRa190314	60	70	5.0	2-propanol	Y	N	Dowex	5.0 %	0.0 %	64.3 %	69.3 %	3	9.9 %	5.7 %
IRa190314	60	70	5.0	DMF	Y	N	Dowex	0.0 %	0.0 %	5.3 %	5.3 %	2	1.1 %	0.8 %
IRa190322	60	95	3.0	cyclohexanol	Y	N	Dowex	7.6 %	11.4 %	24.2 %	40.6 %	3	19.3 %	11.2 %
IRa190322	60	95	3.0	DMSO	Y	N	Dowex	0.0 %	5.2 %	26.6 %	29.2 %	2	9.5 %	6.7 %
IRa190322	60	95	3.0	2-propanol	Y	N	Dowex	8.6 %	7.1 %	52.0 %	57.3 %	3	10.1 %	5.8 %
IRa190322	60	95	3.0	DMF	Y	N	Dowex	0.0 %	0.0 %	10.1 %	10.1 %	3	4.3 %	2.5 %
IRa190329	60	120	3.0	cyclohexanol	Y	N	Dowex	0.0 %	0.0 %	74.4 %	74.4 %	3	7.4 %	4.3 %
IRa190329	60	120	3.0	DMSO	Y	N	Dowex	0.0 %	7.4 %	38.5 %	45.9 %	3	2.3 %	1.3 %
IRa190329	60	120	3.0	2-propanol	Y	N	Dowex	0.0 %	0.0 %	0.0 %	0.0 %	0	0.0 %	0.0 %
IRa190329	60	120	3.0	DMF	Y	N	Dowex	0.0 %	0.0 %	14.0 %	14.0 %	3	0.5 %	0.3 %
IRa190510	60	95	3.0	cyclohexanol	Y	Y	Dowex	0.0 %	0.0 %	75.5 %	75.5 %	3	7.8 %	4.5 %
IRa190510	60	95	3.0	cyclohexanol	Y	N	Dowex	0.0 %	0.0 %	49.7 %	64.6 %	2	8.9 %	6.3 %
IRa190527	60	95	3.0	cyclohexanol	Y	Y	Dowex	6.1 %	15.6 %	55.2 %	76.8 %	3	2.8 %	1.6 %
IRa190527	60	95	3.0	cyclohexanol	Y	Y	Chloramine T	5.8 %	3.1 %	5.2 %	14.1 %	3	1.7 %	1.0 %
IRa190527	60	95	3.0	cyclohexanol	Y	Y	Iodogen	5.5 %	5.5 %	10.8 %	20.0 %	3	4.7 %	2.7 %

Attachment 2. Radio HPLC results of sugar analogue radioiodination

Radio-HPLC results of sugar analogue radioiodination are presented in this attachment, combined to the sample batch parameters.

Table 11. Radio-HPLC results of sugar analogue radioiodination. Standard deviation and error are calculated are presented as absolute, not relative.

Batch code	Precursor	Reaction t (min)	Reaction T (°C)	Amount of carrier (µmol)	Solvent	Dowex activation	Excess water evaporated	Facilitating agent	Main product retention time (min)	Average main product RCY	n	Standard deviation	Standard error
IRa190605	Precursor 1	60	95	3	cyclohexanol	Y	Y	Dowex	10.30	49.88 %	3	4.8 %	2.8 %
IRa190605	Precursor 2	60	95	3	cyclohexanol	Y	Y	Dowex	9.89	55.95 %	3	8.9 %	5.1 %

Attachment 3. Results of statistical tests

Results of statistical tests for this study are presented in this attachment. Degrees of freedom are calculated as n-1, where n = total sample size. Tests for statistical significance were tested with a two-tailed T-test assuming equal variances for two sample sets, and with a single-factor ANOVA for three sample sets.

Table 12. Results of statistical tests.

Test parameter	Solvent	Statistical test	Degrees of freedom	P-value
Resin activation	cyclohexanol	T-test	4	0.307038
Resin activation	DMSO	T-test	5	0.109828
Resin activation	2-propanol	T-test	4	0.544846
Amount of carrier	cyclohexanol	ANOVA	8	0.035989
Amount of carrier	DMSO	ANOVA	8	0.086890
Amount of carrier	2-propanol	ANOVA	8	0.438246
Amount of carrier	DMF	ANOVA	7	0.510594
Reaction temperature	cyclohexanol	ANOVA	8	0.026279
Reaction temperature	DMSO	ANOVA	7	0.000649
Reaction temperature	2-propanol	T-test	5	0.569685
Reaction temperature	DMF	ANOVA	8	0.010967
Excess water removal	cyclohexanol	T-test	5	0.181704
Comparison to electrophilic reactions	cyclohexanol	ANOVA	8	0.000001
Radioiodination of sugar analogues	cyclohexanol	T-test	5	0.356533

Attachment 4. NMR spectrum of **4** (1-(prop-2-yn-1-yloxy)-2,3,4,6-tetra-O-acetyl-D-glucose)

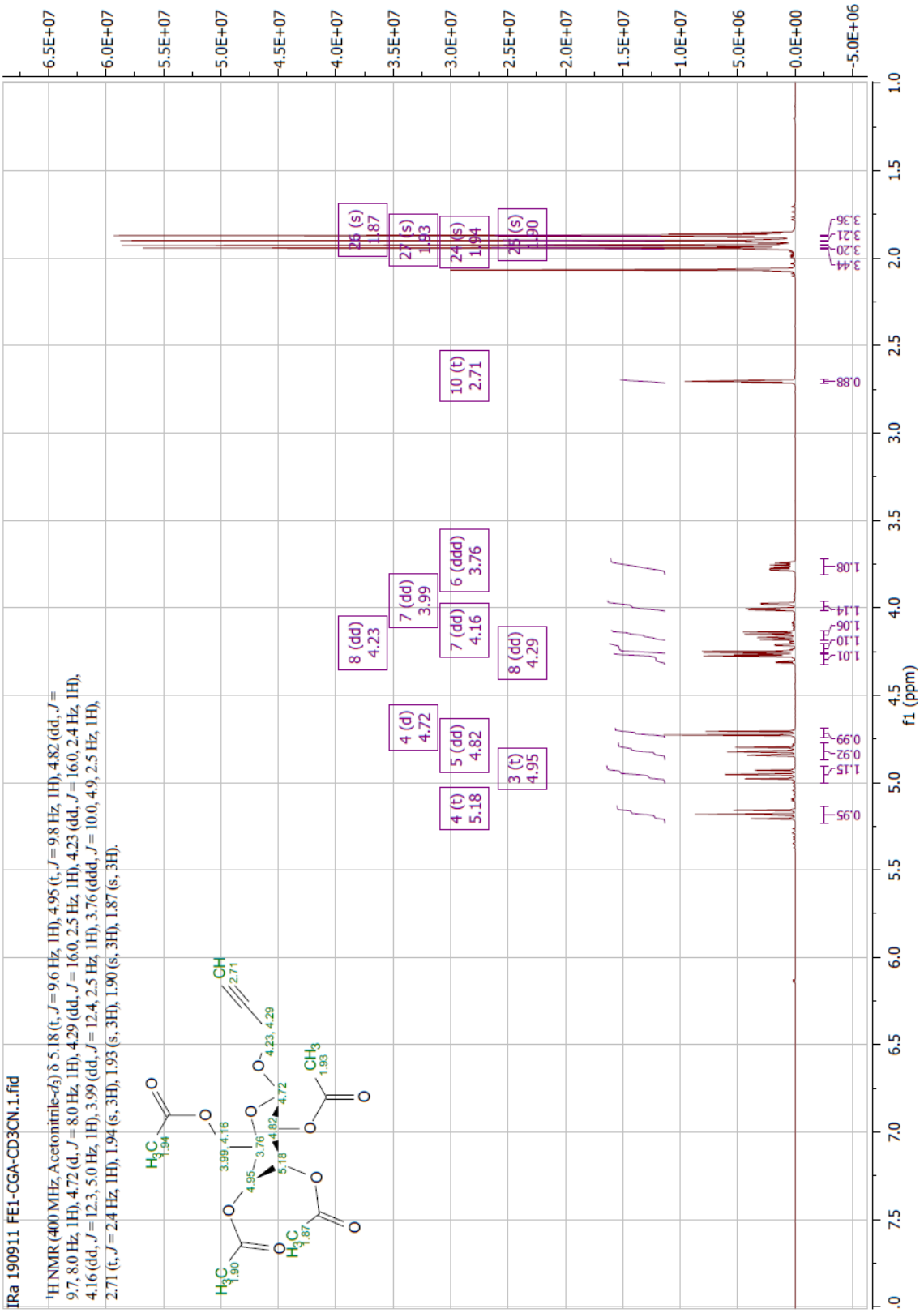

Attachment 5. NMR spectrum of **5** (1,3-di-(prop-2-yn-1-yloxy)-2,4,6-tri-O-acetyl-D-glucose)

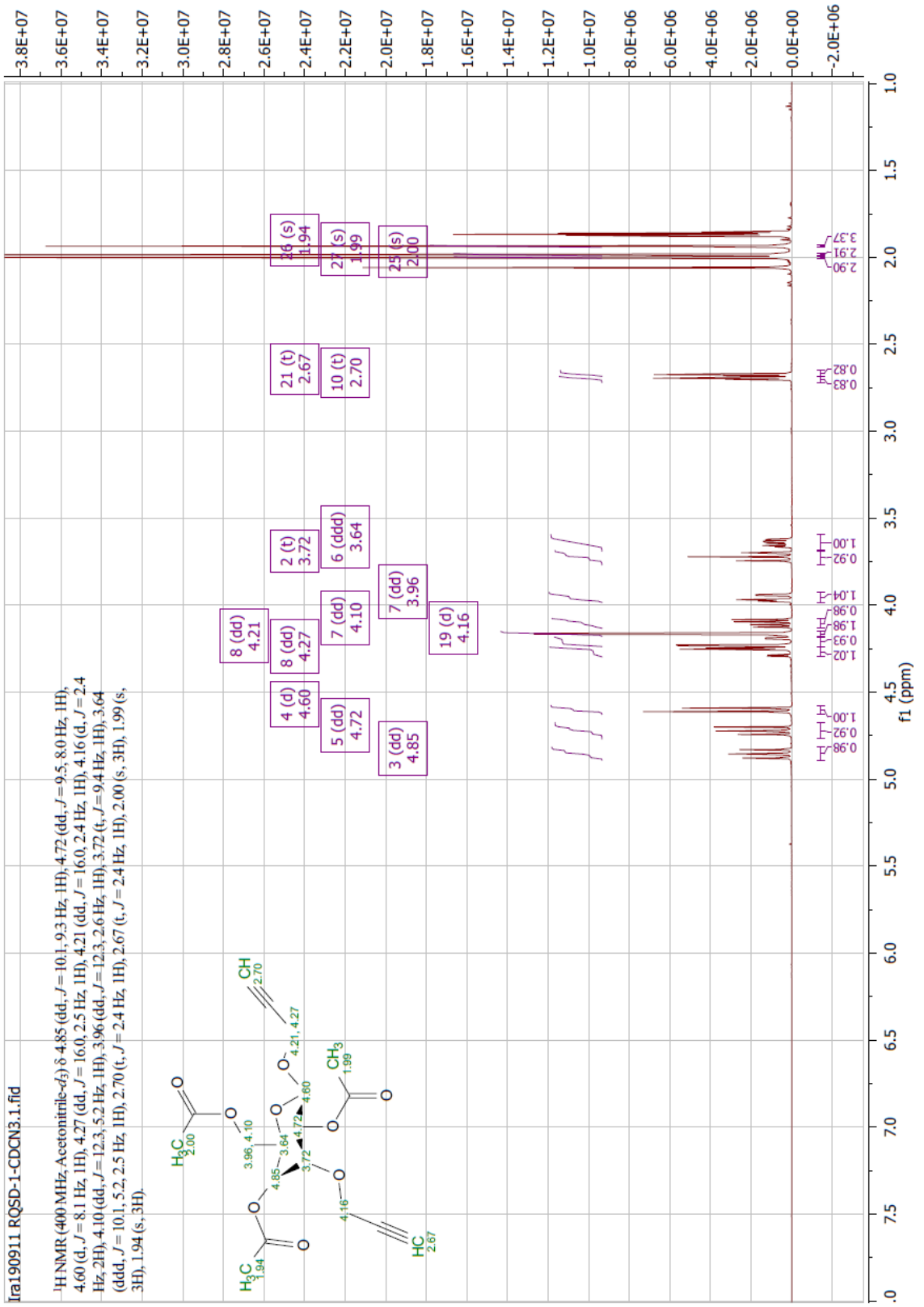

Attachment 6. NMR spectrum of **6** (1-((E)-2,3-diiodo-prop-2-en-1-yloxy)-2,3,4,6-tetra-O-acetyl-D-glucose)

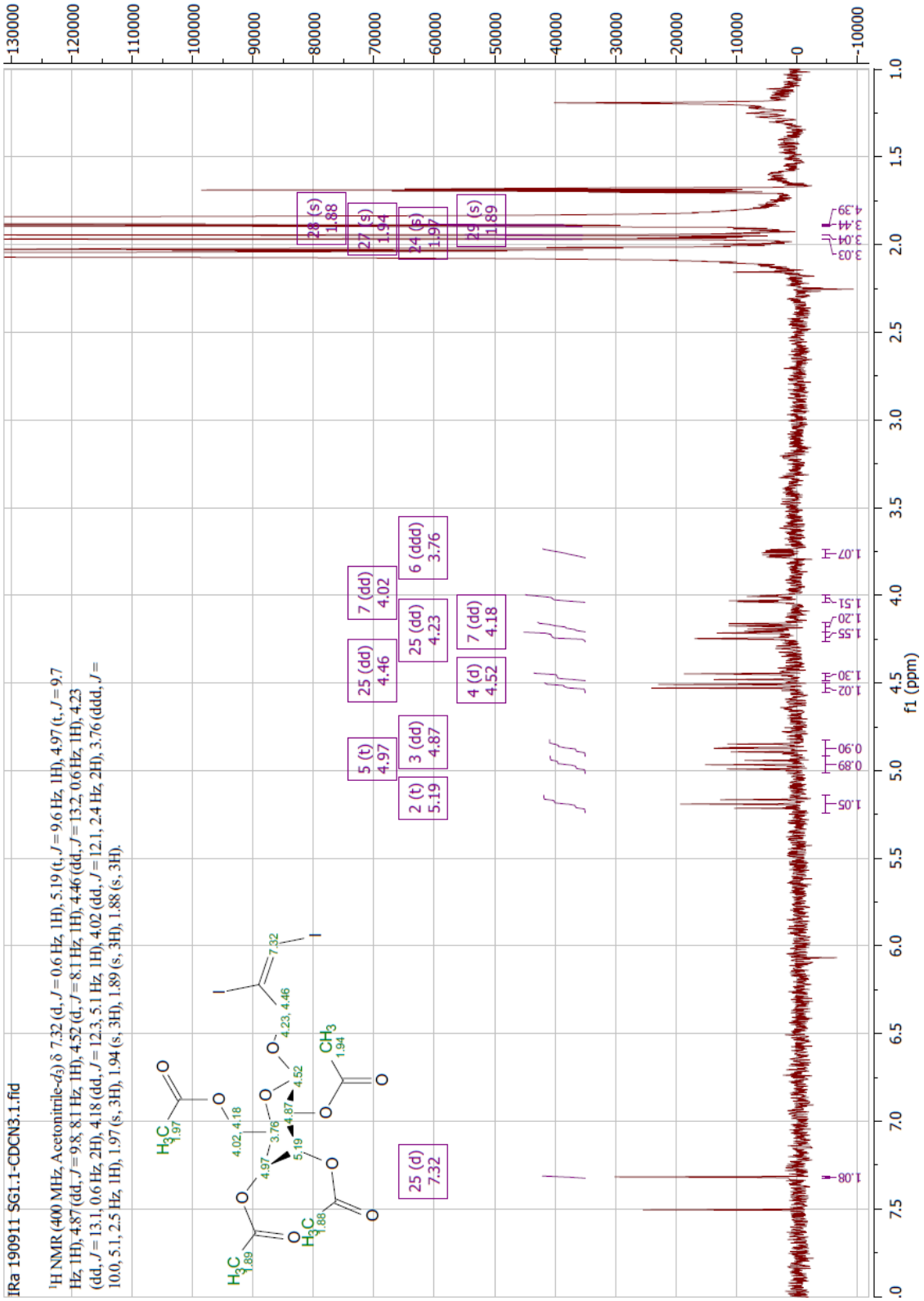

Attachment 7. NMR spectrum of **7** (1-((E)-2,3-diiodo-prop-2-en-1-yloxy)-3-(prop-2-yn-1-yloxy)-2,4,6-tri-O-acetyl-D-glucose)